

SPATIAL DISTRIBUTIONS AND TRANSIENT EFFECTS  
IN MOLECULAR FLUXES FOR THE  
CALIBRATION OF THERMAL DESORPTION SPECTROMETERS

By

Robert H. Jackson

B. S. University of Maine, 1991

M. S. University of Maine, 1996

A THESIS

Submitted in Partial Fulfillment of the

Requirements for the Degree of

Doctor of Philosophy

(in Physics)

The Graduate School

University of Maine

August, 2000

Advisory Committee:

Brian G. Frederick, Professor of Chemistry, Advisor

William N. Unertl, Professor of Physics

Robert J. Lad, Professor of Physics

François G. Amar, Professor of Chemistry

Touradj Solouki, Professor of Chemistry

John B. Hudson, Professor of Materials Science and Engineering,  
Rensselaer Polytechnic Institute (External Reader)

# Table of Contents

<b>LIST OF TABLES.....</b>	<b>VIII</b>
<b>1 INTRODUCTION.....</b>	<b>1</b>
1.1 OVERVIEW OF THE DIFFERENTIALLY PUMPED MASS SPECTROMETER .....	4
1.1.1 Design criteria for a high performance calibrated thermal desorption spectrometer (CTDS) .....	4
1.1.2 The CTDS instrument.....	5
1.1.3 Previous test results of the CTDS system regarding the O/Pd(110) system .....	6
1.2 SUMMARY OF THE THIS WORK.....	7
<b>2 THE DESIGN OF A CALIBRATED THERMAL DESORPTION SPECTROMETER.....</b>	<b>9</b>
2.1 THEORY AND BASIS OF THE TECHNIQUE.....	9
2.1.1 The Wigner-Polanyi equation for desorption .....	10
2.1.2 The effects of the shroud on the mass spectrometer .....	14
2.1.3 The effusion source as a calibrated flow source .....	17
2.1.4 The spinning rotor gauge .....	21
2.2 DESIGN OF THE INSTRUMENT .....	26
2.2.1 The cone geometry and mass spectrometer modifications .....	27
2.2.2 The effusion source.....	41
2.3 CALIBRATION AND TESTING.....	41
2.3.1 The gas chamber volume calibration .....	42
2.3.2 The gas flow calibration .....	47
2.3.3 The mass spectrometer flow gain .....	50
2.3.4 A test study of Pd(110) with O <sub>2</sub> .....	53
<b>3 AN EXTENDED FORMALISM FOR THE GLASS CAPILLARY ARRAY FLUXES .....</b>	<b>56</b>
3.1 BACKGROUND.....	57
3.2 THE REPARAMETERIZATION .....	60
3.3 ARBITRARILY SHAPED PLANAR TARGETS AT ANY POSITION .....	63
3.4 THE EXPERIMENTAL SETUP FOR THE MEASUREMENT OF THE SPATIAL FLUX DISTRIBUTION.....	65
3.4.1 The differentially pumped mass spectrometer specifications .....	65
3.4.2 The Doser .....	65
3.5 MEASUREMENT AND ANALYSIS OF THE DOSER FLUX .....	67
3.6 CONCLUSIONS .....	78
<b>4 TRANSIENT MOLECULAR FLOW IN DOSERS.....</b>	<b>79</b>
4.1 BACKGROUND.....	79
4.2 SIMPLE NON-STICKING TRANSIENT FLOW MODEL.....	81
4.3 FITTING THE TRANSIENT FLOW OF ARGON GAS .....	88
4.4 TRANSIENT FLOW MODEL WITH A CONSTANT STICKING COEFFICIENT .....	91
4.5 TRANSIENT FLOW WITH A RESTRICTED EXIT .....	100
4.6 CONCLUSIONS, LIMITATIONS, AND FURTHER WORK .....	106
<b>5 CALIBRATED ABSORPTION AND DESORPTION.....</b>	<b>108</b>
5.1 A LITERATURE REVIEW OF O/Pd(110) .....	110
5.2 THE EXPERIMENTAL SETUP .....	111
5.2.1 Changes to the system since the MS Thesis .....	112
5.2.2 Preparation of the Pd(110) sample.....	114

5.3 THE BASIC CALIBRATION PROCEDURE .....	114
5.3.1 Gas source calibration.....	115
5.3.2 Mass spectrometer calibration .....	118
5.4 RESULTS .....	120
5.4.1 Calibrated thermal desorption spectrometry (CTDS) on O on Pd(110).....	121
5.4.2 Comparison of uptake measurements with the TDS.....	125
5.4.3 Error analysis.....	139
5.4.4 Transient effects: doser losses or mass spectrometer gain change.....	141
<b>6 CONCLUSIONS AND FURTHER WORK .....</b>	<b>157</b>
6.1 SUMMARY OF THIS WORK.....	157
6.2 RECOMMENDATIONS FOR FURTHER WORK .....	160
<b>REFERENCES .....</b>	<b>165</b>
<b>BIOGRAPHY OF THE AUTHOR .....</b>	<b>171</b>

## List of Figures

2.1 Schematic of a calibrated effusion source.....	18
2.2 The spinning rotor gauge from the Leybold-Infocon VM211 manual.....	21
2.3 Velocity vectors for impingement on the ball.....	22
2.4 Histogram of $\sigma$ for 68 smooth stainless steel ball bearings. ....	24
2.5 Changes from the initial values of $\sigma$ of five NIST rotors.....	25
2.6 Typical measurement uncertainty, $E_{total}$ % versus pressure in the spinning rotor gauge.....	25
2.7 The basic configuration of the CTDS with the important dimensions.....	28
2.8 Pressure and flow criteria in the S- $\Phi$ plane.....	31
2.9 Peak first order desorption flow as a function of initial coverage .....	33
2.10 Molecular transmission probability of an annular cylindrical pipe.....	35
2.11 The contour plots of conductance from and pumping speed at the ionizer for values of $r$ and $l_c$ .....	36
2.12 Contour plot of the characteristic pumping time over the $l_i$ - $r$ plane and a contour plot of the percent pumping speed immunity over the $l_c$ - $r$ plane.....	37
2.13 C, $\% \epsilon$ , and $\tau$ for the chosen design versus the cone position.....	38
2.14 C, $\% \epsilon$ , and $\tau$ for the chosen design versus the molecular weight of the gas used.....	40
2.15 Reference volume calibration assembly.....	43
2.16 Effusion source flow calibration for argon gas.....	48
2.17 Effusion calibration for CO gas compared to the adjusted argon calibration.....	49
2.18 Mass-spectrometer flow calibration for Ar, CO, O <sub>2</sub> , and N <sub>2</sub> gas.....	52
2.19 The effective area for molecules desorbing into the aperture.....	53
2.20 CTPD of oxygen on Pd(110) with coverages calculated integrating the desorption rate.....	54
3.1 The coordinates for the doser and target integrations.....	59
3.2 The reparameterized coordinates on the doser for each target position $r_t$ .....	60

3.3 The doser tube terminated in a 1.35 cm diameter glass capillary array .....	66
3.4 A microscope image of the glass capillary array showing its hexagonal close packed hexagonal tubes.....	67
3.5 The fraction of the total doser flow intercepted by the aperture. ....	69
3.6 The background mass spectrometer signal versus distance to the doser axis .....	70
3.7 The measure fraction of the doser flux to the aperture at a distance of 0.0635cm.....	73
3.8 The measured fraction of doser flux through the 0.0635cm aperture at a distance of 1.00cm.....	75
3.9 A comparison of the average flux density at the aperture (solid curves) with their corresponding calculated flux densities.....	77
4.1 The coordinates and boundary conditions for the long narrow tube.....	81
4.2 The base function $\lambda(\xi, \tau)$ for the number density transient in a long narrow tube.....	84
4.3 The base function $\gamma(\xi, \tau)$ for the transient flow in a long narrow tube.....	85
4.4 Measured argon transient through the doser normalized to the fit value for steady state height. ....	89
4.5 Measured argon transient through the tube directly into the mass spectrometer shroud, normalized to the fit value for steady state height.....	90
4.6 The steady state exit fraction versus $x = \lambda L = \frac{L}{d} \sqrt{3S_0}$ for a long narrow tube with constant sticking coefficient $S_0$ .....	94
4.7 The fraction of gas exiting a 1 m long tube of 1 cm diameter for several sticking probabilities .....	96
4.8 The fraction exiting normalized to the steady state value for a 1m long 1cm diameter tube with constant sticking probabilities.....	97
4.9 a) The time to reach 10% of the steady state value. (b) The time to reach 90% of the steady state value for a step change in the at the inlet of a 1 m long 1 cm diameter tube versus a constant sticking probability.....	99
4.10 A uniform equal step path along the tube. ....	100

4.11 The fraction of gas exiting the 1m long 1cm diameter tube with a restricted outlet.....	104
4.12 The time to reach 10% of the steady state value. (b) The time reach 90% of the steady state value for a step change in the at the inlet of a 1 m long 1 cm diameter tube versus the ratio of restriction conductance $C_0$ to tube conductance $C_{tube}$ .....	105
5.1 The mass spectrometer shroud with the small solid metal cone obstructing the line-of-sight path from the aperture to the axial ionizer.....	113
5.2 The argon number density in the gas source as the gas effuses through the positive shutoff capillary valve. The plus signs mark every forth data point. ....	117
5.3 Typical pulse for calibrating the differentially pump mass spectrometer for flow. (a) Measure current; (b) current corrected for the exponential drop in gas source flow with $\alpha_{dose} = 4.594 \times 10^{-4} \cdot s^{-1}$ .....	119
5.4 CTDS of oxygen on Pd(110) at 310K.....	122
5.5 Coverage of atomic oxygen on Pd(110) measured by CTDS versus the total gas released in each dose at 310K.....	124
5.6 Schematic representation of the double dose mass spectrometer signals in our modified King-Wells experiment.....	126
5.7 Flow of oxygen gas into the chamber during a double dose of the Pd(110) crystal at 310K with a calibration factor, $\lambda = 2.59 \times 10^{22} s^{-1} A^{-1}$ .....	129
5.8 Flow of oxygen gas into the chamber during a double dose of the Pd(110) crystal at 400K with a calibration factor, $\lambda = 2.70 \times 10^{22} s^{-1} A^{-1}$ .....	130
5.9 Flow of oxygen gas into the chamber during a double dose of the Pd(110) crystal at 475K with a calibration factor $\lambda = 2.76 \times 10^{22} s^{-1} A^{-1}$ .....	131
5.10 CTDS of oxygen on Pd(110) for each of the dose pairs at temperature and coverage: (a) 310K, 0.500, (b) 475K, 0.442, and (c) 400K, 0.409. ....	132
5.11 Oxygen uptake rate on a $0.8877\text{cm}^2$ surface area of the Pd(110) crystal at a doser flow of $1.7 \times 10^{13}$ molecule $s^{-1}$ at 310K.....	134
5.12 Oxygen uptake rate on a $0.8877\text{cm}^2$ surface area of the Pd(110) crystal at a doser flow of $1.7 \times 10^{13}$ molecule $s^{-1}$ at 400K.....	135

5.13 Oxygen uptake rate on a $0.8877\text{cm}^2$ surface area of the Pd(110) crystal at a doser flow of $1.7 \times 10^{13}$ molecule $\text{s}^{-1}$ at 475K.....	136
5.14 The coverage versus dose for each double dose pair at temperature (a) 310K, (b) 475K, and (c) 400K.....	137
5.15 60s oxygen pulses for the doser into the mass spectrometer in term of the instantaneous reciprocal of the flow gain.....	144
5.16 The top portion of 5.15.....	145
5.17 The linear relationship between the peak method and integral method calibration factors.....	147
5.18 The inverse flow gain of Figure 5.15 divided by the slow exponential function fit to the tails.....	151
5.19 The underlying transient of the pulses (a) through (i) shifted to their start times.....	154
5.20 A comparison of (a) the transient response of the oxygen pulse (i) of Figure 5.16 divided by the slow exponential and shifted to its start time, (b) the calculated transient response base on the $D/L^2$ value from Table 5-4 and the sticking equivalent to the 10% change in (i) from start to the asymptote.....	156

## List of Tables

2.1 Gas expansion measurements for the total volume of the effusion source. ....	46
2.2 The characteristic rate constant for the effusion source for several gases. ....	50
4.1 Normalized delay and rise times for non-sticking transient flow. ....	88
5.1 A comparison of CTDS and modified King-Wells coverage measurements of O/Pd(110) for several temperatures. ....	138
5.2 The measured and calculated parameters for ten 60s oxygen pulses. ....	142
5.3 The parameters of an exponential fit through the to part of the pulses. ....	149
5.4 The delay, rise, and start times of the pulse estimated from the non-sticking transient model .....	153

## 1 Introduction

Over the past thirty years, the field of Surface Science has developed an array of techniques to probe many aspects of the adsorption, bonding, geometric structure, and reaction pathways of molecules interacting at solid, and even liquid, surfaces [1]. Low energy electron diffraction can often be analyzed to determine surface structure to a precision of better than 0.001nm [2]. Surface vibrational spectroscopies provide detailed information about the intermediates that exist based upon frequency assignments with 0.1% or better accuracy. Electron and phonon band structure has provided a wealth of information for comparison with detailed theoretical calculations of periodic structures. Again band energies can be measured with a precision, e.g. in XPS, of  $\pm 0.05\text{eV}$  at kinetic energies from 500eV to 1500eV. However, one of the most fundamental questions, the absolute coverage or concentration of a species on the surface, remains difficult to quantify with a high degree of accuracy. Methods such as XPS, which have received considerable attention by several group, and M.P. Seah in Particular, achieve an absolute accuracy of  $\pm 20\%$  at best for the surface coverage [3].

The coverage of an adsorbate is inextricably linked to the rate of adsorption onto and the rate of desorption from a surface for a given surface temperature. The kinetic rates are functions of the temperature and coverage on the surface. Measuring the adsorption and desorption rates starting at a known coverage, most typically zero coverage, we can integrate to obtain the coverage thus obtaining the needed kinetic function dependence.

The most common method for the study of desorption kinetics is known as either "Temperature Programmed Desorption" (TPD) or "Thermal Desorption Spectrometry" (TDS) [4-7]. An extensive list of references on TDS is found in Smentkowski *et al.*[8]. In this method, a gas adsorbed on the surface at low temperature desorbs as the sample is heated. Typically the partial pressure established in the vacuum chamber is measured using some type of mass-spectrometer arrangement, or in some cases, particularly in the case of reactive molecules, the direct beam of particles is detected in a line of sight measurement from the surface to the ionizer of the mass-spectrometer. The mass-spectrometer signal must be related to the desorption rate and the sample temperature.

It has been customary to determine the coverage by some secondary means, e.g., low energy electron diffraction (LEED), x-ray photoelectron spectroscopy (XPS), Auger electron spectroscopy, and in the worst case by guessing the saturated structure. Nuclear reaction analysis (NRA)[9] has also so been used occasionally to determine the coverage very accurately but this method is not readily available. Once the coverage is determined , a desorption trace is made and the relationship between the time integral of the mass-spectrometer signal and the coverage establishes the calibration. All of these secondary coverage determinations depend on some assumptions about the surface structure of the adsorbate, with LEED results being the most dependent and NRA the least. The structure of the adsorbate is often a large part of the puzzle to be solved, and therefore assumptions of structure may lead to dubious results. Furthermore, all of these secondary methods have the possibility of decomposing the system to be studied and thereby changing the coverage.

This thesis first addresses the design requirements of a differentially pumped mass spectrometer and then focuses on aspects of molecular fluxes, which must be understood for the quantitative delivery of gases to the sample in dosing procedures or to the spectrometer for calibration purposes. Section 1.1 begins with an overview of the concepts and design criteria of a differentially pumped, calibrated thermal desorption spectrometer. This work formed the basis of my Master's Thesis [10], excerpts of which will be included for completeness in Chapter 2. That work culminated in a test of the CTDS using the O/Pd(110) system, for which NRA measurements exist. The result, summarized in section 1.1.3 below, led to modest modifications of the spectrometer design.

The primary emphasis of the present work, therefore, involves quantifying the spatial distribution and information, which may be extracted from the transient response, associated with losses within a gas doser. These processes enter several aspects of the calibration procedure. We then return to the O/Pd(110) system and re-assess the limitations of the CTDS. Since the previous attempt to measure the absolute oxygen coverage in this adsorption system[10], considerable new results have appeared in the literature, particularly due to the development of scanning tunneling microscopy (STM)[11]. The complexity of the O/Pd(110) system continues to generate discussion and raises a number of related issues regarding the difficulty of preparing ideal, single crystal surfaces. Nevertheless, the system provides a useful measure of the reproducibility of the CTDS, and the contrasting behavior of argon and oxygen allows the theoretical description of transient flow to be tested. Section 1.2 presents the organization of the remainder of the thesis in greater detail.

## 1.1 Overview of the differentially pumped mass spectrometer

In my Masters Thesis[10], I have shown that the mass-spectrometer signal can be related to the desorption rate by directly calibrating the mass-spectrometer signal using a known flow source, if certain conditions of the pumping speed and volume of the vacuum chamber are satisfied. The ability to determine the absolute flux of gases offers a number of applications in quantitative studies of molecule-surface interactions. Foremost, it allows the absolute calibration of a mass spectrometer, which in turn can be used to quantify the flux from a reaction process, such as in thermal desorption spectrometry. The integrated desorption flux may, in favorable circumstances, be related to the absolute coverage. If the absolute quantity and spatial distribution of the gas that impinges on the surface is known, then sticking coefficients can be quantified. In principle, absolute reactive scattering cross-sections can also be obtained.

### 1.1.1 Design criteria for a high performance calibrated thermal desorption spectrometer (CTDS)

The design criteria that we considered to define the properties of a good thermal desorption spectrometer were the following:

- 1) A linear relationship between the desorption rate and the mass spectrometer signal;
- 2) A stable and low baseline mass spectrometer signal;
- 3) A choice of either flux or partial pressure measurement;

- 4) A method of absolutely calibrating the flux versus mass spectrometer signal for different species over a long enough time to complete a typical set of measurements;
- 5) A sensitivity and dynamic range to observe extreme submonolayer desorption features; and
- 6) The ability to measure species which do not form a gas in the chamber, either because they stick to the walls or because they decompose at the walls.

### 1.1.2 The CTDS instrument

Given the above properties, we designed a thermal desorption spectrometer to achieve all but property (6), regarding the reactive or “sticky” species property. The design of a differentially pumped, shrouded mass-spectrometer arrangement was tested. The shroud provides a conical extension to an aperture in front of the sample, thus providing good rejection of species desorbed from other surfaces, e.g. the backside of the sample, the sample heating/mounting structure, and pump or chamber walls (regurgitation). Carefully choosing the shroud geometry established: (i) a small characteristic pumping time facilitating a linear flux versus mass spectrometer signal, (ii) a pumping speed adequate to provide both low baseline and the required sensitivity, and (iii) a conductance from the ionizer to the pump that provides “pumping speed immunity”. Furthermore, the design is based on the assumption of an accommodated ideal gas in the ionizer shroud region, which is pumped through a conductance determined by the shroud geometry. Admitting a gas into the shroud from a calibrated flow source provides a method of calibration of flux versus mass spectrometer signal.

Furthermore, we designed and tested a flow-calibrated gas source, employing: a known volume, a spinning rotor pressure gauge, and a positive shutoff (PSO) capillary leak valve, which provides fluxes typical of thermal desorption experiments.

### 1.1.3 Previous test results of the CTDS system regarding the O/Pd(110) system

The O/Pd(110) system displays two desorption features, the saturation of the higher temperature peak being associated with a c(2x4) structure having a coverage of 0.5 ML. The measurements in the Masters Thesis yielded an estimate of 1.0 ML, suggesting an error by a factor of two. The discrepancy was proposed to be due to a mechanism whereby a substantial fraction of molecules entering the mass spectrometer, with a line-of-sight path to the ionizer, are ionized before they become part of the accommodated gas within the shroud. The calibrating gas should enter the mass spectrometer in a manner that most nearly represents a flux from the sample surface. In thermal desorption spectrometry, the sample temperature, and consequently the desorbing gas velocity is different than at room temperature. Since the probability of ionizing on the first pass decreases with velocity, it is necessary to ensure that both the calibrating gas and the desorbing gas accommodate to the mass spectrometer walls before being measured, i.e. ionized. To address these issues, we have placed a small conical obstruction into the line-of-sight path from the aperture to the mass spectrometer aperture.

Secondly, we chose to use the glass capillary array doser in conjunction with the calibrated effusion source as a "known" source of flux that can be applied to the mass

spectrometer aperture. In order to "know" the source flux, it is necessary to have a theoretical model of the spatial flux distribution as well as methods to measure and compare to the model.

Also of great concern is the extent to which gas exiting from the calibrated flow source does not reach the exit of the doser due to sticking or reactive conversion as it passes along the doser. Achieving steady state behavior can not reveal the extent of these losses. Therefore, we have developed a dynamical model of the transient molecular flow through the doser to determine what information can be extracted regarding surface interactions.

The present work addresses each of these issues and results in a calibrated measurement of the c(2x4) O/Pd(110) coverage that is consistent with the known 0.5 ML coverage.

## 1.2 Summary of the this work

Chapter 2 is an excerpt of my masters thesis[10] included for completeness and ease of referral in subsequent chapters. Chapter 3 develops the theory, measurement and modeling of the glass capillary array doser. In this theory we extend the work of Winkler and Yates [12] to arbitrarily shaped targets and reparameterize the calculations, reducing the order of integration involved in the calculation of the flux density. We further show the use of Fourier transform techniques to more efficiently calculate the total flux to arbitrarily shaped targets.

Chapter 4 initiates a program of study of the transient molecular flow, developing three models from 1-D diffusion, with and without sticking. Although these are the simplest models with uniform tube geometry, we show that they can be used to model the transient flow in the more complicated geometry of our doser, and provide insight into the extent and origin of the sticking losses. Chapter 5 applies the methods of chapters 2 through 4 to the measurement of the c(2x4) oxygen coverage on Pd(110), using calibrated thermal desorption spectrometry (CTDS). This chapter also describes the results of a modified King-Wells[13] method, using the doser and the mass spectrometer in RGA mode for the measurement of gas uptake rates as a function of coverage. Finally, chapter 6 concludes with a review of the results and proposes further work, including suggestions for the development of a new CTDS system, and applications of both the GCA flux theory and the transient theory.

## **2 The Design of a Calibrated Thermal Desorption Spectrometer<sup>1</sup>**

This chapter summarizes the theoretical basis for thermal desorption spectroscopy, leading to design criteria utilized in section 2.2 to specify the differentially pumped mass spectrometer. Section 2.3 describes the calibration and testing of the instrument as achieved at the completion of the Master's degree work.<sup>1</sup>

### **2.1 Theory and basis of the technique**

This chapter describes the requisite principles and theory for understanding the design and operation of the calibrated system. We start with a general explanation of thermal desorption kinetics and the quantities measured in a thermal desorption experiment. Then, needing an estimate of a typical peak desorption rate for a sensitivity analysis, we describe a peak rate analysis following Chan *et al.*[14] This analysis includes a description of the well known Redhead method [15] yielding a relationship between the peak temperature and the desorption activation energy. Chan *et al.* continue, deriving expressions for the coverage at the desorption peak maximum,  $\theta_M$ , and the peak desorption rate, which we use to determine the smallest detectable initial coverage,  $\theta_{min}$ . The second section provides the necessary theory to understand the pressure developed in the shroud during a desorption experiment, including definitions of the characteristic pumping time and the pumping speed immunity. The third section discusses the principles of an effusion

---

<sup>1</sup>Excerpts of chapters 2, 3, and 4 of R.H. Jackson, MS Thesis, University of Maine, 1996 are included here for completeness.

source as a calibrated flow, developing expressions for the flow  $\Phi$  from the source and defining the “characteristic rate constant”  $\alpha$  for the source. We also describe two methods to determine  $\alpha$ . Finally, the fourth section provides a description of the principles and performance of a “spinning rotor gauge,” also known as a “molecular drag gauge,” used to precisely measure the pressure in the effusion source. Except for the measuring range and accuracy, this description is not necessary for the design; however, due to the uncommon nature of the topic we have chosen to include it.

### 2.1.1 The Wigner-Polanyi equation for desorption

The desorption rate,  $r$ , provides an essential part of the information necessary to understand reactions on surfaces. However, the simple measurement of the desorption rate while heating the sample yields only part of the overall desorption rate information. The desorption rate depends on the surface concentration or coverage,  $\theta$ , of the reactants, the temperature,  $T$ , and in many cases the history of the surface,  $t$ ; thus, we write  $r=r(\theta, T, t)$ .

Choosing to avoid systems with history dependence, we proceed to calculate the rate function from the observed rate,  $r_{obs}(t)$ , measured during a single desorption experiment. If we know the coverage at some time  $t_{known}$ , e.g. the coverage is often zero after the desorption has finished, then we may integrate  $r_{obs}$  from the known coverage to obtain the coverage throughout the experiment, i.e.,

$$\theta_{obs}(t) = \theta(t_1) + \frac{1}{n_s} \left| \int_{t_1}^{t_0} r_{obs}(\tau) d\tau \right|, \quad (2.1)$$

where  $n_s$  is the surface concentration of reaction sites.

We are trying to measure the rate function for some range of temperature, T, and coverage,  $\theta$ . Knowing  $\theta_{\text{obs}}(t)$ ,  $r_{\text{obs}}(t)$ , and  $T(t)$ , we construct the rate function over a curve defined by  $\theta_{\text{obs}}(t)$  and  $T(t)$  in the  $\theta$ -T plane. Taking a set of data with different initial coverages, we determine the rate function surface over other curves in the  $\theta$ -T plane until we have determined the rate for the whole region of interest. Having the rate function surface over the  $\theta$ -T plane, we are free to look at either isothermal or isosteric plots of the rate from which the kinetics are more easily understood.

After determining the rate function we must find some method for characterizing it by some small number of parameters, e.g., the isothermal activation energy for desorption, diffusion constants, etc. This characterization requires a model for the kinetics of desorption, which most often starts with the Wigner-Polanyi equation.

The model commonly used for desorption is derived from the activated complex reaction rate theory [4,5,16] and the equation derived from that model is known as the Wigner-Polanyi rate equation expressed by,

$$-\frac{d\theta_i}{dt} = v_i \theta_i^{x_i} \exp\left(-\frac{E_i}{RT(t)}\right) \quad (2.2)$$

where  $\theta_i$  is the surface coverage of the  $i$ th species on the surface,  $v_i$  is a frequency factor related to the frequencies of the vibrations between the surface and the molecule, and  $x_i$  is the order of the reaction related to the type of reaction process occurring on the surface.

Considering equation (2.2) we see that from a theoretical point of view, the easiest rate data to analyze would be isothermal data for which (2.2) is solvable in closed form.

For  $x = 1$  we have

$$\begin{aligned}\theta_i(t) &= \theta_i^0 \exp(-K_i t), \\ K_i &= v_i \exp\left(-\frac{E_i}{RT}\right)\end{aligned}\quad (2.3)$$

There have been successful isothermal experiments [17] providing good isothermal data; however, these experiments involve heating the sample at very high rates then settling to a constant temperature faster than the desorption occurs. Thus, this method requires a carefully designed and well-modeled heating control system.

More commonly [16], the temperature is increased linearly with time while the desorption rate is measured. This process makes the differential equation (2.2) highly nonlinear due to the reciprocal time varying temperature in the exponential; as such it eludes a closed form solution. A number of methods have been developed for determining the parameters  $E_i$ ,  $v_i$ , and  $x_i$  from this type of desorption experiment [4,14,16]. Of these methods the Redhead method [15] is the simplest. Following the Chan *et al.*[14] presentation, the Redhead method assumes values for  $v_i$  and  $x_i$  and relates  $E_i$  to the temperature  $T_M$  where peak desorption rate occurs. Indeed, for first order reactions, i.e., for  $x_i = 1$ ,

$$\frac{E_i}{kT_M^{-2}} = \frac{v_i}{\beta} \exp\left(-\frac{E_i}{RT_M}\right) \quad (2.4)$$

and for second order reactions, i.e. for  $x_i = 2$ ,

$$\frac{E_i}{kT_M^2} = \frac{v_i \theta_0}{\beta} \exp\left(-\frac{E_i}{RT_M}\right) \quad (2.5)$$

where  $\beta$  is the heating rate and  $\theta_0$  is the initial coverage. Both of these expressions can be solved numerically or graphically for  $E_i$  given a value of  $T_M$ . For  $x_i = 1$  Redhead showed that the relationship between  $E_i$  and  $T_M$  is nearly linear and that for  $10^8 \text{ K}^{-1} \leq \frac{v_i}{\beta} \leq 10^{13} \text{ K}^{-1}$  to within 1.5%,

$$\frac{E_i}{RT_M} = \ln\left(\frac{v_i T_M}{\beta}\right) - 3.64 \quad (2.6)$$

We see that knowledge of the “pre-exponential”  $v_i$  is paramount to the application of the Redhead theory. The most commonly assumed value for the pre-exponential is  $v_i = 10^{13} \text{ s}^{-1}$  [18]. However, values of  $v_i$  can vary over many orders of magnitude ---as low as  $10^4 \text{ s}^{-1}$  to as high as  $10^{16} \text{ s}^{-1}$  for first order reactions[18].

In section 2.2.1, we calculate the smallest detectable initial coverage,  $\theta_{\min}$ . By detectable we mean that we can resolve a peak in the desorption rate. In section 2.1.2 we will see that the desorption rate will be linearly related to the pressure in the shroud. Thus, knowing the pressure detection limit of the mass-spectrometer establishes the smallest peak rate observable, which in turn relates to the smallest detectable initial coverage. Following Chan *et al.* [14], we establish the relationship between the initial coverage,  $\theta_0$ , and the peak rate  $r_M$  for first order reactions. This relationship is given by

$$r_M(\theta_0) = v_i n_s \theta_M(\theta_0) \exp(-E_M) \quad (2.7)$$

where  $E_M = \frac{E_i}{RT_M}$  and  $\theta_M(\theta_0)$  is the coverage at the desorption peak given by

$$\theta_M(\theta_0) = \theta_0 \exp\left(-v_1 E \cdot \frac{E_M - 2}{E_M^3} \exp(-E_M)\right) \quad (2.8)$$

where  $E = \frac{E_i}{R \cdot 1K}$  and  $v_1 = \frac{v_i}{\beta} \cdot 1K$ . Later in the theory, Chan *et al.* use the peak width to

establish an expression yielding  $v_i$ , but this is not needed in the present work.

### 2.1.2 The effects of the shroud on the mass spectrometer

We use a simple pumped vacuum chamber as a model for the pressure effects inside of the shroud. Consider a vacuum chamber of volume  $V$  at temperature  $T$  and partial pressures  $P$  with particle number  $N$ . The chamber is pumped by an ultra high vacuum pump, whose pumping speed,  $S = S(P_{inlet}, \Phi, t)$ , where  $P_{inlet}$  is the pressure at the inlet of the pump,  $\Phi$  is the flow, and the time dependence,  $t$ , implies that the pumping speed depends on the history of the pump. We further consider a flow term,  $\Phi$ , where a positive flow enters the chamber. Assuming the ideal gas law  $PV = NkT$  —a good assumption under such rarefied conditions— one writes the differential equation,

$$\frac{dN}{dt} = \Phi - S \frac{N}{V} \quad (2.9)$$

Assuming a constant pumping speed, equation (2.9) has a homogeneous solution given by

$$N(t) = N_0 \cdot e^{-\frac{S}{V}t} \quad (2.10)$$

where  $N_0$  is the initial value of  $N$ . If we further assume zero flow before time  $t = 0$  followed by a step to a constant flow  $\Phi$ , we then find a general solution for  $t \geq 0$ ,

$$N(t) = (N_0 - \frac{V}{S} \cdot \Phi) \cdot e^{-\frac{S}{V}t} + \frac{V}{S} \cdot \Phi \quad (2.11)$$

From this solution, if we define the characteristic pumping time  $\tau = V/S$ , we then see that for changes in the flow  $\Phi$  that are slow compared to the characteristic pumping time,  $\tau$ , the number of molecules in the chamber is proportional to the flow.

In order to calculate the characteristic pumping time  $\tau$  in the case of our shrouded mass-spectrometer, we calculate the pumping speed,  $S_i$ , at the ionizer. This pumping speed  $S_i$  depends on the conductance,  $C$ , from the ionizer to the pump and is related to the pumping speed  $S_p$  of the pump by

$$\frac{1}{S_i} = \frac{1}{C} + \frac{1}{S_p} \quad (2.12)$$

From this expression we notice that if  $S_p \gg C$ , then  $S_i \approx C$ , i.e. if the conductance is small compared to the pumping speed at the pump, then the pumping speed at the ionizer will be “immune” to small changes in the pumping speed at the pump. This observation motivates us to define the “pumping speed immunity”  $\varepsilon$  as

$$\varepsilon = \frac{dS_i}{dS_p} \quad (2.13)$$

which for equation (2.12) yields,

$$\varepsilon = \left( \frac{S_i}{S_p} \right)^2 = \left( \frac{\frac{C}{S_p}}{1 + \frac{C}{S_p}} \right)^2 \quad (2.14)$$

We will use the pumping speed immunity as a constraint on the design of the shroud. From expression (2.14) we see that for  $C \ll S_p$ ,  $\varepsilon \equiv (C/S_p)^2 \approx 0$ , and for  $C \gg S_p$ ,  $\varepsilon \approx 1$ . Using the above expressions we also find

$$\Delta S_i \approx \varepsilon \cdot \Delta S_p \quad (2.15)$$

and

$$\frac{\Delta S_i}{S_i} \approx \sqrt{\varepsilon} \cdot \frac{\Delta S_p}{S_p} \quad (2.16)$$

Thus  $\varepsilon$  provides a function of  $C$  and  $S_p$  that specifies the immunity of  $S_i$  to small changes in  $S_p$ .

Finally, we must have a method for calculating the conductance to the pump. We utilize the results of Monte-Carlo calculations for the transmission probability  $a_{trans}$  of a molecule passing through a particular geometry, given that it has impinged upon the area  $A_{ent}$  defined by the entrance of that geometry. The conductance  $C$  is then given by

$$C = \frac{\bar{v}}{4} \cdot a_{trans} \cdot A_{ent} \quad (2.17)$$

where  $\bar{v}$  is the mean molecular speed given by

$$\bar{v} = \sqrt{\frac{8kT}{\pi \cdot m}} \quad (2.18)$$

for a molecular mass,  $m$ , and a temperature,  $T$ . Tables and graphs of molecular transmission probabilities for a variety of common geometries are available in O'Hanlon[19]. We will use such a table for an annular cylindrical tube to calculate the conductance from the shroud in section 2.2.1.

### 2.1.3 The effusion source as a calibrated flow source

An effusion source is a container of gas in which there is a relatively small orifice through which the gas exits. Consider Figure 2.1 in which a volume,  $V$ , with temperature,  $T$ , and pressure,  $P$ , is connected to a pumped chamber having relatively negligible pressure.

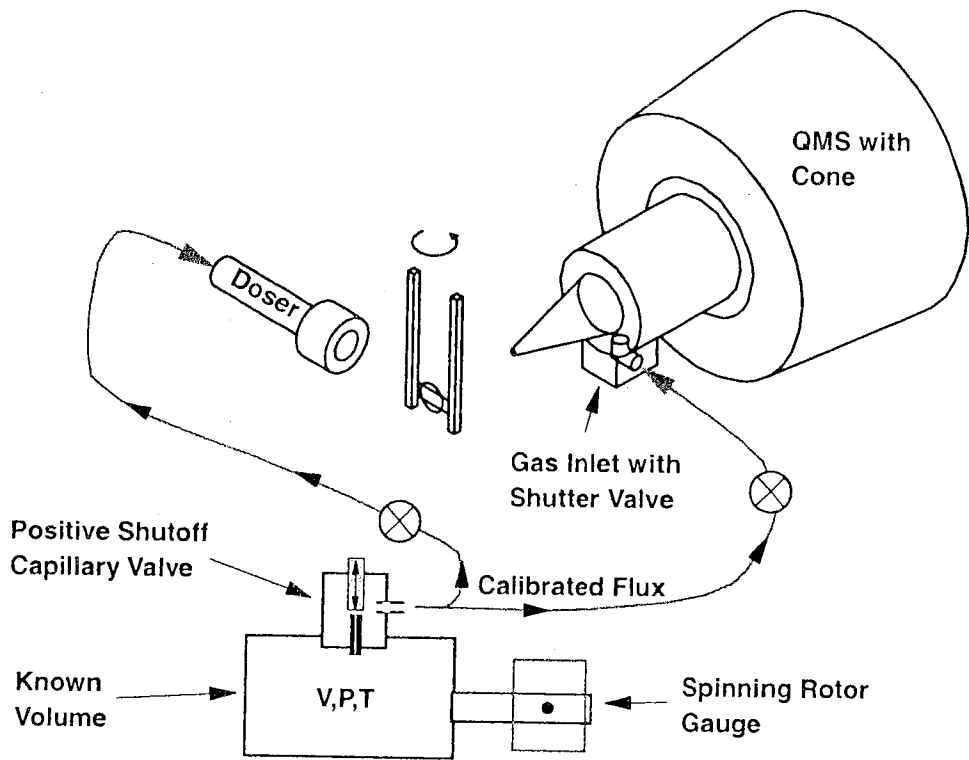


Figure 2.1 Schematic of a calibrated effusion source and the connections leading to the doser and the differentially pumped mass spectrometer

If  $n(t)$  represents the number density of the gas in  $V$ , then the flow  $\Phi$  through the orifice given by conservation of particles is

$$\Phi(t) = -V \frac{dn}{dt} \quad (2.19)$$

If we further assume an ideal gas law  $P = nkT$ , then we may write

$$\Phi(t) = -\frac{V}{kT} \frac{dP}{dt} \quad (2.20)$$

Hence, if we can measure the pressure,  $P(t)$ , then we can differentiate to find the flow,  $\Phi(t)$ .

This is a general expression, which relies only on the validity of the ideal gas law and the conservation of particles in the gas phase. Since we will be using pressures in the molecular flow regime, i.e., the rarefied gas regime, the ideal gas law will hold. However, as we will see, if the gases react with walls, then the conservation of particles in the gas phase will not be completely achieved, though this effect may be reduced by choosing gases that are unreactive with the walls, e.g., we can use argon gas to calibrate the flow.

We now employ a simple model in which, on average, a gas molecule effuses with a probability,  $a_{eff}$ , when it impinges upon the area of the orifice. The expression from the kinetic theory of gases for the impingement of a gas onto a surface[19] is given by

$$flux = \frac{P}{\sqrt{2\pi \cdot mkT}}. \quad (2.21)$$

We then have that the flow,

$$\Phi = \frac{a_{eff} A_{orifice} P}{\sqrt{2\pi \cdot mkT}} \quad (2.22)$$

or, in terms of  $n$ ,

$$\frac{dn}{dt} = -\frac{a_{eff} A_{orifice}}{V} \sqrt{\frac{kT}{2\pi \cdot m}} \cdot n \quad (2.23)$$

which may be solved as

$$n(t) = n_0 e^{-\alpha t} \quad (2.24)$$

where we define the characteristic rate constant  $\alpha$  given by

$$\alpha = \frac{a_{eff} A_{orifice}}{V} \sqrt{\frac{kT}{2\pi \cdot m}} \quad (2.25)$$

The proportionality factor  $\alpha$  varies as  $\sqrt{T/m}$ . Thus, if we can determine a value  $\alpha_1$  for gas of mass  $m_1$ , then we can determine  $\alpha_2$  for a gas of mass  $m_2$  by the relation

$$\alpha_2 = \sqrt{\frac{m_1}{m_2}} \cdot \alpha_1 \quad (2.26)$$

We use this expression to avoid the problem of conservation of particles in the gas phase by first determining  $\alpha_1$  for argon, which does not react with the walls, then calculating  $\alpha_x$  for the  $x$ th gas with molecules of mass  $m_x$ .

We can determine  $\alpha$  in two ways from the data. First, we can calculate  $\alpha$  for two successive data points at times  $t_1$  and  $t_2$  by

$$\alpha(t) = -\frac{1}{n} \frac{dn}{dt} = -\frac{d}{dt} \ln(n) \equiv \frac{\ln\left(\frac{n_1}{n_2}\right)}{t_2 - t_1} \quad (2.27)$$

Second, by equation (2.24) we can fit an exponential function to the entire data set by making a linear regression

$$\ln(n(t)) = \ln(n_0) - \alpha \cdot t \quad (2.28)$$

Finally, from equation (2.22) we may write  $\Phi = K(T,M) P$ . The value  $K$  for some temperature and a particular gas will be specified when designing the leak used in the effusion source in section 2.2.2.

#### 2.1.4 The spinning rotor gauge

The effusion source will require precision pressure measurement for pressures  $10^{-4} \text{ mbar} \leq P \leq 10^{-2} \text{ mbar}$ , since lower pressures will aggravate the effects of wall reactions and higher pressures no longer lie in the molecular flow regime. A “spinning rotor gauge” [20,21], or, as otherwise called, a “molecular drag gauge”, measures the pressure for a pressure range  $10^{-7} \text{ mbar} \leq P \leq 10^{-1} \text{ mbar}$  with an accuracy of  $\pm 3\%$  and with a precision of  $10^{-10} \text{ mbar}$ , which easily covers the pressures in question.

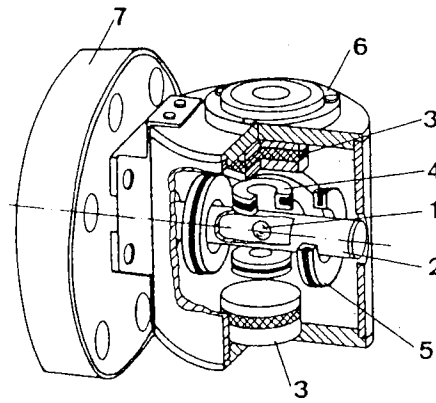


Figure 2.2 The spinning rotor gauge from the Leybold-Infocon VM211 manual.

Figure 2.2 shows a drawing of the spinning rotor gauge. A small (4.5 mm dia.) stainless steel ball is suspended in a magnetic field within a tube connected to the vacuum chamber. Due to magnetic defects present in most balls a small magnetic moment exists. Applying an oscillating magnetic drive field via two coaxial coils drives the ball into rotation. Similarly, when the drive field is removed another set of coils detects the spinning magnetic moment, thus enabling the determination of the period of rotation. As molecules of gas impinge isotropically on the rotating spherical ball, an amount of

tangential momentum is given up to the ball as characterized by the coefficient of tangential momentum transfer,  $\sigma$ , defined by

$$\sigma = \left\langle \frac{c_{\parallel} - c_{\parallel f}}{c_{\parallel}} \right\rangle_{avg.} \quad (2.29)$$

where the  $c$ 's are the incident and final velocities tangent to the surface as shown in Figure 2.3.

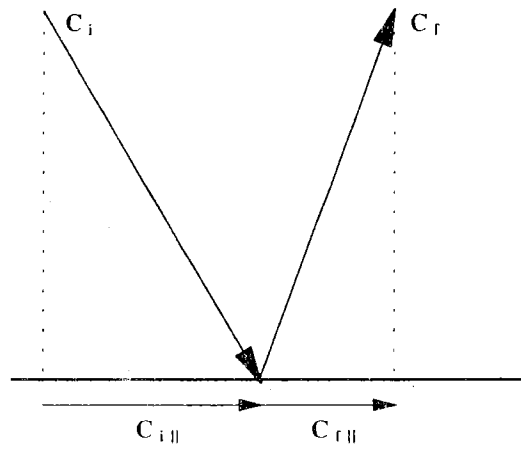


Figure 2.3 Velocity vectors for impingement on the ball.

The rotational speed of the ball decelerated by molecular collisions is given by

$$\omega(t) = \omega_0 \exp \left( -\frac{10\sigma \cdot P}{d_B \rho_B} \sqrt{\frac{M}{2\pi \cdot RT}} \cdot t \right) (rev/sec) \quad (2.30)$$

where  $d_B$  is the ball diameter,  $\rho_B$  is the ball density, and  $M$  is the molecular weight of the gas. Solving equation (2.30) for the pressure, we have

$$P = -\frac{d_B \rho_B}{10\sigma} \sqrt{\frac{2\pi \cdot RT}{M}} \cdot \frac{1}{t} \ln \left( \frac{\omega(t)}{\omega_0} \right) \quad (2.31)$$

The value  $-\frac{1}{t} \ln\left(\frac{\omega(t)}{\omega_0}\right)$  is referred to by the gauge manufacturer as the "DCR" value for deceleration; indeed, this value is the relative deceleration, since

$$-\frac{1}{t} \ln\left(\frac{\omega(t)}{\omega_0}\right) = -\frac{\ln(\omega(t)) - \ln(\omega_0)}{t} \approx -\frac{d}{dt} \ln(\omega(t)) = -\frac{1}{\omega} \frac{d\omega}{dt} \quad (2.32)$$

and since we are interested in a single ball revolution,  $t$  is small.

We must relate the rhs of equation (2.32) to some measurements of the periods of rotation of the ball. Let  $\tau_i$  be the period of the  $i$ th revolution of the ball. The average rotation speed for the  $i$ th revolution is  $\omega_i = \frac{1}{\tau_i}$  and

$$\frac{d\omega}{dt} \equiv \frac{1}{\tau_{avg}} \left( \frac{1}{\tau_{i+1}} - \frac{1}{\tau_i} \right) \quad (2.33)$$

from which we have

$$-\frac{1}{\omega} \frac{d\omega}{dt} = \left( \frac{\tau_{i+1} - \tau_i}{\tau_{avg}^2} \right) \quad (2.34)$$

where we have approximated  $\tau_{i+1}$  and  $\tau_i$  by  $\tau_{avg} = (\tau_{i+1} + \tau_i)/2$  everywhere except in the difference. We then have an expression for the pressure given by

$$P = -\frac{d_B \rho_B}{10\sigma} \sqrt{\frac{2\pi \cdot RT}{M}} \cdot \left\langle \frac{\tau_{i+1} - \tau_i}{\tau_{avg}^2} \right\rangle_{t_m} \quad (2.35)$$

where the average is over all revolutions within the measuring time,  $t_m$ . In our case it is convenient to have the spinning rotor gauge report the number density directly as given by

$$n = -\frac{N_A d_B \rho_B}{10\sigma} \sqrt{\frac{2\pi}{MRT}} \cdot \left\langle \frac{\tau_{i+1} - \tau_i}{\tau_{avg}^2} \right\rangle_{t_m} \quad (2.36)$$

Determining the value of  $\sigma$  calibrates the gauge, however, the values of  $\sigma$  for smooth stainless steel balls are very nearly unity, and the manufacturer supplied balls have  $\sigma = 1.00 \pm 3\%$ . Furthermore, Figure 2.4 shows a histogram of  $\sigma$  for 68 balls, all nearly unity.

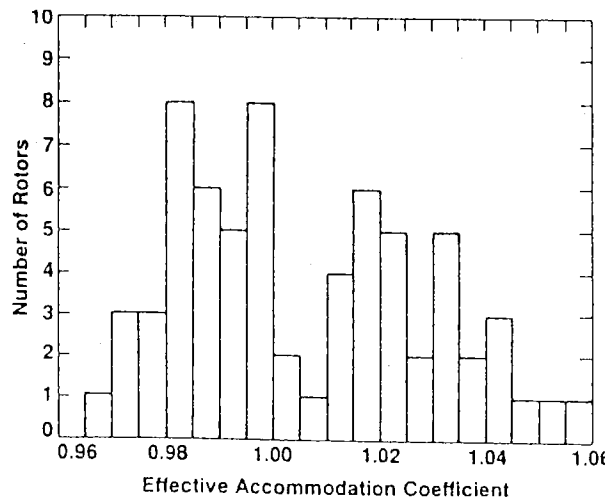


Figure 2.4 Histogram of  $\sigma$  for 68 smooth stainless steel ball bearings. Taken from Dittmann *et al* [21] p. 3358 Fig. 3.

The stability of the spinning rotor gauge is dependent on the stability of  $\sigma$  in which Figure 2.5 shows that the stability of  $\sigma$  is within 0.5% for 20 months.

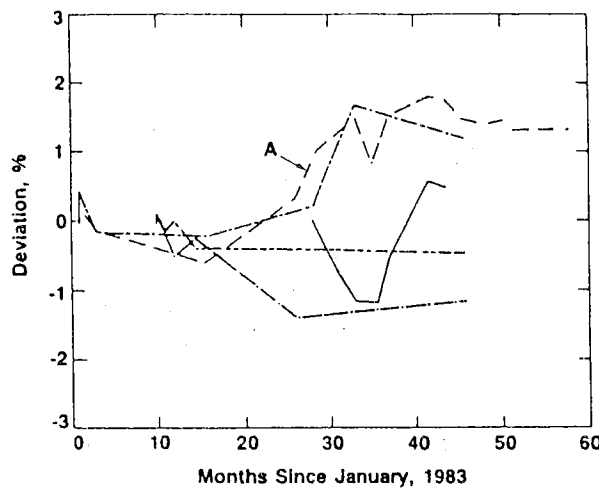


Figure 2.5 Changes from the initial values of  $\sigma$  of five NIST rotors. Taken from Dittmann *et al* p. 3357 Fig. 2.

The manufacturer provides a plot of the typical measurement uncertainty versus pressure as shown in Figure 2.6.

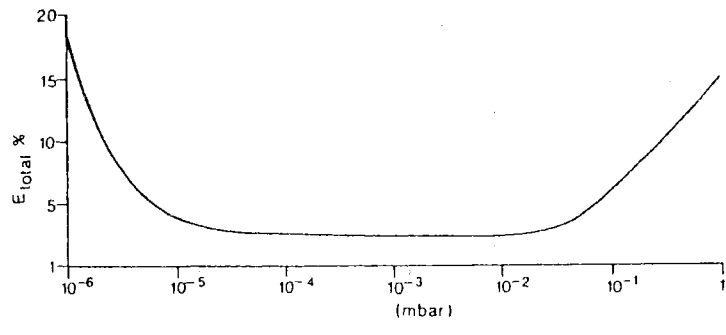


Figure 2.6 Typical measurement uncertainty,  $E_{total} \%$  versus pressure in the Leybold-Infocon VM211 spinning rotor gauge.

## 2.2 Design of the instrument

This section focuses on the design of the calibrated thermal desorption spectrometer (CTDS) and the associated, calibrated effusion source. We will also briefly discuss the channel array doser and the general system layout and instrumentation.

The properties of a good quantitative CTDS were discussed in chapter 1 concluding with a proposed layout of a shrouded differentially-pumped mass-spectrometer with a conical extension to the front of the sample. The spectrometer is pumped by a separate 360 L/s turbomolecular pump, while the sample is mounted in the main chamber, which is pumped by an ion pumped and a titanium sublimation pump. The theory concerning the desorption process and the pumping of the ionizer region within the shroud were discussed in section 2.1.2, providing quantitative relationships between: the flow of gas into the shroud, the pressure at the ionizer, the pumping speed at the ionizer, the pumping speed at the pump, and the conductance from the ionizer to the pump. Three characteristic quantities were derived from these relationships, namely: the characteristic pumping time  $\tau$ , the minimum detectable coverage for first order desorption  $\theta_{\min}$ , and the pumping speed immunity  $\epsilon$ . In addition we must consider three other quantities, namely: the baseline pressure  $P_{base}$ , the dynamic range of continuous operation  $\Delta P_{dyn}$ , and the maximum pressure generated at the ionizer  $P_{max}$ . Using these quantities, we have developed five design criteria to guide the choices of geometry, materials, and other details of the configuration. These criteria are as follows:

- 1) Minimize the characteristic pumping time  $\tau$ .

- 2) Maximize the peak intensity to obtain at least a minimum detectable coverage of  $\theta_{\min} = 10^4$ .
- 3) Choose a conductance to provide substantial immunity from variations in pumping speed such that at least  $\epsilon < 10\%$ , preferably  $\epsilon < 1\%$ .
- 4) Ensure that typical desorption experiments generate pressures at the ionizer within the dynamic range  $\Delta P_{\text{dyn}}$  preferably with the mass spectrometer in SEM mode.
- 5) Minimize the baseline pressure  $P_{\text{base}}$ .

In the following sections, each of these constraints are applied to the spectrometer design.

### 2.2.1 The cone geometry and mass spectrometer modifications

We now turn to the determination of the preferred characteristics and geometry of the CTDS. Figure 2.7 shows the basic configuration and dimensions. A cylindrical shroud, placed coaxial to the mass-spectrometer's quadrupole and ionizer is extended with a conical shroud close to a point in front of the sample.

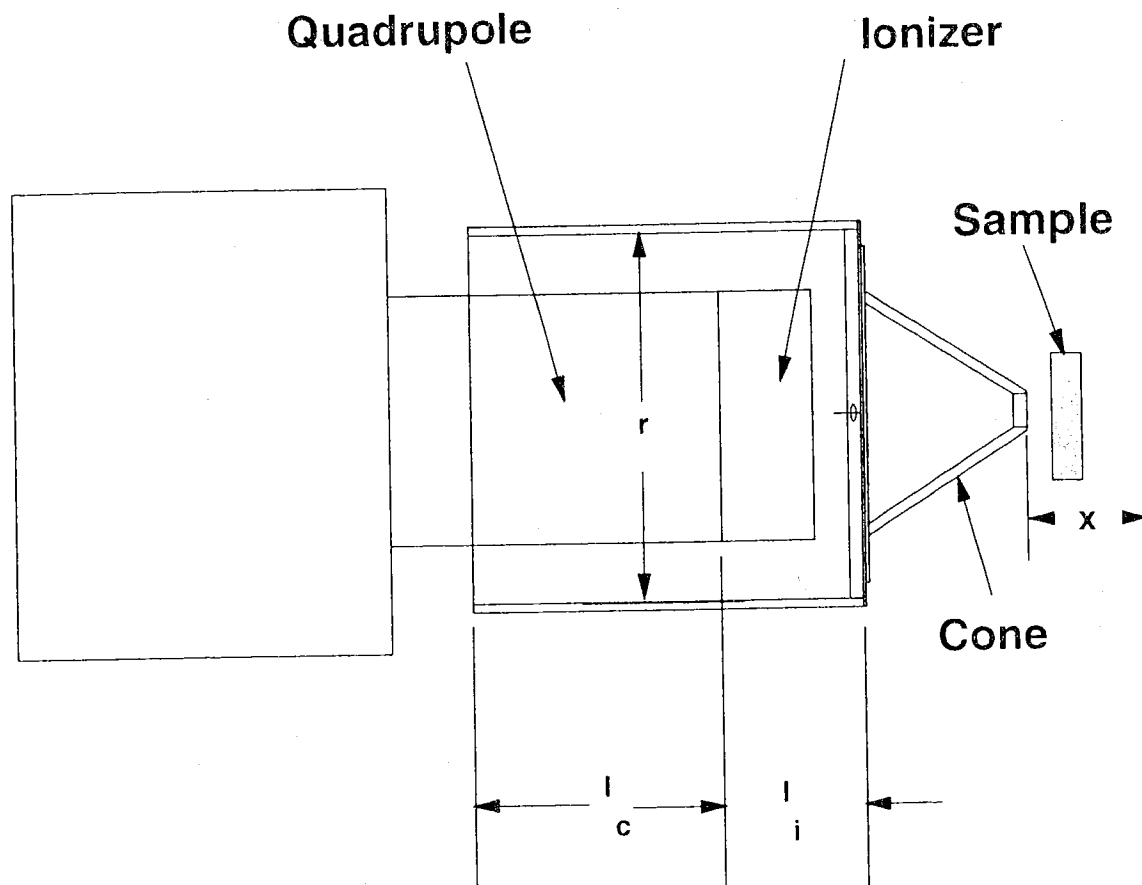


Figure 2.7 The basic configuration of the CTDS with the important dimensions. Note: the differential pumping seal is shown in Figure 5.1

We somewhat arbitrarily choose the volume  $V_i$  of the ionizer region to be the volume of the cone plus the volume of the cylindrical shroud of length  $l_i$  and radius  $r$  from the end of the quadrupole to the end where the cone attaches. We have ignored the effects of the volume displaced by the ionizer and the higher temperature of the filament, but include an estimate of the elevated temperature,  $T = 350$  K (later measured to be 330 K), of the cylindrical shroud due to the filament. The conductance from the ionizer to the pump is determined by the pumping speed  $S_{exit}$  at the back exit of the shroud and by the

conductance of the annular region defined by the remaining length of the cylindrical shroud and the tube containing the quadrupole of outer radius  $r$ , and inner radius  $r_0$ , and length  $l_c$ .

The ultra high vacuum chamber, mass-spectrometer, and other available vacuum hardware impose further constraints on the dimensions of the CTDS. However, it is our opinion that these constraints are typical, and, as we will see, they turn out to be insignificantly limiting. These further constraints are as follows:

- 1) The cone must be longitudinally translatable in order to provide clearance for both the sample holder, when the sample is moved to the Electron Energy Loss Spectrometer position, and the doser, when it is moved to the sample position.
- 2) The flange port available for the instrument is a standard 6 inch conflat™ flange with 4.00 inch O.D. 1/16 inch wall tubing, thus limiting the diameter of the instrument to the I.D. of the tubing, minus clearance.
- 3) The flanges and valves used to provide the differential pumping necessitated extending the mass-spectrometer from its flange in order to bring it close enough to the sample position.
- 4) The available Leybold TMP360 turbo molecular pump has an inlet pumping speed of 360 liters  $s^{-1}$ .

We will proceed to develop the design by first determining the range of pumping speeds that fit the constraints, then second determining the dimensions that give that range

of pumping speeds while analyzing the other design parameters, and finally choosing the dimensions and analyzing the performance at those dimensions.

Assuming a steady state flow of gas into the shroud, we proceed as in section 2.1.2 using equation (2.11) to calculate the pressure at the ionizer as a function of pumping speed  $S_i$  at the ionizer and flow  $\Phi$  into the shroud. We look for a possible design region in the ( $S_i$ - $\Phi$ ) plane, such that the pressure satisfies three criteria: the detection limit, the maximum pressure, the available pumping speed, and the minimum detectable coverage sensitivity.

First consider the pressure detection limit. The ultimate pressure detection limit of the mass-spectrometer is  $\sim 10^{-13}$  mbar, however, for more practical measurements we degrade the detection limit to  $10^{-12}$  mbar. This has the effect of reducing noise, increasing the allowable scan speeds, and detecting changes above baseline pressures which are typically  $\sim 10^{-11}$  mbar. Therefore, for our detection limit we have

$$10^{-12} \text{ mbar} \leq P = \frac{kT\Phi}{S_i} \quad (2.37)$$

yielding,

$$\log_{10}\left(\frac{\Phi_{\text{det}}}{\text{molecules/s}}\right) \geq 7.3 + \log_{10}\left(\frac{S_i}{\text{l/s}}\right) \quad (2.38)$$

This detection limit line is shown in Figure 2.8 and the region below this line is shaded to show that we have rejected that region.

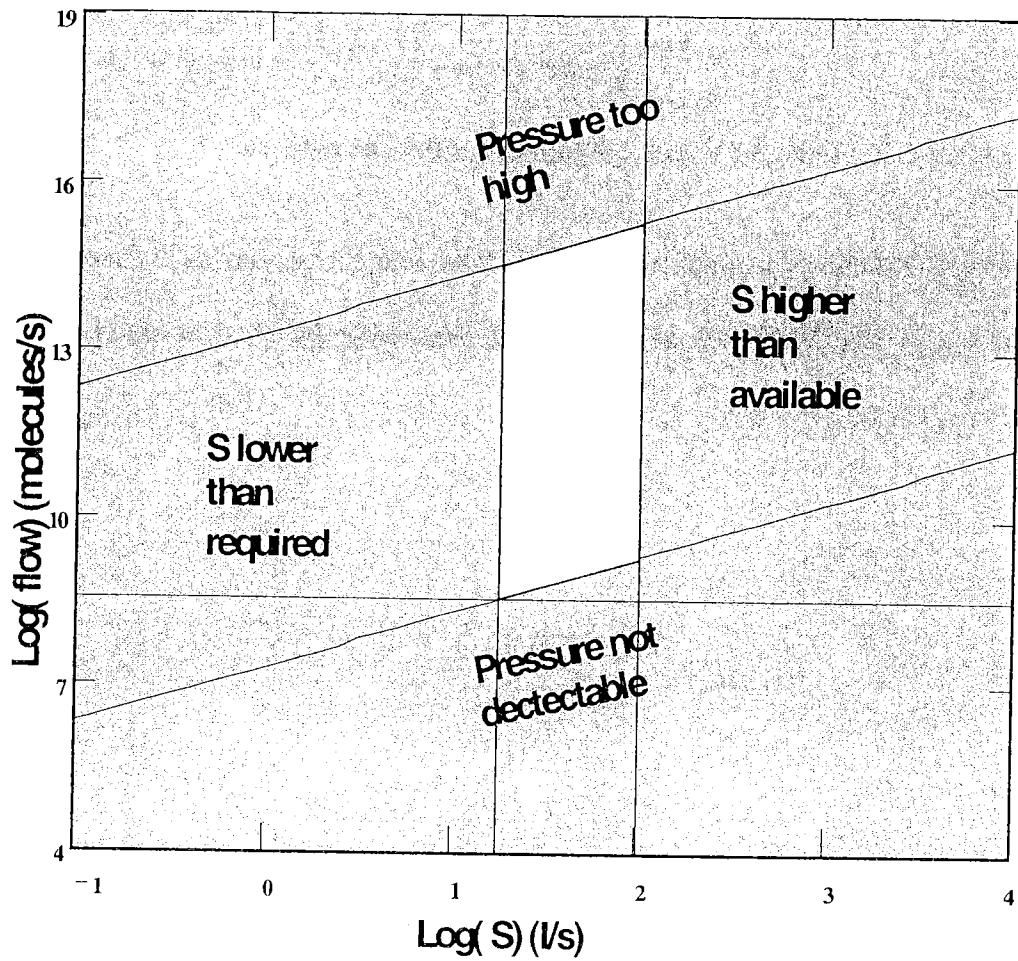


Figure 2.8 Pressure and flow criteria in the S-Φ plane

Next we consider the high pressure operating limit, which we have chosen to be  $10^{-6}$  mbar, thus allowing SEM operation at moderate gains and insuring linear operation. Therefore, for our high pressure limit we have

$$10^{-6} \text{ mbar} \geq P = \frac{kT\Phi}{S_i} \quad (2.39)$$

yielding,

$$\log_{10}\left(\frac{\Phi}{\text{molecules/s}}\right) \leq 13.3 + \log_{10}\left(\frac{S_t}{l/s}\right) \quad (2.40)$$

as shown in Figure 2.8 with the region above the line rejected.

Figure 2.9 shows a graph of the peak flow into the shroud as a function of the initial coverage, as calculated from the peak rate function of the Chan, *et al.*[14] theory, discussed in section 2.1.1.

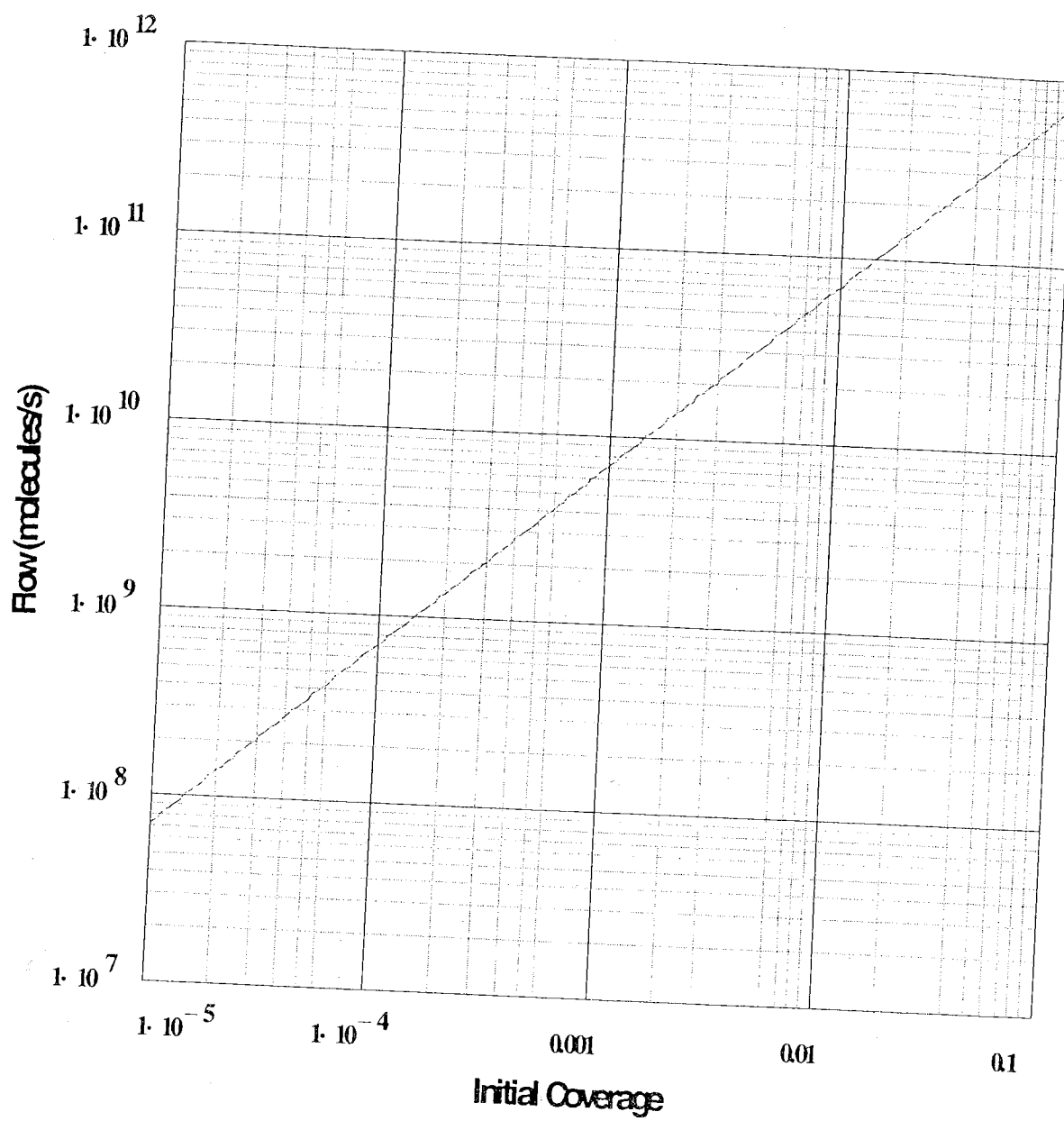


Figure 2.9 Peak first order desorption flow as a function of initial coverage for  $E_d = 200$  KJ/mole,  $\beta = 5$  K/s,  $v_0 = 10^{12}$ , and  $0.1 \text{ cm}^2$  cone aperture.

In Figure 2.8 we show a horizontal line intersecting the detection limit, corresponding to the initial coverage  $\theta_0 = 5 \times 10^{-5}$ . We choose the intersection of the  $\theta_0 = 5 \times 10^{-5}$  line and the

detection limit as defining the lower limit on S, because it just achieves the peak sensitivity required, leaving a range of choices of S and otherwise maximizing the pumping speed to minimize the baseline pressure.

A simple vacuum calculation shows that the pumping speed at the outlet of the shroud will be approximately 100 l/s. Thus, Figure 2.8 shows the range of pumping speeds and corresponding ranges of flow into the shroud. We can use these ranges as a guide for our subsequent design calculations. It is fortuitous that the ranges of flow all encompass the typical flows that would be generated, e.g., if the initial coverage is unity then a peak flow of  $7 \times 10^{12}$  molecules/s would be established in the model of Figure 2.9. This flow is an order of magnitude below the lowest maximum flow in the design region, thus allowing for other desorption processes where there might be larger peaks, e.g., two dimensional phase transitions which can desorb in very sharp intense peaks [22-24].

We must now consider the more complicated issues surrounding the dimensions  $l_c$ ,  $l_i$ , and  $r$ . The constraints imposed by the dimensions of the chamber are:

$$\begin{aligned} 1.95\text{cm} &\leq r \leq 4.42\text{cm} \\ 0\text{cm} &\leq l_c \leq 7.52\text{cm} \\ 5.03\text{cm} &\leq l_i \leq 28.26\text{cm} \end{aligned} \tag{2.41}$$

We must also consider the longitudinal motion of the shroud indicated by  $x$  in Figure 2.7. However, for the current analysis we will fix  $x = 0.64$  cm, which represents the typical sample position. After choosing the dimensions we will vary both  $x$  and the mass  $M$  of the gas as part of the design performance analysis.

In order to continue the analysis we must have some means of calculating the conductance of the annular section. This is accomplished by using the transmission probability plot in Figure 2.10.

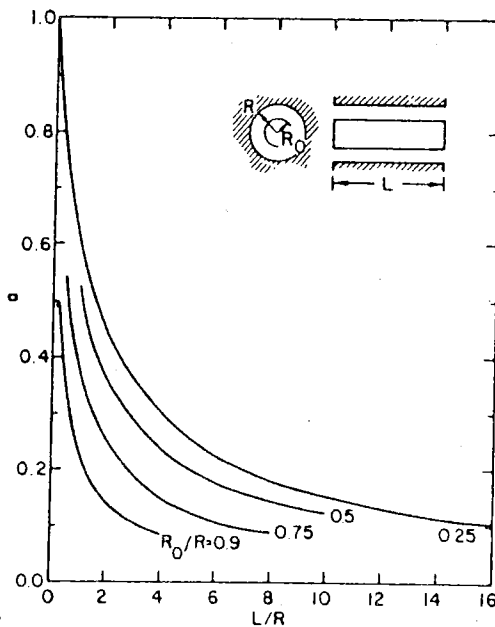


Figure 2.10 Molecular transmission probability of an annular cylindrical pipe. Taken from *A Users Guide to Vacuum Technology* 2<sup>nd</sup> ed. by John F. O'Hanlon in which it was reprinted with permission from *Le Vide*, No. 103, p. 42, L. L. Levenson *et al.* Copyright 1963 Societe Francaise des Ingeneurs et Techiciens du Vide.

For ease of calculation, the data in this graph was digitized and fit with a two dimensional cubic spline in Mathcad™ 6.0. Having the spline fit enabled us to create a function describing the transmission probability as a function of  $l_c/r$  and  $r_0/r$ ,  $\text{transprob}(l_c/r, r_0/r)$ , which was used in the subsequent calculations of conductance  $C$ , pumping speed  $S_i$ , characteristic pumping time  $\tau$ , and pumping speed immunity  $\varepsilon$ . The results of these calculations are reproduced here in Figure 2.11 through Figure 2.14.

In Figure 2.11, the conductance  $C$  and the ionizer pumping speed are shown as two contour plots over the  $l_c$ - $r$  plane. The pumping speeds are all within the desired range; however, the conductances are too high except for in the lower right corner, i.e., for  $l_c$  maximum and  $r$  minimum, where the conductance is below 50 l/s.

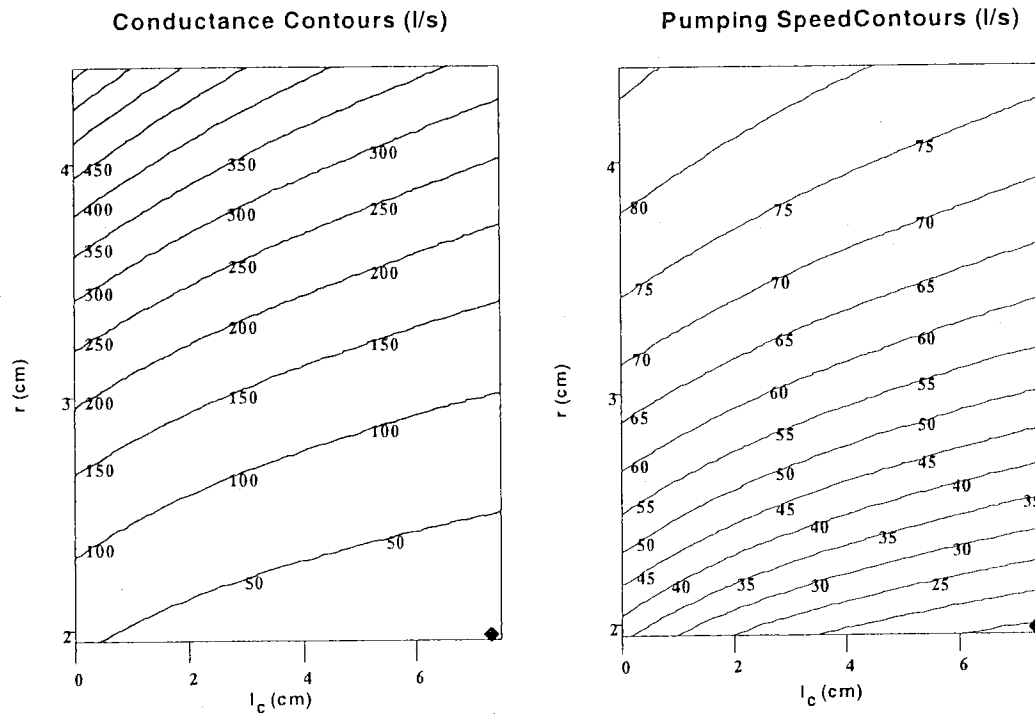


Figure 2.11 The contour plots of conductance from and pumping speed at the ionizer for values of  $r$  and  $l_c$

The effect of high conductances is also apparent in the pumping speed immunity contour plot of Figure 2.12, where the lower right corner has values of pumping speed immunity below 5%. The characteristic pumping time,  $\tau$ , shown in Figure 2.12 as a contour plot over the  $l_i$ - $r$  plane reveals a minimum at approximately  $r = 3.0$  cm for  $l_i = 5.03$  cm.

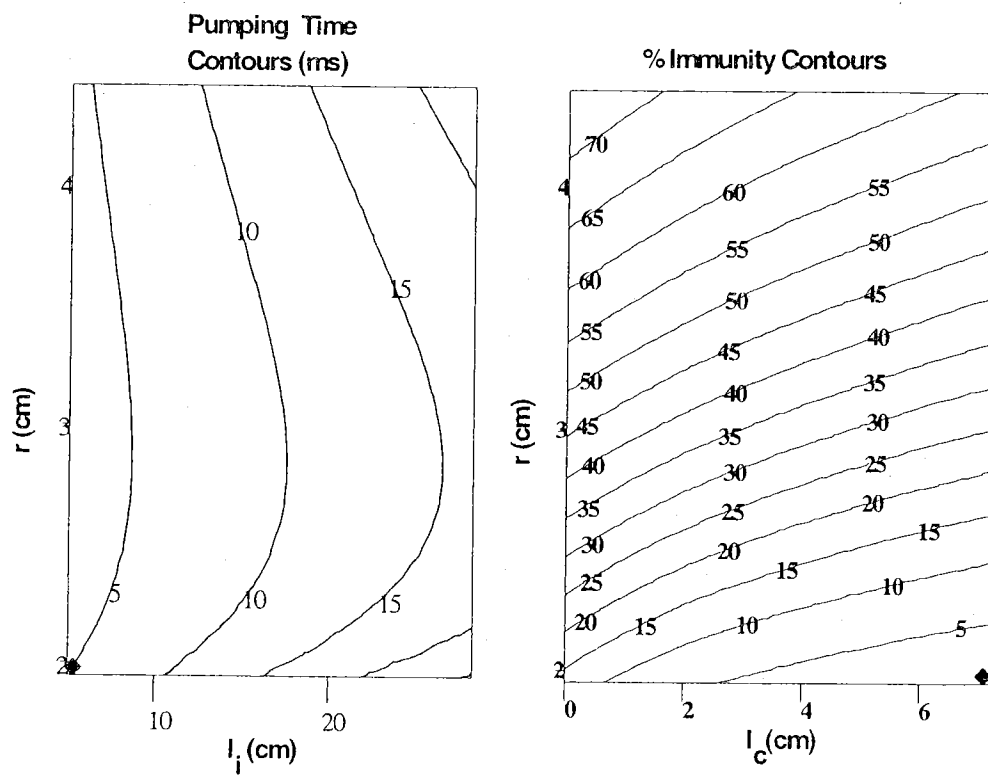


Figure 2.12 Contour plot of the characteristic pumping time over the  $l_i$ - $r$  plane and a contour plot of the percent pumping speed immunity over the  $l_c$ - $r$  plane.

In the above four contour plots the diamond indicates our actual design choice. The conductance, the pumping speed at the ionizer, and the pumping speed immunity optimize the design criteria for this choice and the characteristic pumping time is acceptable. The actual design values used for  $l_c$ ,  $l_i$ , and  $r$  are

$$\begin{aligned}l_c &= 7.22 \text{ cm} \\l_i &= 5.00 \text{ cm} \\r &= 1.975 \text{ cm.}\end{aligned}$$

Figure 2.13 shows the conductance, C, the percent pumping speed immunity,  $\% \epsilon$ , and the characteristic pumping time,  $\tau$ , for the design choice while varying the cone position x from its typical position  $x = 0.63$  cm. All values are well within the design criteria.

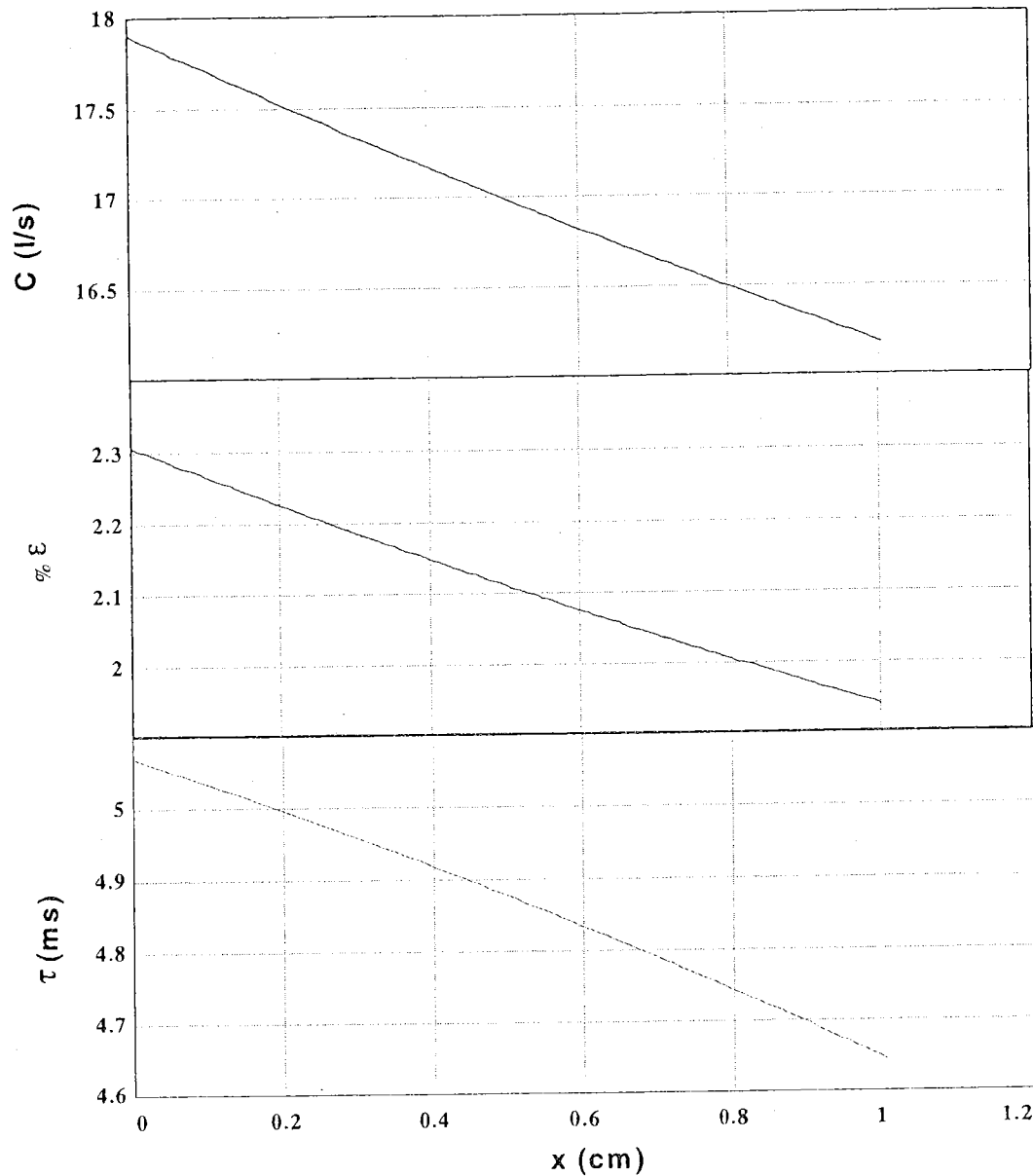


Figure 2.13 C,  $\% \epsilon$ , and  $\tau$  for the chosen design versus the cone position.

Figure 2.14 shows the conductance  $C$ , the percent pumping speed immunity  $\% \epsilon$ , and the characteristic pumping time  $\tau$  for the design choice, while varying the molecular weight  $M$ . All of these values become less favorable below 10 g/mole and we therefore expect hydrogen CTDS to be less than optimum for the chosen design. This could be changed by reducing the conductance of the shroud and by increasing the pumping speed for hydrogen, e.g. by using a cryopump rather than a turbomolecular pump.

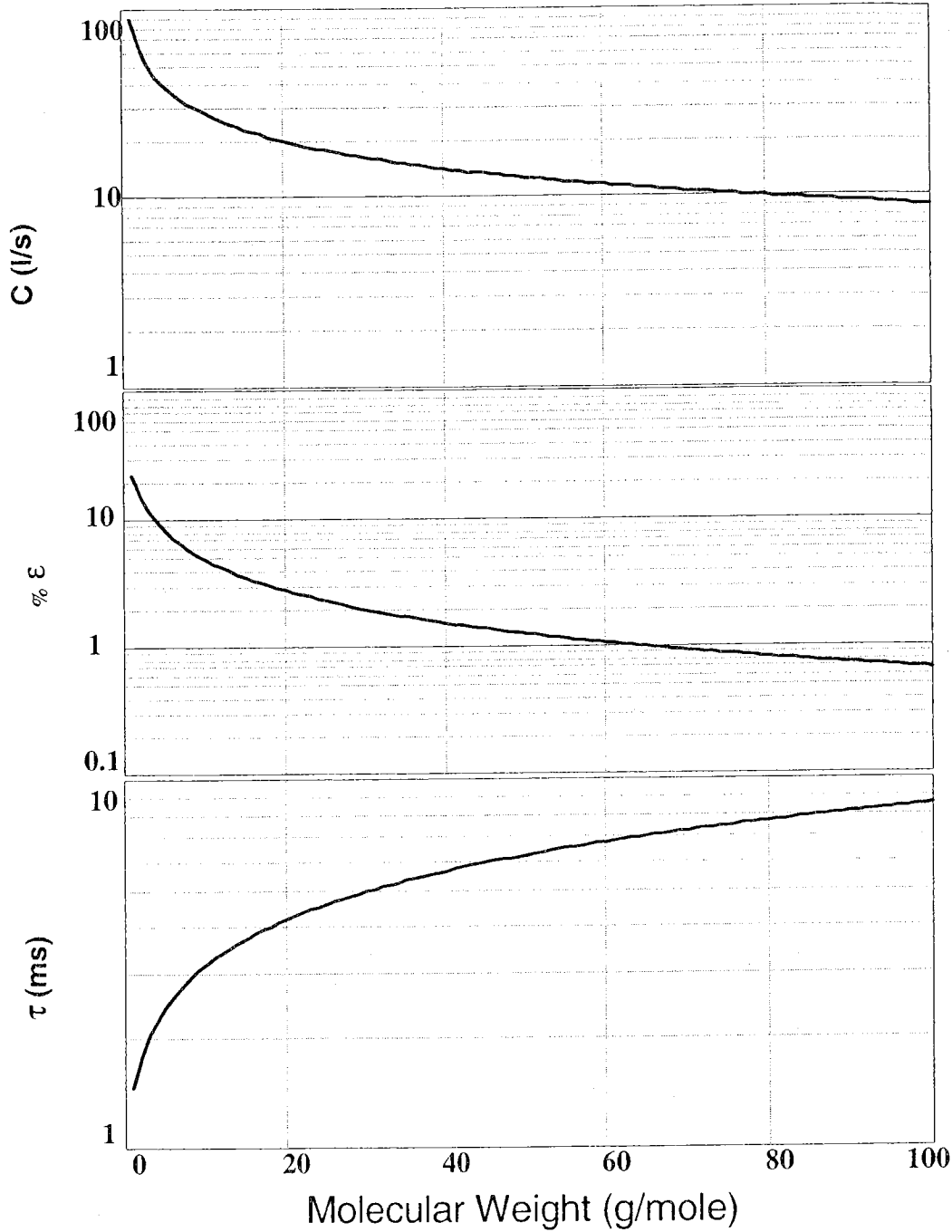


Figure 2.14  $C$ ,  $\% \epsilon$ , and  $\tau$  for the chosen design versus the molecular weight of the gas used.

### 2.2.2 The effusion source

The design of the effusion source includes four major considerations: the range of the measurable flow, the rate of change in the flow, adsorption of gases on the walls, and a method of determining the volume.

First consider the range of flow, which we would like to be comparable to the flows established during desorption experiments, i.e.,  $\sim 10^{13} \text{ s}^{-1}$ , but also allowing for dosing flows at about  $10^{15} \text{ s}^{-1}$ . Figure 2.6 showed the typical uncertainty versus pressure for the spinning rotor gauge, which exhibits a wide flat region of low uncertainty centered roughly around  $10^{-3} \text{ mbar}$ . We chose the specification of the positive shutoff capillary leak valve to flow nitrogen gas at  $10^{13} \text{ s}^{-1} \pm 40\%$  at a pressure  $10^{-3} \text{ mbar}$ . The tolerance was a manufacturer option which eliminated more careful testing and selection of a leak of tighter tolerance, an unneeded expense since we planned to calibrate the capillary valve ourselves.

### 2.3 Calibration and testing

In this section, the calibration procedure is broken down into several steps, describing calibration of the volume of the gas chamber, calculation of the gas flow from the spinning rotor gauge measurements, and the mass spectrometer flow gain. The section concludes with the test results for oxygen desorption from Pd(110) obtained within the Masters degree work..

### 2.3.1 The gas chamber volume calibration

The volume of the effusion source, including the connections to the capillary valve is determined by expanding a reference volume  $V_{ref}$  of gas at a measured pressure  $P_{before}$  into the total volume  $V_{tot}$ , after which the pressure  $P_{after}$  is again measured. The total volume  $V_{tot}$  is then determined by the relationship

$$V_{tot} = \frac{P_{before}}{P_{after}} \cdot V_{ref} \quad (2.42)$$

The reference volume has been determined by weighing the reference volume assembly when open and dry and when filled with distilled water, determining  $V_{ref}$  from the mass difference and the density of water  $\rho = 0.99821$  g/ml at 20° C. Figure 2.15 shows the reference volume, constructed from a stainless steel mini-conflat™ tee and varian gold seal UHV valve v1. The figure also shows a second valve v2 (Whitney toggle valve with Swaglok connections) between v1 and a portable turbo-molecular pump. The inlet of this second valve is more easily filled with water than the UHV valve with its bellows and other internal convolutions.

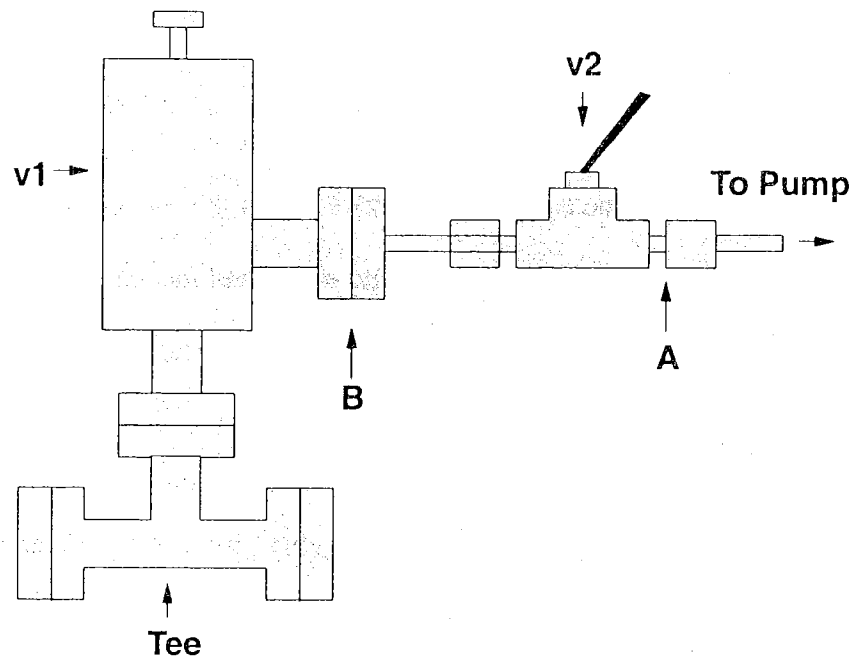


Figure 2.15 Reference volume calibration assembly.

The weighing and filling procedure to determine the reference volume is as follows:

- 1) The assembly is broken at B and the dry mass  $M_{dry}$  of the tee plus v1 assembly is determined by weighing.  $M_{dry} = 738.3 \pm 0.1 \text{ g}$ .
- 2) The assembly is reconnected at B and evacuated to  $10^{-4}$  torr followed by closing v1 and v2 in sequence.
- 3) The assembly is broken at A and a small glass pipet is used to fill the now exposed end of v2 with distilled water.
- 4) The assembly is immersed in distilled water and the end of v2 is flushed with the pipet to dislodge any remaining air (none was observed).

- 5) While immersed, v1 and v2 were opened in sequence and the assembly is allowed to fill for 10 minutes.
- 6) Valve v1 is closed, the assembly is removed from the water, broken at B. The water is shaken and pipeted from the exposed end of v1, and the tee plus v1 assembly is placed in a drying oven for 1 hour at 80° C, followed by cooling for 1 hour at room temperature.
- 7) The filled mass  $M_{filled}$  of tee plus v1 assembly plus water is determined by weighing.

$$M_{filled} = 765.25 \pm 0.1 \text{ g.}$$

The masses determined by this procedure yield a difference  $\Delta M = 26.95 \pm 0.1 \text{ g } (\pm 0.7\%)$ .

Thus, using the density of water at 20° C,  $V_{ref} = 27.00 \pm 0.2 \text{ ml } (\pm 0.7\%)$ . The tee plus v1 assembly was emptied and reattached to the effusion source.

The determination of the total volume  $V_{tot}$  of the effusion source as described by equation (2.42) is performed using the spinning rotor gauge to measure pressures before and after expansion. It is important to note that the uncertainty in this expansion method is not determined by the 3% uncertainty in the tangential momentum transfer coefficient  $\sigma$ , which is an uncertainty in our knowledge of its fixed stable value. Since the expansion method involves a ratio of measured pressures and since  $\sigma$  appears as a factor in the expression for the pressure, equation (2.35),  $\sigma$  is divided out of the total volume calculation leaving

$$V_{tot} = \frac{\left\langle \frac{\tau_{i+1} - \tau_i}{\tau_{avg}} \right\rangle_{t_m}^{before}}{\left\langle \frac{\tau_{i+1} - \tau_i}{\tau_{avg}} \right\rangle_{t_m}^{after}} \cdot V_{ref} \quad (2.43)$$

These averages have an absolute uncertainty equivalent to  $10^{-8}$  mbar, which is determined by the residual drag offset correction statistics. For measurements at a pressure of  $3 \times 10^{-4}$  mbar, this offset uncertainty yields a 0.003% uncertainty in the ratio of the pressures. Thus, the uncertainty of the total volume is determined by the 0.7% uncertainty of the reference volume. Since our flow calculations will be uncertain by the 3% uncertainty in  $\sigma$ , this 0.7% uncertainty is not considered significant, though it may be improved by more precise weighing.

We anticipated the total volume at approximately 400 ml, which provides an expansion ratio of 27:400. We therefore expect about an order of magnitude decrease in the pressure upon expansion. The mid  $10^{-4}$  mbar range provides an easily measurable final pressure and allows the expansion to start from the mid  $10^{-3}$  mbar range, also easily measurable. Thus we chose  $\sim 5 \times 10^{-3}$  mbar as the starting pressure. The procedure for the expansion is as follows:

- 1) The effusion source is evacuated to below  $10^{-6}$  mbar and is baked at  $150^\circ C$  for at least 24 hours.
- 2) The spinning rotor gauge operated for at least 24 hours at a pressure below  $10^{-8}$  mbar while the residual drag offset is monitored and stabilized according to the users manual.

- 3) With the reference valve v1 opened and the pump-out valve  $v_e$  closed , argon gas is leaked into the effusion source to a pressure of approximately  $5 \times 10^{-3}$  mbar.
- 4) Ten values of the pressure are taken in sequence, each with a 20 second measuring time, after which v1 is slowly closed to avoid compression of the gas.
- 5) The pump-out valve to the turbomolecular pump,  $v_e$ , is opened and the effusion source is pumped for ten minutes.
- 6)  $v_e$  is closed then v1 is opened, thus expanding the argon gas into the total volume  $V_{tot}$ .
- 7) Ten values of pressure were recorded in sequence, each with a 20 second measuring time, and the  $V_{tot}$  was calculated by equation (2.42).

Trial	$P_{before}$ (mbar)	$P_{after}$ (mbar)	$V_{tot}$ (ml)
1	5.2358e-3	3.3066e-4	427.5
2	5.5933e-3	3.5270e-4	428.2
3	5.0811e-3	3.2044e-4	428.1
4	5.4104e-3	3.4147e-4	427.8
5	5.191e-3	3.2360e-4	428.0

Table 2.1 Gas expansion measurements for the total volume of the effusion source.

The average total volume is 427.9 ml with a standard deviation of 0.08 ml. At 95% confidence, i.e. three standard deviations, we have an uncertainty of  $\pm 0.24$  ml or  $\pm 0.06\%$ . Combining this uncertainty with the 0.7% uncertainty in  $V_{ref}$  we have

$$V_{tot} = 427.9 \text{ ml} \pm 0.76\% \text{ or } \pm 3.3 \text{ ml.}$$

The linear expansion coefficient for stainless steel is  $16 \times 10^{-6} \text{ K}^{-1}$ . Estimating the volume expansion coefficient at three times the linear coefficient yields a volume

expansion coefficient of  $48 \times 10^{-6} \text{ K}^{-1}$  or  $0.0048\% \text{ K}^{-1}$ . Thus, the volume expansion will become comparable to the  $0.76\%$  uncertainty of  $V_{\text{tot}}$  only for  $158 \text{ K}$  change in temperature. Therefore, at the current degree of uncertainty, no corrections for the thermal expansion will be necessary for usual room temperature use of the source.

### 2.3.2 The gas flow calibration

According to equations (2.19) and (2.23), determining the time rate of change of the number density as a function of number density calibrates the effusion source. Furthermore, as the following measurements show, the effusion source obeys the simple effusion model of equation (2.24). Thus, we use the linear fit of equation (2.28),

$$\ln(n(t)) = \ln(n_0) - \alpha \cdot t \quad (2.44)$$

to determine the characteristic rate constant  $\alpha$  of the effusion source.

A computer program, called FLUX1\_01 has been written to communicate between the Leybold VM211 spinning rotor gauge and an IBM PC compatible computer. This program records the number density versus time, while reporting the two point estimate of  $\alpha$  from equation (2.27). Figure 2.16 shows the results of an argon flow calibration.

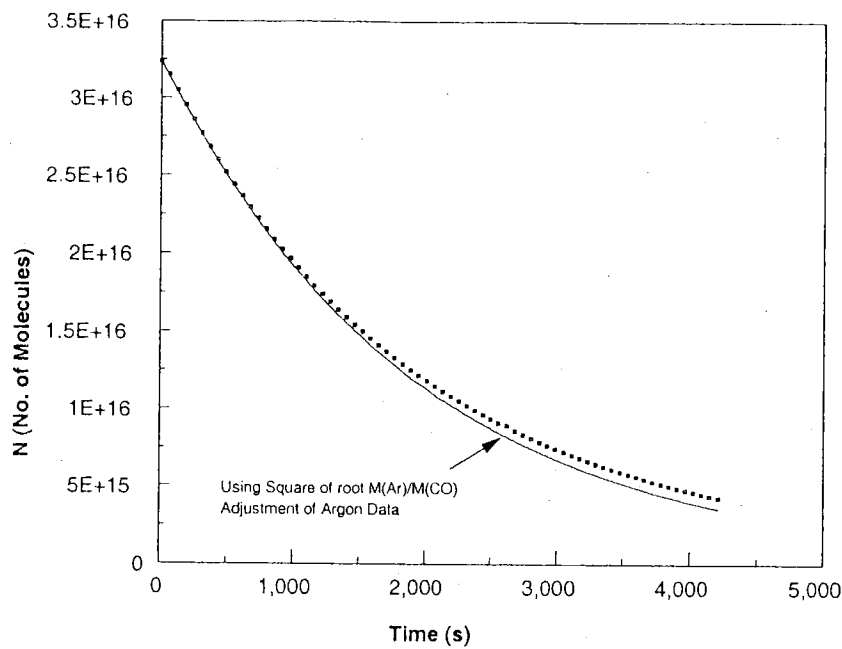


Figure 2.17 Effusion calibration for CO gas compared to the adjusted argon calibration.

Suppose that CO is adsorbed by the walls of the effusion source at the higher initial pressure. Further suppose that as the pressure drops due to effusion, CO desorbs back into the effusion source volume. This desorption would keep the number density higher than expected by the effusion model.

In support of this hypothesis, we have observed that after filling the effusion source with CO, the pressure drops by several percent over about two hours. This drop in pressure implies the uptake of CO within the effusion source, which implies that CO adsorbs to the stainless steel walls. Several attempts were made to quantify this effect, however, it seems – not unexpectedly – that this process is history dependent and our observations have been inconclusive.

Because the error would only be 8% and because we have a plausible and somewhat supported hypothesis, we have chosen to proceed with the assumption that the values of the characteristic rate constant  $\alpha$  calculated from the molecular weight dependence in equation (2.26),  $\alpha_2 = \sqrt{\frac{m_1}{m_2}} \cdot \alpha_1$ , is correct. The characteristic rate constants calculated from the value for argon are shown in Table 2.2.

Gas	$\alpha (10^{-4} \text{ s}^{-1})$
Argon	4.388*
CO	5.245
O <sub>2</sub>	4.906
N <sub>2</sub>	5.245

Table 2.2 The characteristic rate constant for the effusion source for several gases. \* This value was measured for argon and the others were calculated from this value. These values are assigned an uncertainty of  $\pm 3\%$  attributable to the uncertainty in  $\sigma$  for the spinning rotor gauge.

### 2.3.3 The mass spectrometer flow gain

The final step to calibrate the thermal desorption spectrometer is the determination of the relationship between the mass-spectrometer current  $I_{ms}$  and the flow  $\Phi$  into the shroud from the calibrated effusion source assuming negligible losses in the transfer process. Values of  $I_{ms}$  versus  $\Phi$  are measured for each gas and a linear fit is made to determine the slope from which the calibration factor  $g_{flow} = 1/\text{slope}$  is calculated. To expedite this procedure, a computer program has been written to record both  $I_{ms}$  and the number density in the effusion source,  $n$ .

The program uses the entered characteristic rate constant  $\alpha$  and volume of the effusion source to calculate the flow into the shroud. As it starts, it records an entered number of values of mass-spectrometer current before the flow is started, thus establishing an average current baseline, which is subtracted from later current values yielding  $I_{ms}$  due only to the flow. The program then pauses, waiting for the operator to establish the desired number density in the effusion source after which it records values of  $I_{ms}$  and  $\Phi$  until a key is hit. Next the program updates and reports a linear regression of  $I_{ms}$  versus  $\Phi$  followed by asking the operator to establish another value of number density.

Figure 2.18 shows the flow calibration for Ar, CO, O<sub>2</sub>, and N<sub>2</sub> gases, all of which display extremely good linearity over two and a half orders of magnitude.

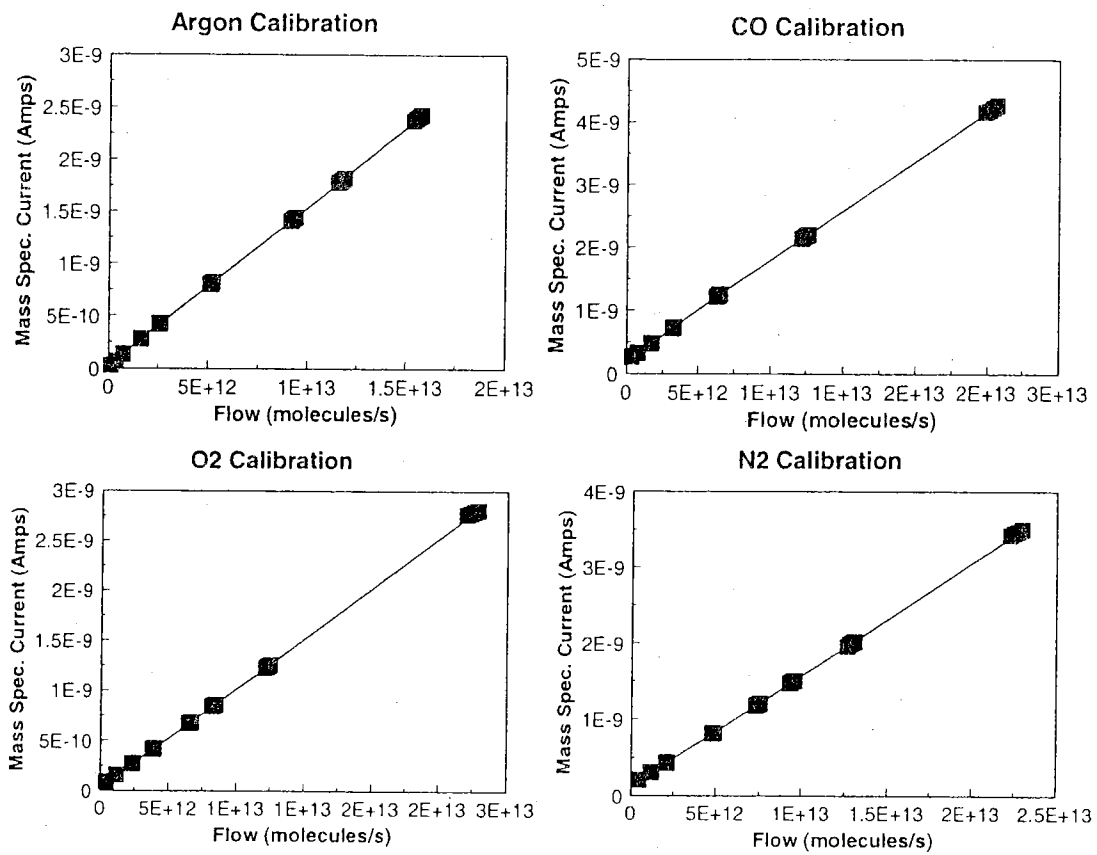


Figure 2.18 Mass-spectrometer flow calibration for Ar, CO, O<sub>2</sub>, and N<sub>2</sub> gas.

The final piece of information needed to calibrate the CTDS is the "effective area" of the sample, for which we attribute the flow of molecules entering the cone. Clearly, the effective area will equal the area of the cone aperture when the sample is close to the aperture. Figure 2.19 shows the results of integrating the cos<sup>n</sup> desorption direction distributions over the entire sample for the whole aperture area. These integrations follow Winkler and Yates[12].

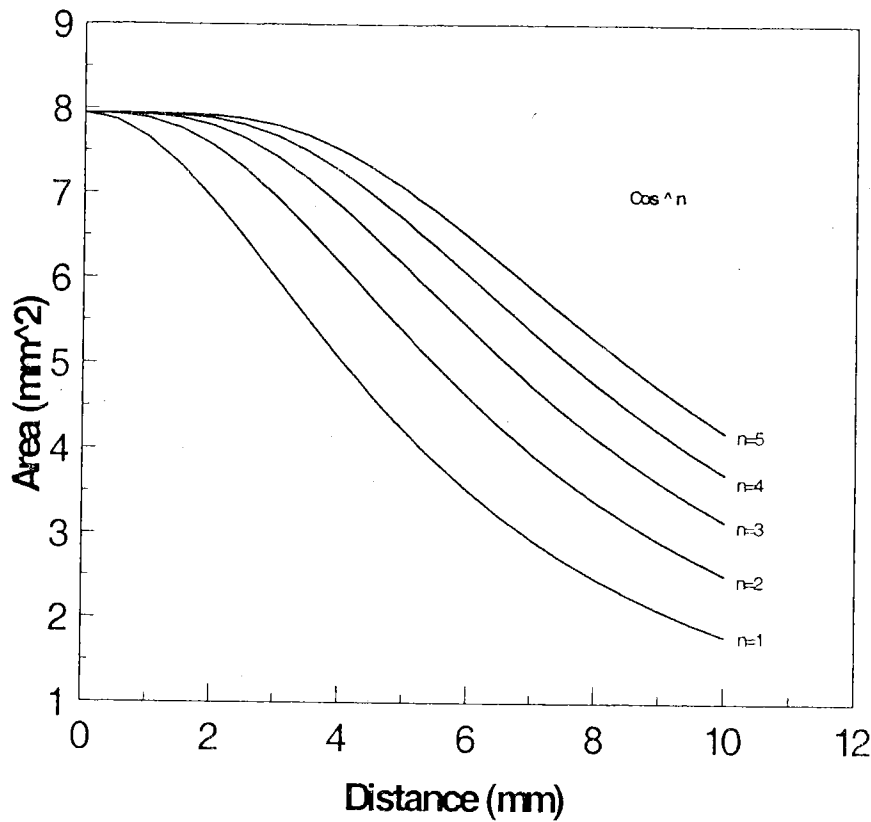


Figure 2.19 The effective area for molecules desorbing into the aperture.

Figure 2.19 clearly shows that, if  $d < 1$  mm, then the effective area is not significantly different from the area of the aperture. The aperture area used in the calculations is  $7.49\text{ mm}^2$ ; however, the cone was later modified and now has an aperture area of  $9.51\text{ mm}^2$ . The desorption rate is then calculated by dividing the flow into the cone by the effective aperture, which for sample distances  $d < 1$  mm is just the cone aperture area.

### 2.3.4 A test study of Pd(110) with O<sub>2</sub>

Finally, we show the initial results of oxygen CTDS on a Pd(110) surface. This system has several advantages; it is relatively easy to prepare [7,25] and it has been studied

by nuclear reaction analysis (NRA)[9,26-28]. Figure 2.20 shows the results of the CTDS of O<sub>2</sub> adsorbed at 100K.

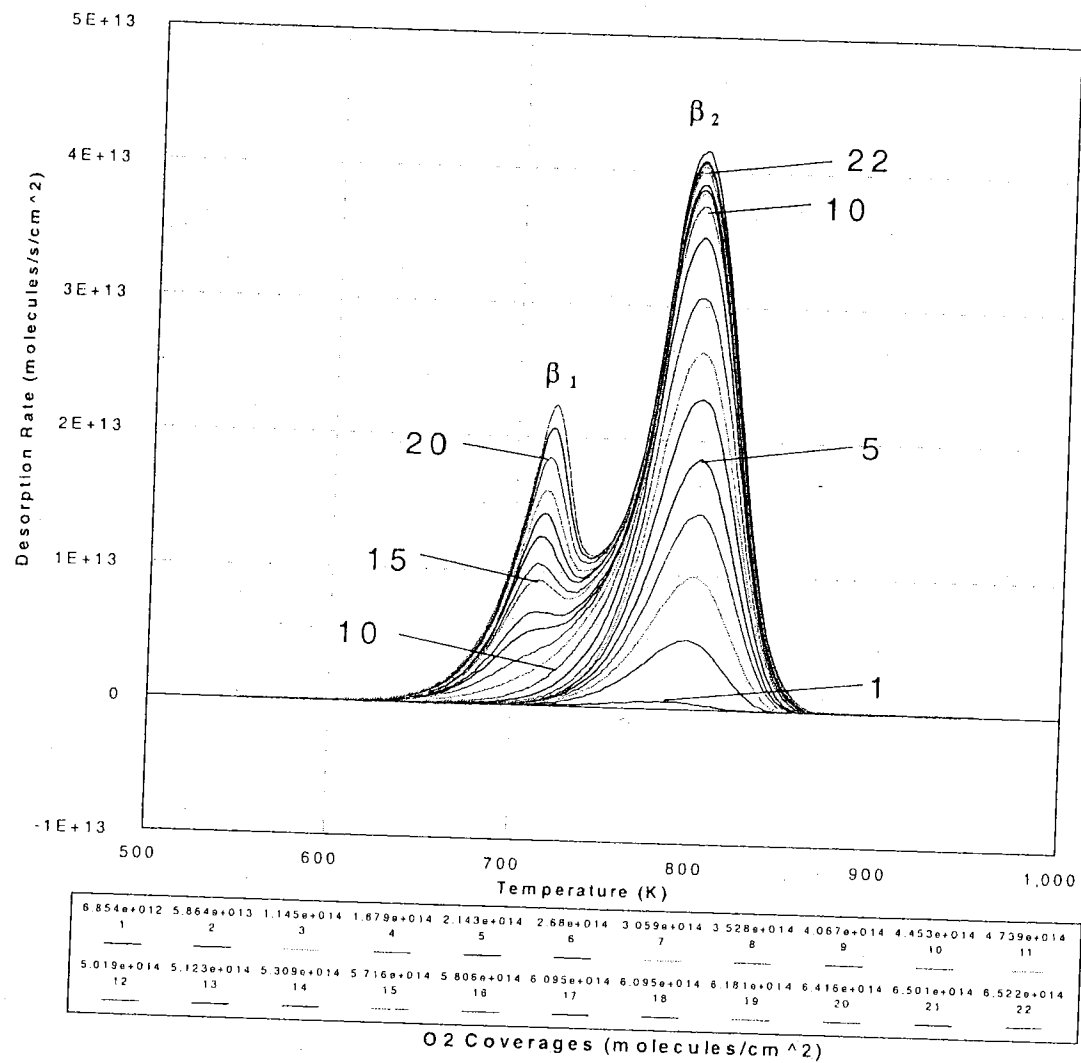


Figure 2.20 CTPD of oxygen on Pd(110) with coverages calculated integrating the desorption rate.

These CTDS traces show one peak ( $\beta_2$ ) for lower coverages, saturating at about  $4.7 \times 10^{14}$  O<sub>2</sub> molecules per cm<sup>2</sup>, which yields  $9.4 \times 10^{14}$  O atoms per cm<sup>2</sup> or  $\theta_{\beta_2} = 1.00$ . NRA gives

precise measurements of the atomic oxygen saturation coverage  $\theta_{\beta 2} = 0.5$  ML in the  $\beta 2$  c(2x4) structure at which the work function is maximized. One monolayer on the Pd(110) surface is  $9.4 \times 10^{14}$  cm<sup>-2</sup>. Comparing these results, one is struck by the exact factor of two, and we immediately started looking for a factor of two error in the calculations, in the measurements, in the programs, or in the references cited.

After a thorough search and numerous individual tests of all factors involved and a review of the references, we concluded that the result is circumstantially an exact factor of two and must come from some inherent misunderstanding of the measurement. We now have several hypotheses. First, it is probable that some gas from the effusion source is adsorbed by the walls of the calibration tube; therefore the flow gain calculated in section 2.3.3 would be artificially high. This error seems unlikely to be a factor of two, since after starting the flow into the shroud the mass-spectrometer current comes to a steady value after a few seconds and then decreases with the rate constant of the effusion source. Second, since the flow from the effusion source enters the shroud differently than the flow from the sample surface, it is possible that the probability of ionization for typical molecules from these two sources will be different. The most obvious explanation of this type of effect is that molecules coming from the sample have a line of sight path coaxial to the ionizer. If a large fraction of the molecules from the sample are ionized on their first pass through the ionizer then the mass-spectrometer current will be higher than expected from an accommodated gas within the shroud. In the masters thesis we did not resolved this issue, however, we suggested that the instrument be modified to have an obstruction placed inside of the shroud in front of the ionizer, thus testing the line of sight issue.

### **3 An Extended Formalism for the Glass Capillary Array Fluxes**

Having reviewed the design criteria and calibration procedures of the differentially pumped mass spectrometer and the effusion source, we now turn to a discussion of the phenomena involved in delivery of gas fluxes by gas dosers. The doser was placed in a position opposing and coaxial to the entrance aperture of the differentially pumped mass spectrometer, which allowed it to be used as an alternative calibration source to the tube leading internally to the mass spectrometer shroud. This position also allowed the spatial flux distribution to be measured and compared with a theoretical description. Knowledge of the spatial distribution is necessary for determining the impingement of gas molecules during dosing, for example in sticking coefficient measurements. While the shape of the distribution will be accounted for at a quantitative level, the magnitude of the flux distribution cannot be determined directly, since the magnitude of loss of the gas along the doser tube and the gain of the spectrometer are not known independently. Estimates of the former process will be examined in Chapter 4.

Glass capillary array (GCA) dosers provide a substantial degree of columniation as compared to typical cosine law effusion sources, thus providing more efficient dosing [12,29-31]. We have examined the spatial distribution from a doser consisting of a long tube terminated in a glass capillary array. The results are of general utility to the practical design of dosers as well as the quantitative aspects of the calibration of the absolute flux in molecules per unit area per unit time.

In section 3.2, we give an extension to the formalism of Winkler and Yates [12] in the form of a reparameterization of the flux calculation, subsequently reducing the number of integrations required. We also apply Fourier transform convolution techniques thus providing an efficient method to calculate the total flux to an arbitrarily shaped target at any position in the target plane. In Section 3.4, we compare the calculated and measured spatial flux distributions produced by the capillary array.

### 3.1 Background

The analysis of a GCA operated in the molecular flow regime [32,33] begins by considering the scattering of molecules from the walls of a single capillary due to an inlet impingement of molecules and the subsequent exit direction distribution. The analysis made by Clausing [33] assumes that the wall scatters the molecules diffusely, i.e. each impinged area element of the tube wall scatters molecules as an effusion source from that surface element. The direction distribution of molecules emitted from a capillary,  $J(\theta)$ , is a highly peaked function of  $\theta$  for small values of  $\gamma = D/L$ , the ratio of the capillary diameter  $D$  to the capillary length  $L$ . The function  $J$  as stated by Olander [32] is,

$$\text{for } \tan(\theta) < \gamma, \quad J(\theta) = \xi \cos \theta + \frac{2}{\pi} \cos \theta \left\{ (1-\xi) R(p) + \frac{2}{3}(1-\xi) \frac{\left[ 1 - (1-p^2)^{\frac{2}{3}} \right]}{p} \right\} \quad (3.1)$$

$$\text{and for } \tan(\theta) \geq \gamma, \quad J(\theta) = \xi \cos(\theta) + \frac{4\gamma}{3\pi} (1-\xi) \frac{\cos^2(\theta)}{\sin(\theta)} \quad (3.2)$$

$$\text{where, } p = \frac{\tan(\theta)}{\gamma}, \xi = \frac{2\gamma}{3}, \text{ and } R(p) = \cos^{-1}(p) - p(1-p^2)^{\frac{1}{2}}. \quad (3.3)$$

Since we require a half space normalized distribution function and since  $J$  is forward normalized, i.e.  $J(\theta = 0) = 1$ , we must re-normalize  $J(\theta)$  by calculating its integral over  $2\pi$  steradians.

$$K_0^{-1} = 2\pi \int_0^{\frac{\pi}{2}} J(\theta) \sin(\theta) d\theta \quad (3.4)$$

This renormalization factor  $K_0$  is a function of the ratio  $\gamma$  and is approximately a straight line on a log-log plot. A linear least squares fit on this plot gives the relationship  $K_0 = 0.277\gamma^{-0.957}$  within 2% for  $\gamma$  from 0.026 to 0.467. For our GCA  $\gamma = 0.02$  and  $K_0 = 12.0245$  by equation (3.4).

To convert the distribution from a single capillary array into the flux density at a point on the target, we begin with the formalism of Winkler and Yates [12] but then, further recognizing the additional azimuthal symmetry of  $J(\theta)$ , we transform into a new polar coordinate system. Figure 3.1 shows the basic geometry of the problem. On the left, a circular source region represents the GCA doser with radius  $R_s$  and shows infinitesimal area  $dA_s = r_s dr_s d\psi_s$  at polar position  $(r_s, \psi_s)$ . On the right, at a distance  $d$  away and parallel to the source is a target plane with an infinitesimal area  $dA_t = r_t dr_t d\psi_t$  at polar position  $(r_t, \psi_t)$ . The distance between  $dA_s$  and  $dA_t$  is specified by  $y$  at an angle  $\theta$  from the doser normal. The total flux from a circular doser to a circular, coaxial target involves integration over the four variables:  $r_s, \psi_s, r_t$  and  $\psi_t$ . As suggested by Winkler and Yates

[12] these integrations may be reduced in dimension by considering the coaxial symmetry of the doser and target, and choosing  $\psi_t = 0$ , which leads to

$$\phi(r_t, d) dA_t = \frac{S \cdot K_0 \cdot dA_t}{\pi \cdot R_s^2} \int_0^{R_s} \int_0^{2\pi} \frac{J(\theta) \cdot d \cdot r_s \cdot d\psi_s \cdot dr_s}{(d^2 + r_s^2 + r_t^2 - 2r_s r_t \cos \psi_s)^{\frac{3}{2}}} \quad (3.5)$$

and

$$\Phi(d) = 2\pi \int_0^{R_s} \phi(r_t, d) r_t dr_t, \quad (3.6)$$

where  $\phi(r_t, d)$ , is the flux density (molecules  $s^{-1}cm^{-2}$ ) at a radial distance  $r_t$  from the center of the target and  $\Phi(d)$  is the total flux (molecules  $s^{-1}$ ) intercepted by a circular target at a distance on the doser axis.

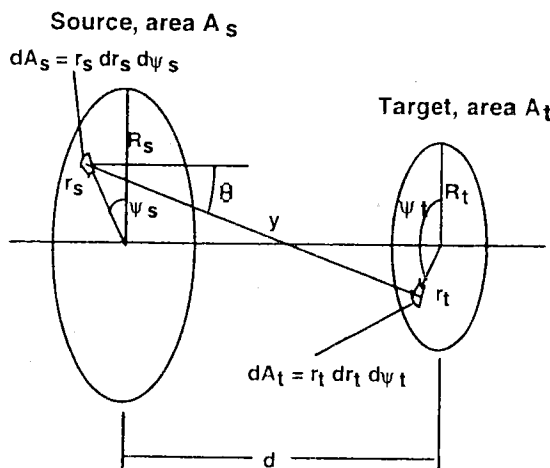


Figure 3.1 The coordinates for the doser and target integrations following Winkler and Yates[12].

### 3.2 The reparameterization

Integrating along a path on the surface of the doser that has constant  $J(\theta)$  for a particular target element would reduce the number of times that the complicated function  $J(\theta)$  needs to be evaluated, thus increasing the speed of integration. This increase motivates the following reparameterization. Consider the coordinates on the doser face shown in Figure 3.2. For each value of target radius  $r_t$  we show a new polar coordinate system  $(r'_s, \psi'_s)$  centered at a point  $r_s = r_t$ , and  $\psi_s = \psi_t = 0$  in the original coordinate system, i.e. the point on the doser that is adjacent to the area element  $dA_t(r_t)$ .

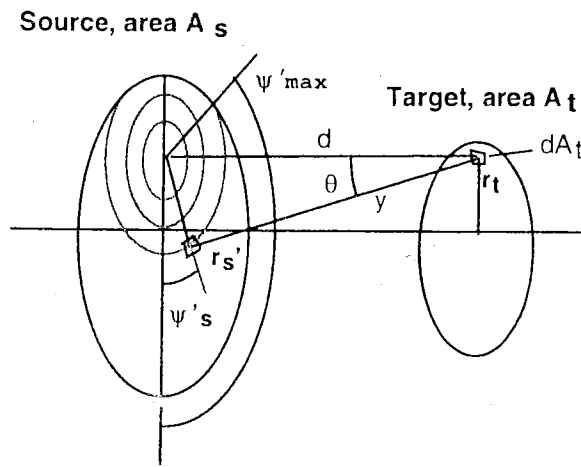


Figure 3.2 The reparameterized coordinates on the doser for each target position  $r_t$ .

The function  $J(\theta)$  is constant along the circles of constant  $r'_s$  and thus satisfies our requirement for the reparameterization. We must now calculate the limits for the  $\psi'_s$  integration. Referring to Figure 3.2 we see that for  $0 \leq r'_s \leq R_s - r_t$  we have  $-\pi \leq \psi'_s \leq \pi$

but for  $r'_s > R_s - r_t$  we have  $-\psi'_{\max}(r'_s, r_t) \leq \psi'_s \leq \psi'_{\max}(r'_s, r_t)$ . We determine  $\psi'_{\max}(r'_s, r_t)$  from the law of cosines. Thus,

$$\cos(\psi'_{\max}) = \frac{(r'_s)^2 + r_t^2 - R_s^2}{2r'_s r_t} \quad (3.7)$$

Further consideration of the  $(r'_s, \psi'_s)$  coordinates reveals a simple relationship for the angle  $\theta$ , namely,

$$\cos(\theta) = \frac{1}{\sqrt{1 + \left(\frac{r'_s}{d}\right)^2}}. \quad (3.8)$$

The denominator in the integrand of (3.5) may now be expressed in terms of the new variable  $r'_s$  as,

$$\frac{d}{(d^2 + r_s^2 + r_t^2 - 2r_s r_t \cos(\psi'_s))^{\frac{3}{2}}} = \frac{1}{d^2 \left(1 + \left(\frac{r'_s}{d}\right)^2\right)^{\frac{3}{2}}}. \quad (3.9)$$

Noting that  $\tan(\theta) = \frac{r'_s}{d}$  and recalling the definition  $p = \frac{\tan(\theta)}{\gamma}$ , we have

$$p = \frac{r'_s}{\gamma d}. \quad (3.10)$$

Thus the parameter  $p$  is a doubly re-scaled, unit-less version of  $r'_s$ . Since  $p$  is present in the definition of  $J(\theta)$  and since  $\theta$  may be expressed in terms of  $p$  we seek a reparameterization of  $J(\theta)$  in terms of  $p$ .

We derive the new function  $J'(p) = J(\theta)$  using the relations

$$\begin{aligned}\cot(\theta) &= \frac{1}{\gamma p}, \\ \cos(\theta) &= \frac{1}{(1 + (\gamma p)^2)^{\frac{1}{2}}},\end{aligned}\quad (3.11)$$

and find the new expression of  $J$ ,

$$J'(p) = \frac{1}{(1 + (\gamma p)^2)^{\frac{1}{2}}} \left[ \xi + \frac{2}{\pi} (1 - \xi) \begin{cases} \cos^{-1}(p) + \frac{1}{3p} [2 - (1 - p^2)(2 + p^2)], & p \leq 1 \\ \frac{2}{3p}, & p > 1 \end{cases} \right]. \quad (3.12)$$

Expressions containing combinations of  $r'$  with other spatial variables and constants become awkward after the  $p$  reparameterization. Therefore, we similarly transform all spatial variables as,

$$q = \frac{r_s}{\gamma d}, \quad s = \frac{R_s}{\gamma d}, \quad \text{and} \quad t = \frac{R_t}{\gamma d} \quad (3.13)$$

The angular limits on  $\psi'_s$  are then given by,

$$\psi'_{\max} = \begin{cases} \pi, & p \leq s - q \\ \cos^{-1} \left( \frac{p^2 + q^2 - s^2}{2pq} \right), & s - q \leq p \leq s + q \\ 0, & p \geq s + q \end{cases} \quad (3.14)$$

We define a new function  $j(p)$  by factoring equation (3.12) to get,

$$J(p) = \frac{1}{(1 + (\gamma p)^2)^{\frac{1}{2}}} j(p) \quad (3.15)$$

The first factor will combine with the denominator in equation (3.9) to eliminate the  $3/2$  power. The flux density of equation (3.5) becomes

$$\phi'(q, d) = \frac{2SK_0}{\pi s^2 d^2} \int_{p_{low}(s, q)}^{s+q} \frac{\psi'_{\max}(p, q) j(p) pdp}{(1 + (\gamma p)^2)^2} \quad (3.16)$$

where  $\phi(r_i, d) = \phi'(q, d) = \phi'\left(\frac{r_i}{\gamma d}, d\right)$  and

$$p_{low}(s, q) = \begin{cases} 0, & q \leq s \\ |q - s|, & q > s \end{cases} \quad (3.17)$$

Equation (3.16) provides an efficient expression for the calculation of the azimuthally symmetric flux density from a circular glass capillary array doser at a point in a plane at a distance  $d$  from the doser and at a radial distance  $r_i$  from the axis of the doser. The total flux to a circular target of radius  $R_i$  centered on the doser axis can be calculated directly as

$$\Phi(d) = 2\pi(\gamma d)^2 \int_0^r \phi'(q, d) q dq \quad (3.18)$$

In this section we have reduced the order of integration from 3 to 2 for the calculation of the total flux to a circular on-axis target.

### 3.3 Arbitrarily shaped planar targets at any position

The methods of the last section allowed us to calculate the total flux to a circular target coaxial with the doser. This could be extended to off axis targets by calculating the flux density in the plane of the target, and then integrating over the repositioned target area. This integration is straightforward and may be easily carried out; however, using two-dimensional Fourier transforms and the convolution theorem, we may calculate the total

flux to a target for a range of positions in the plane. We utilize this method in section 3.5, where the measured flux intercepted by the entrance aperture of the differentially pumped mass spectrometer is compared to the calculated flux versus lateral position from the doser axis. Furthermore, we can utilize the enormous calculation efficiency of Fast Fourier Transform algorithms along with its well-known sampling criteria.

Consider a planar target region  $T$ , whose normal is parallel to the doser axis that we place at an origin on the doser axis at a distance  $d$  from the doser. We define the target selector function  $S_T$  to be,

$$S_T(x, y) = \begin{cases} 1, & (x, y) \in T \\ 0, & (x, y) \notin T \end{cases} \quad (3.19)$$

We now write the total flux to the target,  $\Phi$ , when it is displaced from the origin by  $(x_T, y_T)$  as a convolution of the selector function with the flux density as the convolution,

$$\Phi(x_T, y_T) = \int_{-\infty}^{\infty} \int_{-\infty}^{\infty} S_T(x - x_T, y - y_T) \phi(r_i, d) dx dy = S_T * \phi, \quad (3.20)$$

where  $r_i = \sqrt{x^2 + y^2}$ . Letting  $S_F$ ,  $\phi_F$ , and  $\Phi_F$  be the Fourier transforms of  $S_T$ ,  $\phi$ , and  $\Phi$  respectively, and applying the convolution theorem we have,

$$\Phi(x_T, y_T) = \mathcal{F}^{-1} \{ S_F(k_x, k_y) \phi_F(k_x, k_y) \} \quad (3.21)$$

Thus, for a given doser we need only calculate the Fourier transform  $\phi_F$  once for each distance of interest. Application of equation (3.21) for each target shape of interest,

e.g. the mass spectrometer aperture, and various different shaped samples, gives the total flux as a function of target positions ( $x_T$ ,  $y_T$ ) in a single calculation.

### 3.4 The experimental setup for the measurement of the spatial flux distribution

#### 3.4.1 The differentially pumped mass spectrometer specifications

The differentially pumped mass spectrometer as described in Chapter 2, was designed with a shroud and conical nosepiece to provide a flow regime measurement so that the pressure in the ionizer region is *proportional to the entering flow*. The design parameters were optimized to allow an ultimate flow sensitivity to detect a typical first order desorption feature at  $10^{-5}$  coverage with a characteristic pumping time of ~6 ms at the mass spectrometer ionizer. The approximate volume around the ionizer is  $70 \text{ cm}^3$  and the pumping speed is 11 L/s. In the configuration used for these measurements there was a conical obstruction between the 3.63 mm diameter aperture and the ionizer. This obstruction provides the opportunity to study gases that are well accommodated to the shroud walls thus eliminating gas velocity effects.

#### 3.4.2 The Doser

The molecular doser shown in Figure 3.3 includes a long tube and a glass capillary array (GCA) (Galileo C13L05M10), which is 13.5 mm in diameter by 0.5 mm thick with 10  $\mu\text{m}$  diameter capillaries. Microscopic examination of the GCA showed hexagonal close packed hexagonally shaped capillaries uniformly covering the array with the wall thickness such that about half of the array area is capillary openings as shown in Figure 3.4. The

GCA was mounted to the tube with ceramic adhesive (Aremco Ceramabond™ 671) as shown schematically in Figure 3.3. Because the inside diameter of the tube is less than the diameter of the array and because the glue seals the array from the outside edge, there is an uncertainty in the actual diameter of the array conducting gas from the tube, the effects of which are examined in the next section. The doser is mounted in a xyz manipulator (micrometers have  $\pm 0.001$ in minor divisions) adjusted to have the z axis coaxial with the mass spectrometer aperture.

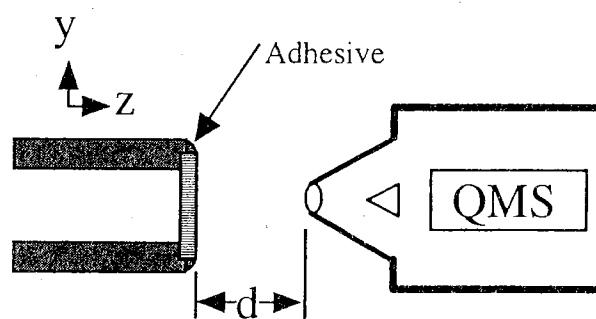


Figure 3.3 The doser tube terminated in a 1.35 cm diameter glass capillary array, which was cemented in place with ceramic adhesive.

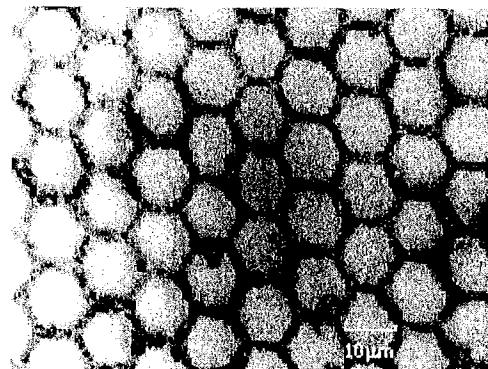


Figure 3.4 A microscope image of the glass capillary array showing its hexagonally close packed hexagonal tubes.

### 3.5 Measurement and analysis of the doser flux

Calibrating the differentially pumped mass spectrometer using the doser and the known total flow from the calibrated gas source requires the exact determination of the fraction of the total doser flow that enters the mass spectrometer aperture. To this end we measure the mass spectrometer current  $i_{ms}(x, y)$  as a function of lateral position of the doser ( $x, y$ ) in front of the aperture as shown in Figure 3.3, while maintaining a constant flow during the measurement. The limits of the lateral motion of the doser are such that the entire non-zero flow function can only be measured for the closest doser to aperture distances. A convenient doser to aperture distance was 0.025 inch (0.635 mm), which is one turn of the micrometer from the zero distance position. The gas flow is maintained manually at  $4.59 \times 10^{12} \pm 0.3\%$  argon atoms per second by throttling the inlet leak valve of the gas source to maintain a nearly constant  $10^{-3} \pm 0.3\%$  mbar Argon pressure in the gas source (with the positive shutoff capillary leak

The mass spectrometer current  $i_{ms}(x, y)$  was measured in a  $30 \times 30$  x-y grid with measurements made at 0.025 inch (0.635 mm) intervals. The position was returned to center after each x scan in order to check for drift in the measurement. This data is shown as a contour plot in Figure 3.5. The plot is generally of circular symmetry with the leftmost area appearing as the most uniformly circular. The central plateau shows more irregularity, appearing highest on the right and drooping about (3%) on the left. The center of symmetry of the doser was found by fitting a circle to a half-height level curve calculated from a 2-D cubic spline of the data, using only data in the left region where the distribution seemed very uniform. For comparison with the theory, we must subtract from the signal the background flux, due to gas that is initially excluded from the mass spectrometer aperture, but then bounces around the chamber and subsequently enters the aperture. Since we measured the doser flux very close to the doser, the background flux was partly obstructed by the doser. Therefore, we determined the background signal as a function of distance from the center of the doser as follows. First, we measured the background signal with the aperture positioned to the side of the doser, out of view of the doser flux. We then determined that the background at this position with the argon flow through the doser equaled the background when the same argon flow entered the chamber from a pump-out on the main chamber, whose inlet was not in the line of sight of the aperture. Next we measured the mass spectrometer current due to the background gas entering the aperture versus lateral position of the doser with the argon flow through the side pump-out. Since the background for the argon flow entering by either route was shown to be the same, and since in molecular flow the background and doser fluxes do not interact, we may assume

that the background measured in this way closely approximates the background when we measure the flux.

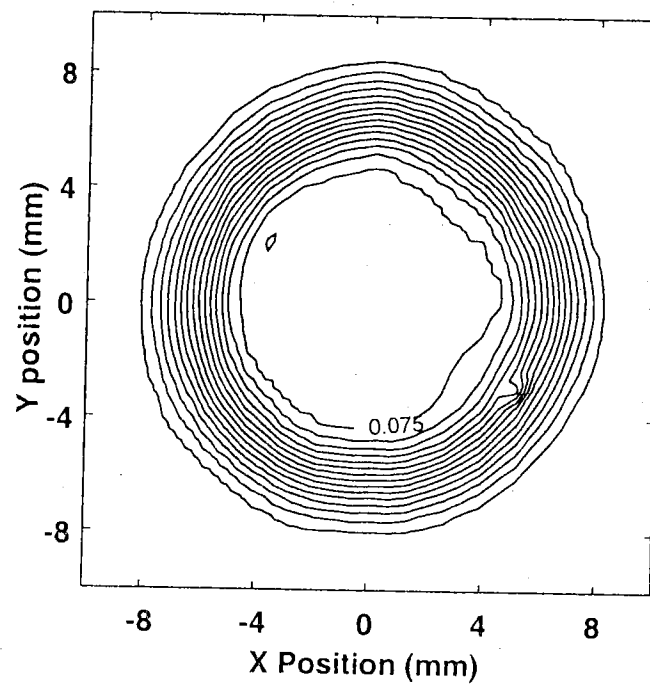


Figure 3.5 The fraction of the total doser flow intercepted by the aperture for argon gas versus lateral position in front of the glass capillary array doser, at 0.005 contour intervals starting at zero on the outside and increasing.

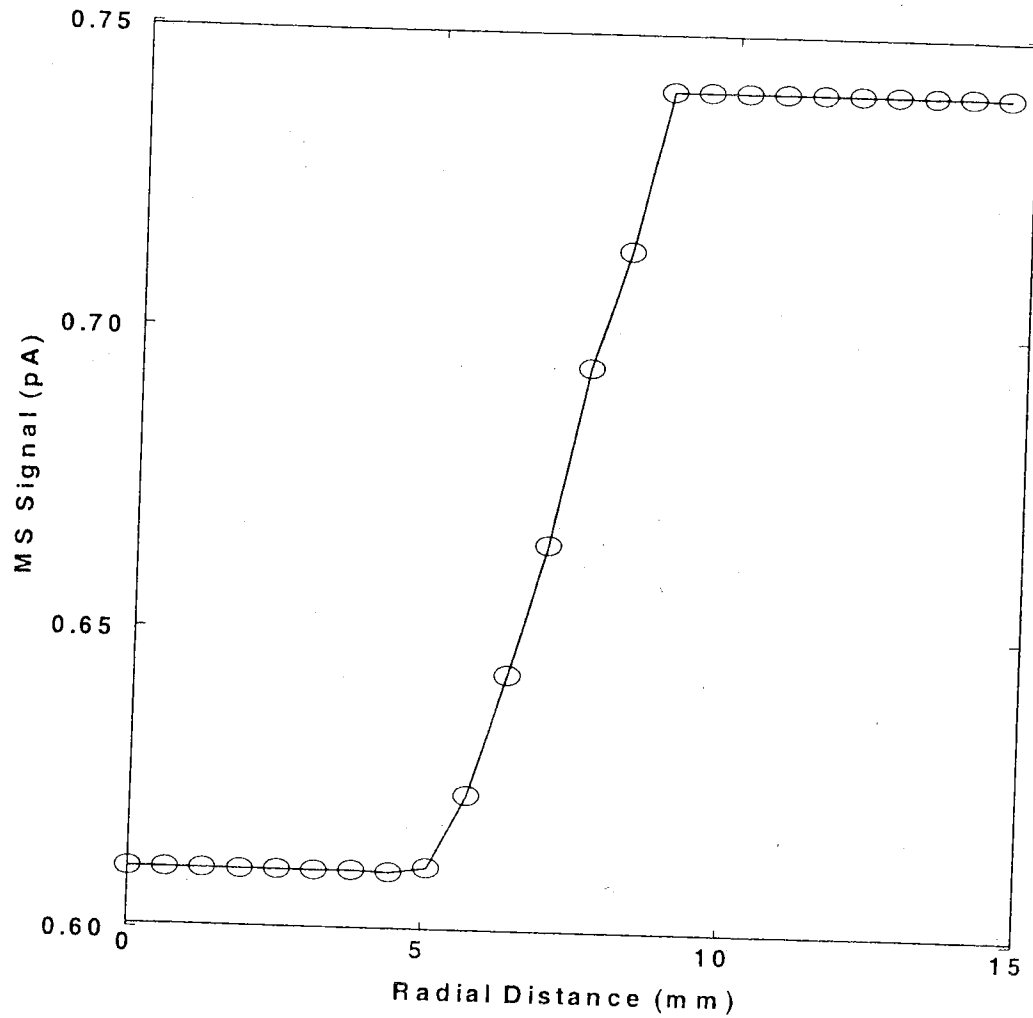


Figure 3.6 The background mass spectrometer signal versus distance to the doser axis at 0.063 cm in front of the doser for argon gas entering the chamber through a side pump-out port.

Figure 3.6 shows the background current,  $i_{back}(r)$ , as a function of radial distance from the center of the measured flux distribution. The signal, relative to the peak current of  $i_{ms}(x, y)$  on the plateau of Figure 3.5 shows, an increase from 6.8% at the center of the doser to 8.1% at the side. We created a 1-D cubic spline of this function in order to

interpolate and subtract the background current,  $i_{back}(r)$ , from flux measurement data,  $i_{ms}(x, y)$ .

We determined the connection between the mass spectrometer current and the total flow from the doser as follows. We assumed that the flow into the mass spectrometer,  $\Phi_{app}$ , is proportional to the measured current, i.e.  $\Phi_{app}(x, y) = \lambda \cdot i_{ms}(x, y)$ , [10]. Since  $\Phi_{app}$  is the convolution of the flux density from the doser with the selector function of the aperture, and since the total flow  $\Phi_{doser}$  from the doser is the area integral of the flux density  $\phi(x, y)$ , consideration of the area integral of  $\Phi_{app}(x, y)$  and the Fourier convolution theorem reveals the relationship

$$\lambda \iint i_{ms}(x, y) dx dy = A_{aperture} \iint \phi(x, y) dx dy = A_{aperture} \Phi_{doser}. \quad (3.22)$$

The flow  $\Phi_{app}$  is then given by

$$\Phi_{app}(x, y) = \Phi_{doser} A_{aperture} \frac{i_{ms}(x, y)}{\iint i_{ms}(x, y) dx dy}. \quad (3.23)$$

If we use Argon in this distribution measurement, then the flow to the aperture for another gas is given by

$$\Phi_{app}^{gas}(x, y) = \Phi_{doser}^{gas} A_{aperture} \frac{i_{Argon}(x, y)}{\iint i_{Argon}(x, y) dx dy} \quad (3.24)$$

We therefore have the required relationship for the calibration flow to the mass spectrometer aperture in terms of the measured spatially dependent current function for

Argon gas and the total flow of gas  $\Phi_{doser}^{gas}$  from the flow source. In order to determine the actual flux density from the doser we would have to deconvolve the effect of the aperture from the flux function  $\Phi_{app}(x, y)$  determined by  $i_{ms}(x, y)$  and equation (3.23). Given the numerical difficulties of deconvolution, we chose to fit the calculated flux into the aperture to the measured flux. Because the GCA diameter is uncertain (see section 3.4.2) the doser array diameter was used as the only free parameter, first using the approximate re-scaling relationship

$$\Phi_2(r) = \frac{D_1^2}{D_2^2} \Phi_1\left(\frac{D_2}{D_1} r\right) \quad (3.25)$$

where we fit on the ratio  $\frac{D_1}{D_2}$  to find an improved value of the actual doser diameter. We then recalculated the flux for the improved estimate and repeated the fit, and so on, to a ratio near unity. Finally, the fit value was used to calculate the flux density by the methods of section 3.3.

We derived the re-scaling relationship (3.25) as follows. First, the flux density is inversely proportional to the area of the doser. Therefore, we re-scale the doser function for  $D_1$  by the ratio of the areas. Second, we assume that corresponding points on the flux function, e.g. the half-height points, have corresponding re-scaled value of position, therefore the radial position is re-scaled by the ratio of the diameters.

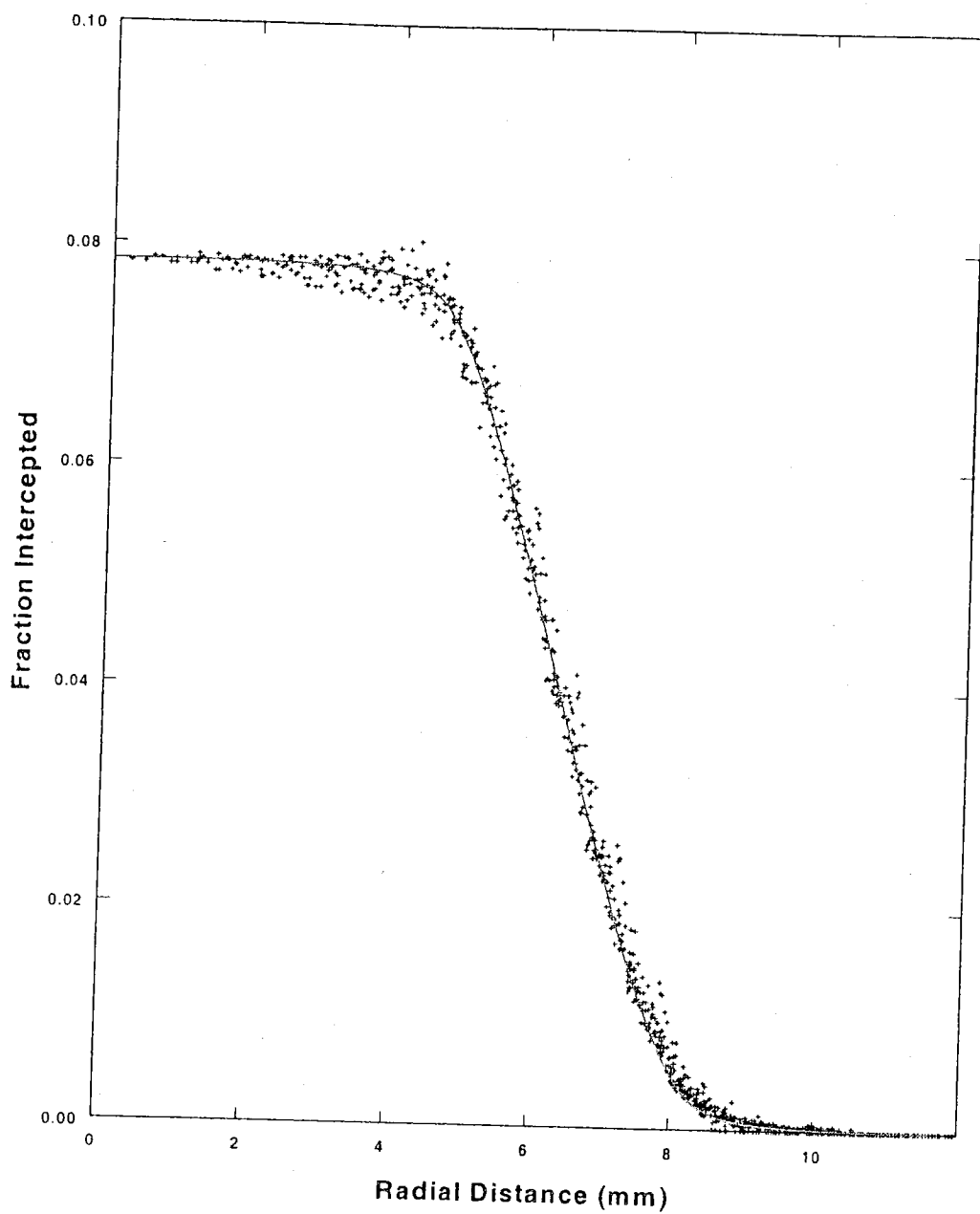


Figure 3.7 The measured fraction of the doser flux to the aperture at a distance of 0.0635 cm in front of the doser (points) and the calculated fraction for a usable doser diameter of 1.29 cm.

Figure 3.7 shows the flux data with the background subtracted as a fraction of the total doser flux versus radial distance from the center using the calibration equation(3.23). This figure also shows the calculated fraction and its corresponding flux density using the formalism of section 3.3 with the total doser flow set to 1 molecule/s in equation (3.16). The second iteration using equation (3.25) produced a ratio of 0.998 of the value from the first iteration, which yielded a fit doser diameter of 1.29cm.

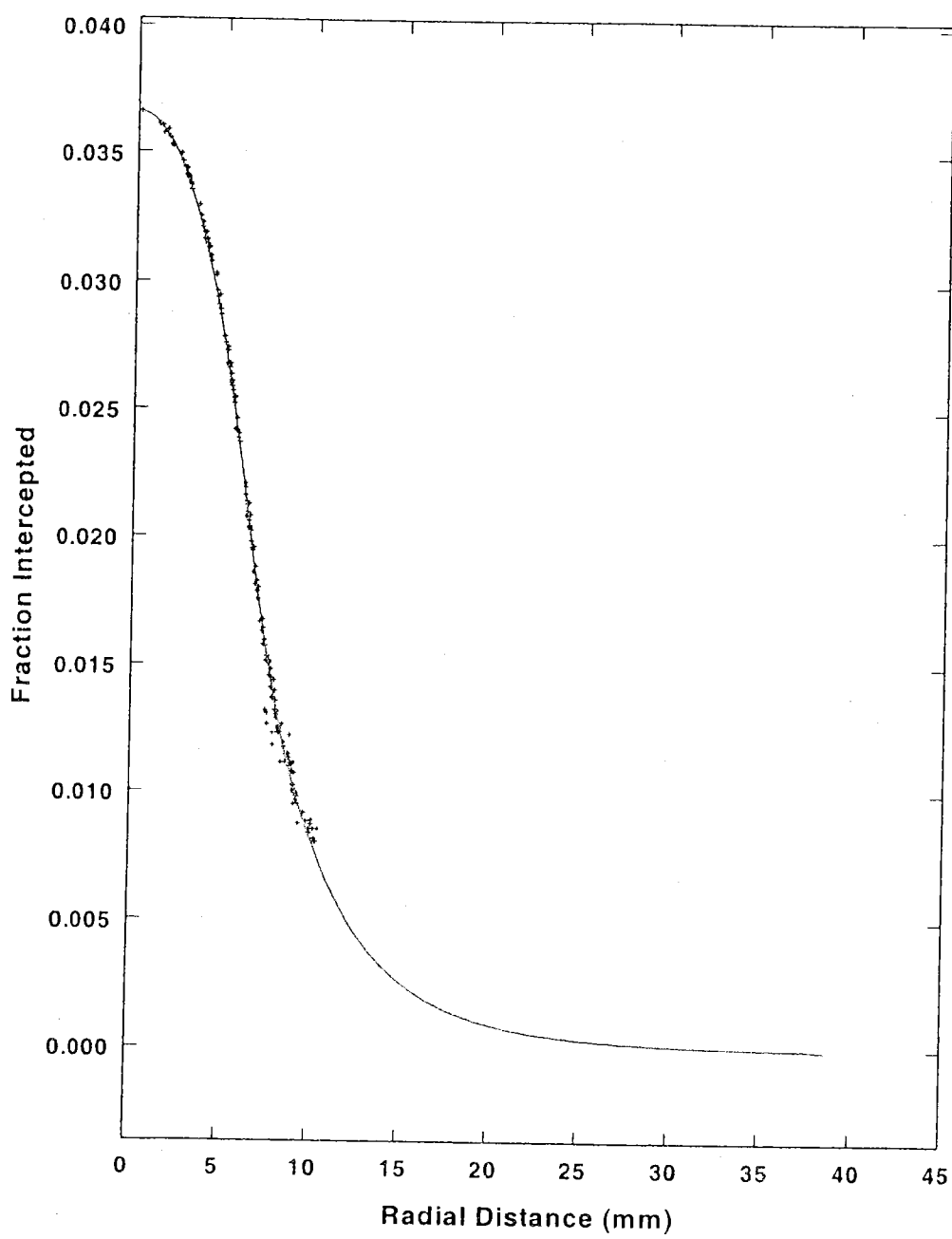


Figure 3.8 The measured fraction of doser flux through the 0.0635cm aperture at a distance of 1.00cm in front of the doser (points) and the calculated fraction for a 1.29cm usable doser diameter (line). The fit allows *only one parameter*, the constant background level, to be varied.

Figure 3.8 shows the flux data versus radial distance at distance of 1.00cm from the doser. The data is fit with equation (3.23), varying only the background value, such that the calculated flux fits the measured flux signal when the peak values are normalized. The background was found to be 6.6% of the peak flux data value and the calculated fraction of total doser flow is 0.037.

Finally, Figure 3.9 shows the average aperture flux functions from fits in Figure 3.7 and Figure 3.8 along with their corresponding flux density functions. These plot clearly show the broadening due to the aperture for the close (0.0635cm) plot; however, at 1.00cm the average flux density nearly matches the flux density.

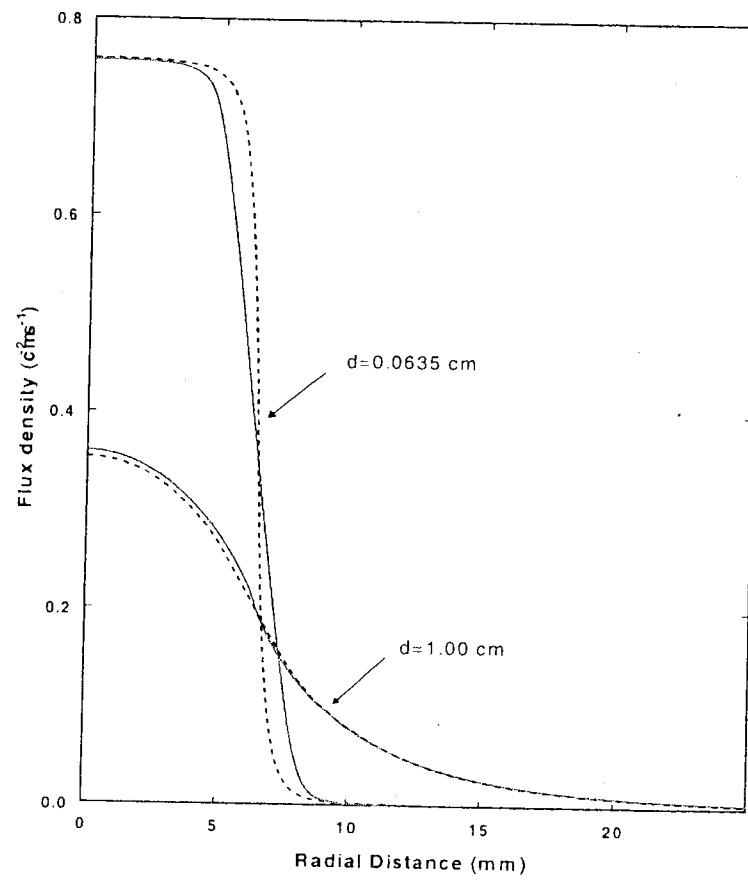


Figure 3.9 A comparison of the average flux density at the aperture (solid curves) with their corresponding calculated flux densities (dashed curves) for a 1.29 cm diameter doser at the indicated distances in front of the doser.

### 3.6 Conclusions

We have compared theoretical and experimental results for the spatial flux density distributions emitted from a glass capillary array doser. We reparameterized the formalism of Winkler and Yates [12] to simplify the spatial flux density calculations, which reduced the order of integration from 2 to 1. Furthermore, we extend the target flux calculation of this formalism to arbitrarily shaped targets in a plane normal to the axis of the doser but not necessarily on the axis of the doser. By measuring the mass spectrometer signal versus lateral x-y position for the entire distribution, we demonstrate a method for the direct measurement of the fraction of the total doser flux intercepted by the entrance aperture of a differentially pumped mass spectrometer. The method also includes the measurement of the position dependent background flux when the aperture is close (0.0635 cm) to the doser. We show that the above measured fraction versus the radial distance to the doser axis is in good agreement when fit with only the usable doser radius as a free parameter. A subsequent measurement at a distance of 1 cm fits exactly using the value of the radius determined above, adjusting only for the background flux. By supplying the doser from a known flux source, such as an effusion source with known cell volume and an accurate spinning rotor gauge, the doser forms the basis for quantitative, absolutely calibrated experiments in mass spectrometry and thermal desorption spectroscopy, as long as loss of the gas along the tube can be neglected. The latter assumption is addressed in the following chapter.

## 4 Transient Molecular Flow in Dosers

### 4.1 Background

In chapter 3, we have demonstrated the use of a glass capillary array doser as a calibrated molecular flux source. This source can be used to absolutely calibrate the signal of a differentially pumped mass spectrometer in terms of the flux to its inlet aperture, as well as for efficiently dosing surfaces with known exposures. The extent to which the source gas sticks to the walls of the doser should be estimated in order to determine the accuracy of the calibration. Since our source utilizes a positive shutoff capillary valve, the inlet transient flow to the doser is a step change. Our differentially pumped mass spectrometer has a characteristic pumping time of approximately 6 ms, which enables us to follow the flow transient at the exit of the doser. Knowing the exit flow versus time for the doser we pose the following question. *Does the transient flow from the doser reveal the type and extent of the sticking in the doser?* To begin to answer this question we present a model for the following three cases. Each case embodies a 1-dimensional diffusion model based on diffuse scattering from the walls of a long narrow tube under molecular flow conditions. In this model most of the flowing gas is assumed to scatter from the walls many times, each time having its direction of travel randomly changed, thus constituting a random walk down the length of the tube. The three cases are a simple long circular tube without sticking, a simple long circular tube with a constant sticking probability, and a long circular tube with a restriction at the exit.

In each case the inlet boundary condition is a step change in flow and the exit boundary condition is considered to be well pumped at a constant pressure that is much smaller than the pressure established in the tube during the flow. For generality in treating both increasing and decreasing flow steps we establish the initial condition by applying a constant inlet flow at time equal to minus infinity. Thus the initial condition is a steady state flow throughout the tube at time equal to zero.

The solutions for a step change in inlet flow from this steady state initial condition constitute the step response functions for each case. These step response functions can subsequently be employed to calculate the response due to any piecewise continuous time varying inlet flow. We can calculate this response by convolving the time derivative of the inlet flow with the step response solution [34].

Comparison of the sticking model to the non-sticking model reveals measurable changes in the shape of the transient. When the doser transient response is measured for a non-sticking gas, e.g. argon, we fit the non-sticking theory to obtain the diffusion constant. We will show that this diffusion constant can be derived from the conductance of the tube and can subsequently be adjusted for the square root mass dependence to obtain the diffusion constant for another gas. A change in the shape of the transient will thus be indicative of sticking and the extent of sticking can be estimated.

The chapter is organized as follows: Section 4.2 presents the transient flow through a long narrow tube in the absence of sticking. In Section 4.3, the model is compared to transient flow data using argon through the doser and the calibration tube. The addition of



sticking to the narrow tube model is presented in section 4.4. Since the glass capillary array represents a restriction at the end of the doser, we solve a transient flow model in section 4.5 to determine whether or not the effects are measurable. Conclusions regarding the information which can be extracted from the transient response will be presented in Section 4.6.

#### 4.2 Simple non-sticking transient flow model

One very simple model for the transient molecular flow in a doser is that of a long narrow tube of length  $L$  and diameter  $d$ , shown in Figure 4.1 with gas molecules scattering diffusely from the walls in a random walk from inlet to exit. The inlet flow is established from a capillary whose conductance is much smaller than the doser tube and whose constant back pressure is much greater than the mean pressure developed in the doser during the flow. With these conditions and the positive shutoff nature of the inlet valve, featuring a small dead volume, we assume a step change to a constant flow at the inlet at time zero. The outlet is well pumped since it exits into a large volume. Therefore, the outlet pressure is assumed to be a constant pressure that is much smaller than the pressures developed in the doser.

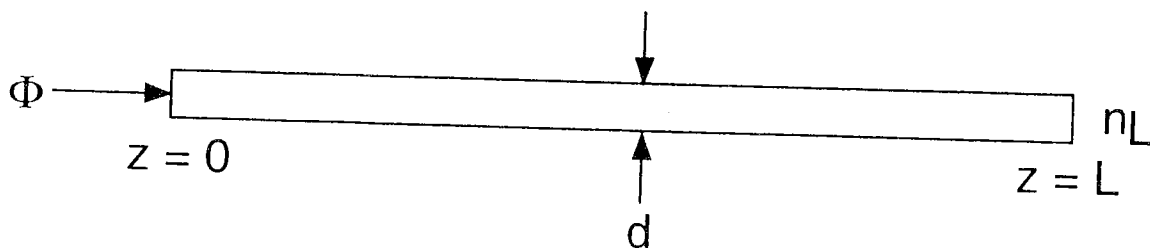


Figure 4.1 The coordinates and boundary conditions for the long narrow tube.

We will calculate the molecular number density  $n(z,t)$  and the molecular flow  $\Phi(z,t)$  for a step change in flow from  $\Phi_0$  to  $\Phi_1$  at the inlet,  $z = 0$  at  $t = 0$ , while the outlet number density is a constant  $n_L$ . Fick's first law relates the number density to the flow by,

$$\Phi(z,t) = -D \frac{\partial n}{\partial z}, \quad (4.1)$$

where  $D$  is the diffusion constant. The initial value boundary value problem for  $n(z,t)$  is given by Fick's second law,

$$\frac{\partial n}{\partial t} = -D \frac{\partial^2 n}{\partial z^2}, \quad (4.2)$$

along with an initial condition and the boundary conditions,

$$\frac{\partial n}{\partial z}(0,t) = -\frac{\Phi_1}{AD} \text{ and } n(L,t) = n_L, \quad (4.3)$$

where  $A$  is the cross-sectional area of the tube.

The steady state solution of (4.2) and (4.3) is,

$$V(z) = n(z, t \rightarrow \infty) = n_L + \frac{\Phi_1}{AD}(L - z) \quad (4.4)$$

Considering the steady state solution we establish the initial condition by applying a constant flow  $\Phi_0$  at  $t \rightarrow -\infty$ . Thus the initial condition is

$$n(z,0) = n_L + \frac{\Phi_0}{AD}(L - z) \quad (4.5)$$

With this initial condition the solution will be the step-response of the system. The general solution is then,

$$n(z,t) = V(z) + \frac{L(\Phi_0 - \Phi_1)}{AD} \lambda \left( \frac{z}{L}, \frac{D}{L^2} t \right), \quad (4.6)$$

and the flux is,

$$J(z,t) = \Phi_1 + (\Phi_0 - \Phi_1) \gamma \left( \frac{z}{L}, \frac{D}{L^2} t \right), \quad (4.7)$$

where

$$\lambda(\xi, \tau) = \frac{8}{\pi^2} \sum_{m=1,3,5,\dots} \frac{1}{m^2} \cos \left( \frac{m\pi}{2} \xi \right) \exp \left( - \left( \frac{m\pi}{2} \right)^2 \tau \right), \quad (4.8)$$

and

$$\gamma(\xi, \tau) = \frac{4}{\pi} \sum_{m=1,3,5,\dots} \frac{1}{m} \sin \left( \frac{m\pi}{2} \xi \right) \exp \left( - \left( \frac{m\pi}{2} \right)^2 \tau \right), \quad (4.9)$$

for

$$\xi \equiv \frac{z}{L} \text{ and } \tau \equiv \frac{D}{L^2} t \quad (4.10)$$

where  $\xi$  is a dimensionless position and  $\tau$  is a scaled dimensionless time.

The base functions of the solutions (4.8) and (4.9) may be tabulated and spline interpolated as any other transcendental function and they are plotted in Figure 4.2 and Figure 4.3 respectively. Note that the solutions (4.6) and (4.7) define either a rising or a falling transient depending on the values of  $\Phi_0$  and  $\Phi_1$ .

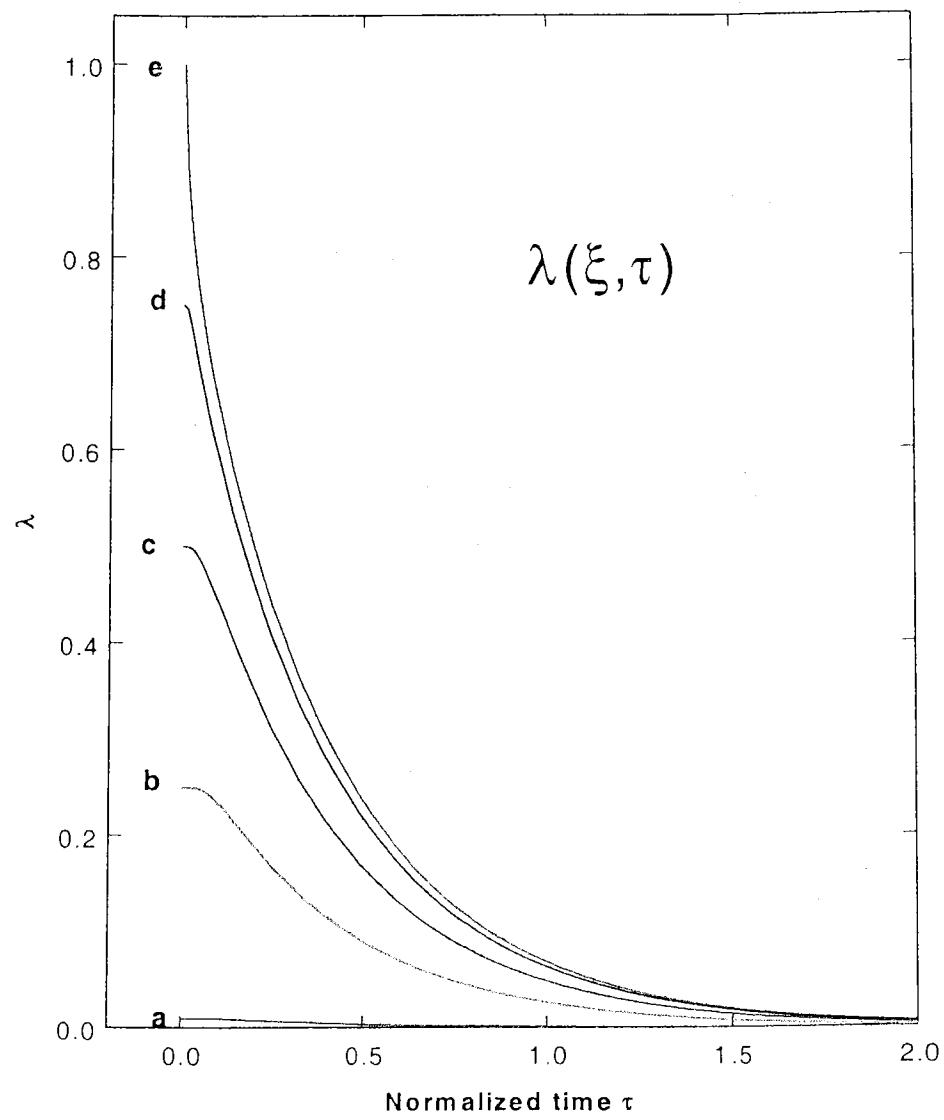


Figure 4.2 The base function  $\lambda(\xi, \tau)$  for the number density transient in a long narrow tube for several values of normalized distance,  $\xi$ , along the tube (a) 0.99, (b) 0.75, (c) 0.50, (d) 0.25, (e) 0.00.

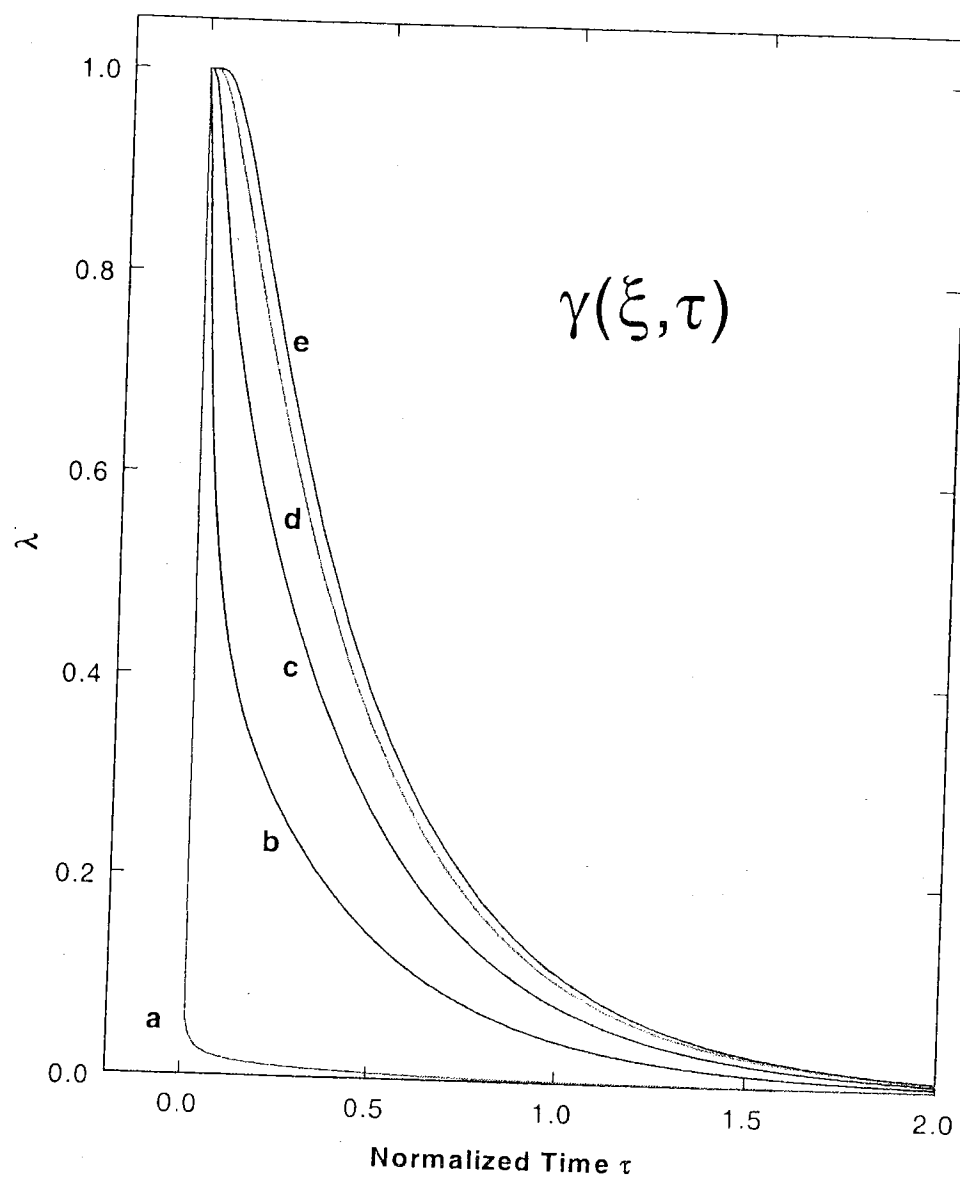


Figure 4.3 The base function  $\gamma(\xi, \tau)$  for the transient flow in a long narrow tube for several values of normalized distance,  $\xi$ , along the tube (a) 0.01, (b) 0.25, (c) 0.50, (d) 0.75, and (e) 1.00.

We determine the diffusion constant  $D$  by comparing the steady state solution to the standard vacuum molecular flow calculation of the throughput  $q$  given by

$$q = C(P_{inlet} - P_{outlet}) = C(n_{inlet} - n_{outlet})k_B T . \quad (4.11)$$

where  $C$  is the conductance,  $P_{inlet}$  and  $P_{outlet}$  are the respective pressures.

The equivalent statement from the steady state solution is obtained through Fick's first law as

$$\Phi = -AD \frac{dn(z, t \rightarrow \infty)}{dz} = \frac{AD}{L} (n_{inlet} - n_{outlet}) \quad (4.12)$$

Since  $q = k_B T \Phi$ , we have  $C = \frac{AD}{L}$ . The conductance for a long narrow tube is given approximately [35] by

$$C = \frac{4}{3} A \frac{d}{L} \sqrt{\frac{RT}{2\pi M}} = \frac{1}{3} A \cdot \frac{d}{L} \cdot \bar{v} \quad (4.13)$$

The diffusion constant  $D$  is then a function of the diameter  $d$  of the tube, and the average molecular velocity of the gas  $\bar{v}$ .

$$D = \frac{4}{3} d \sqrt{\frac{RT}{2\pi M}} = \frac{1}{3} d \cdot \bar{v} \quad (4.14)$$

Returning to Figure 4.3 curve (e) we see that there is a delay  $\tau \approx 0.1$  for the flow to start at the exit. Defining the delay time as the time for the exit flow to change to 10% of the new steady state value, we solve the equation  $\gamma(L, \tau_{delay}) = 0.90$  finding  $\tau_{delay} = 0.06346$ . Using definition (4.10) and equation (4.14), we find

$$t_{delay} = 0.047595 \frac{L^2}{d} \sqrt{\frac{2\pi M}{RT}} \quad (4.15)$$

Similarly, if we define the rise or fall time as the time for the exit flow to change by 90% we have

$$t_{rise/fall} = 1.47374 \frac{L^2}{d} \sqrt{\frac{2\pi M}{RT}} \quad (4.16)$$

Table 4.1 shows the normalized delay times, rise times, and their ratios for several fractional changes in the flow. The corresponding times can then be calculated by

$$t = 3\tau \frac{L^2}{d \cdot v} \quad (4.17)$$

Because the ratio of the rise time and the delay time is independent of the dimensions and the gas velocity, the ratio can be used to estimate the start time from the corresponding absolute positions of the delay and rise times. Let  $\chi = \frac{\tau_{rise}}{\tau_{delay}}$ , then the start time  $t_0$  is given by

$$t_0 = \frac{\chi \cdot t_d - t_r}{\chi - 1} \quad (4.18)$$

where  $t_d$  and  $t_r$  are absolute delay and rise times respectively.

fraction	$\tau_{delay}$	$\tau_{rise}$	$\frac{\tau_{rise}}{\tau_{delay}}$
0.01	0.063456	1.964308	30.95528
0.05	0.099525	1.312027	13.18295
0.1	0.130159	1.031105	7.921894

Table 4.1 Normalized delay and rise times for non-sticking transient flow.

#### 4.3 Fitting the transient flow of Argon gas

Figure 4.4 and Figure 4.5 show the results of fitting this non-sticking, open tube model to the differentially pumped mass spectrometer current after the positive shutoff valve is opened allowing argon gas to flow through either the doser or the direct tube to the inside of the mass spectrometer shroud respectively. The fits were made in MathCad 2000 using the Marquadt non-linear fitting algorithm in the “minerr” function in a solve block to minimize the square deviation function. As expected from equations (4.15) and (4.16) the transient times for the longer, narrower tube to the shroud, ( $L \approx 2m$  and  $d \approx 3mm$ ) are longer compared to the doser ( $L \approx 0.9m$  and  $d$  is uncertain because there are several diameters ranging from  $12.7mm$  to  $3mm$ ). Considering the doser’s somewhat complex combination of different diameter tubing, a 90 degree bend, and termination of the tube with the glass capillary array, the fit is surprisingly good. Likewise, the fit for the long  $0.625cm$  (0.25in) tube, which includes several formed bellows sections, is also good. The differences appear only at the foot of the transients. For the doser, the fit is much sharper than the data. For the long tube, the fit shape and the slope matches the data, but again has a slight delay before rising more rapidly, fitting the data after about a 20% rise.

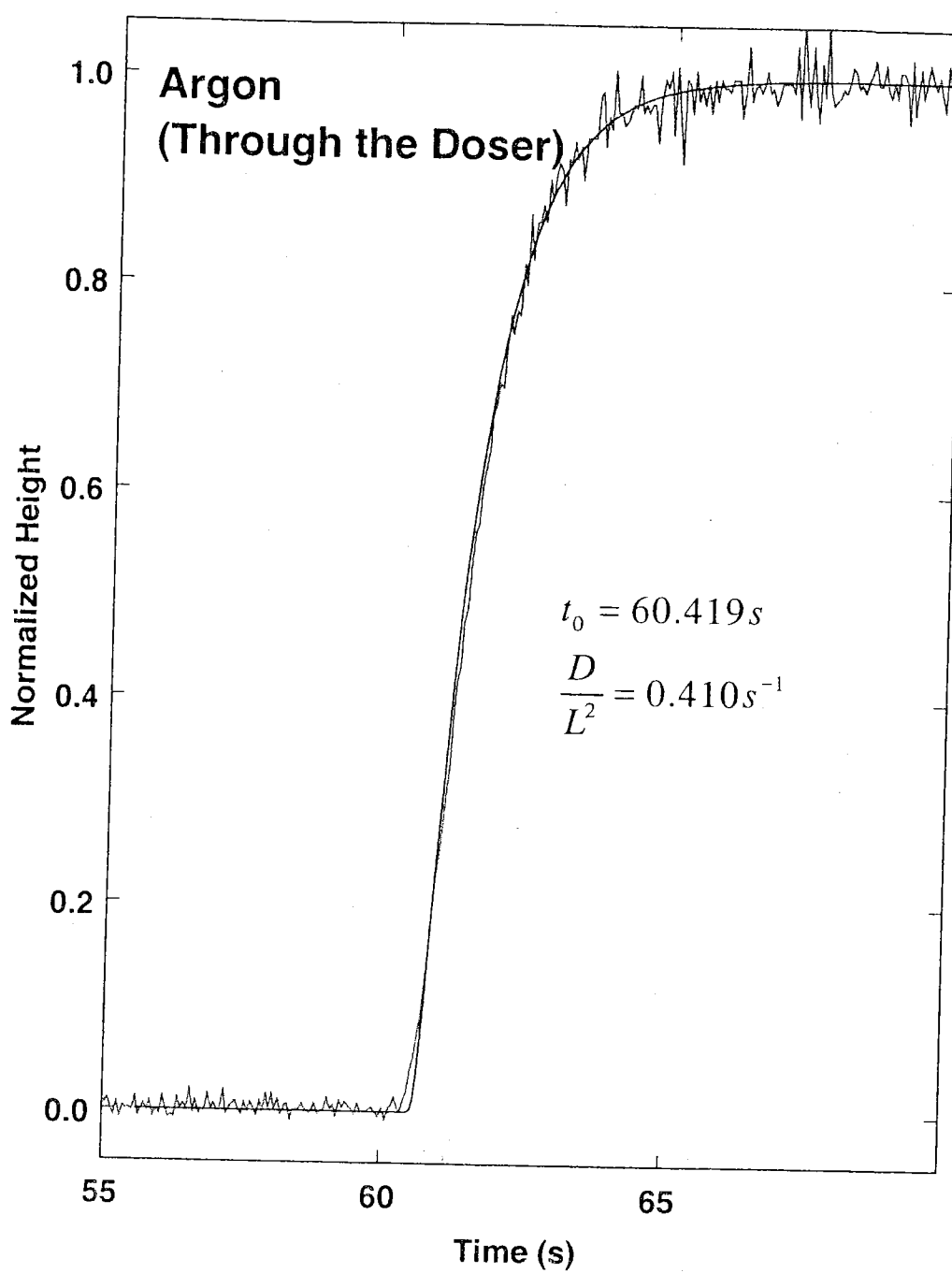


Figure 4.4 Measured argon transient through the doser normalized to the fit value for steady state height.

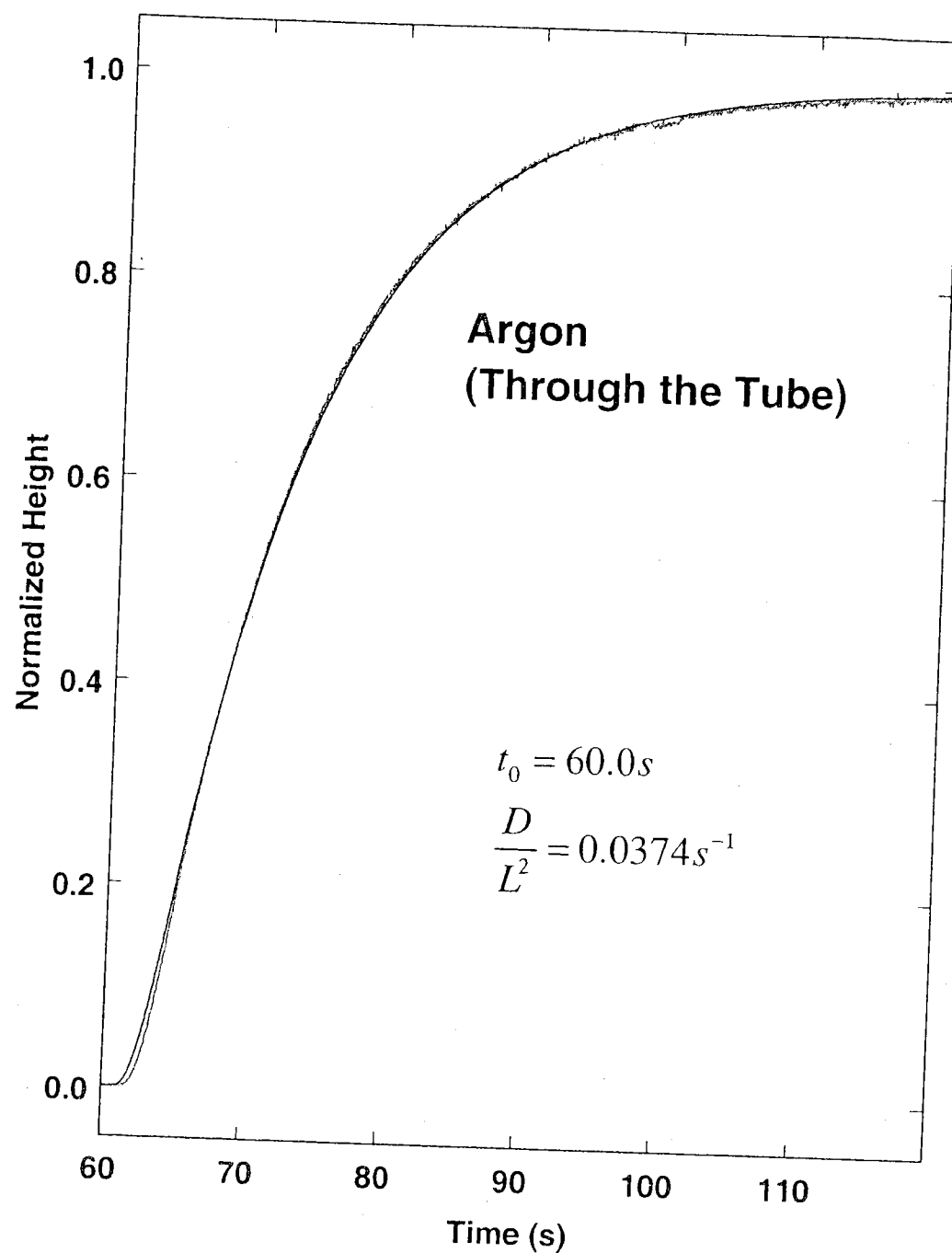


Figure 4.5 Measured argon transient through the tube directly into the mass spectrometer shroud, normalized to the fit value for steady state height.

We conclude that the transient response model agrees well with data for argon, in which sticking is expected to be negligible. Furthermore, the delay and rise/fall times can be used to estimate the starting time as well as the value of  $D/L^2$ . These properties, together with Table 4.1, provide a more convenient means of fitting the data than with an explicit evaluation of the deviation from equation (4.7).

#### 4.4 Transient flow model with a constant sticking coefficient

To include sticking in the transient molecular flow model, we must have a loss term in the partial differential equation. Generally, this loss term could be expressed as a function of position, time, sticking probability, temperature, the tube dimensions and the number density. In practice, the sticking probability will also depend on the impingement history and the desorption rate. Solution of this general problem seems impractical. We choose to start with the simplest sticking model of constant sticking probability,  $S_0$ , hoping to gain some insight into more complicated sticking cases as a consequence. Considering

$S_0$  and the impingement rate  $\sqrt{\frac{RT}{2\pi M}}n$  we arrive at the loss term  $\rho n$  where,

$$\rho = \frac{4S_0}{d} \sqrt{\frac{RT}{2\pi M}} \quad (4.19)$$

The partial differential equation is then

$$\frac{\partial n}{\partial t} = D \frac{\partial^2 n}{\partial x^2} - \rho n, \quad (4.20)$$

with a steady state solution

$$V(z) = n(z, t \rightarrow \infty) = \frac{\Phi_1}{\lambda AD} e^{-\lambda z} + \left( n_L - \frac{\Phi_1}{\lambda AD} e^{-\lambda L} \right) \frac{\cosh(\lambda z)}{\cosh(\lambda L)} \quad (4.21)$$

where

$$\lambda = \sqrt{\frac{\rho}{D}} = \frac{\sqrt{3S_0}}{d}. \quad (4.22)$$

We have again imposed an initial condition with a flow  $\Phi_0$  started at  $t = -\infty$ . The general solution is then

$$n(z, t) = V(z) + \frac{L(\Phi_0 - \Phi_1)}{AD} e^{-\rho t} \frac{8}{\pi^2} \sum_{m=1,3,5,\dots} \frac{1}{m^2 + \left(\frac{2\lambda L}{\pi}\right)^2} \cos\left(\frac{m\pi z}{2L}\right) \exp\left(-D\left(\frac{m\pi}{2L}\right)^2 t\right). \quad (4.23)$$

The resulting flow is

$$\begin{aligned} \Phi(z, t) = & \Phi_1 e^{-\lambda z} - (\lambda D A n_L - \Phi_1 e^{-\lambda L}) \frac{\sinh(\lambda z)}{\cosh(\lambda L)} \\ & + (\Phi_0 - \Phi_1) e^{-\rho t} \frac{4}{\pi} \sum_{m=1,3,5,\dots} \frac{m}{m^2 + \left(\frac{2\lambda L}{\pi}\right)^2} \sin\left(\frac{m\pi z}{2L}\right) \exp\left(-D\left(\frac{m\pi}{2L}\right)^2 t\right) \end{aligned} \quad (4.24)$$

The transient parts of these solutions are similar to the non-sticking solution. They have the same eigenvalues and eigenfunctions but the coefficients are now functions of

$\lambda L = \frac{L}{d} \sqrt{3S_0}$ . As  $m \rightarrow \infty$  the coefficients converge uniformly to the non-sticking

coefficients. The temporal functions have an additional factor of  $e^{-\rho t}$ . These solutions are easily shown to revert identically to the non-sticking solution when the sticking probability is zero.

Now consider the flow at the outlet for  $n_L = 0$ . The solution for the steady state flow then becomes

$$\Phi_{outlet}(\lambda L) = \Phi_1 e^{-\lambda L} (1 + \tanh(\lambda L)) \quad (4.25)$$

Figure 4.6 shows a plot of  $\Phi_{outlet}(x)$  and  $1 - \Phi_{outlet}(x)$  with  $\Phi_1 = 1$  and  $x = \lambda L = \frac{L}{d} \sqrt{3S_0}$ .

The half height value of  $\Phi_{outlet}$  is  $x_{1/2} = 1.31696$ . The sticking probability, for which half of the gas flowing through the tube exits, is then given by

$$S_{1/2} = \frac{x_{1/2}}{3} \left( \frac{d}{L} \right)^2 \quad (4.26)$$

and similarly for x values of other exit fractions.

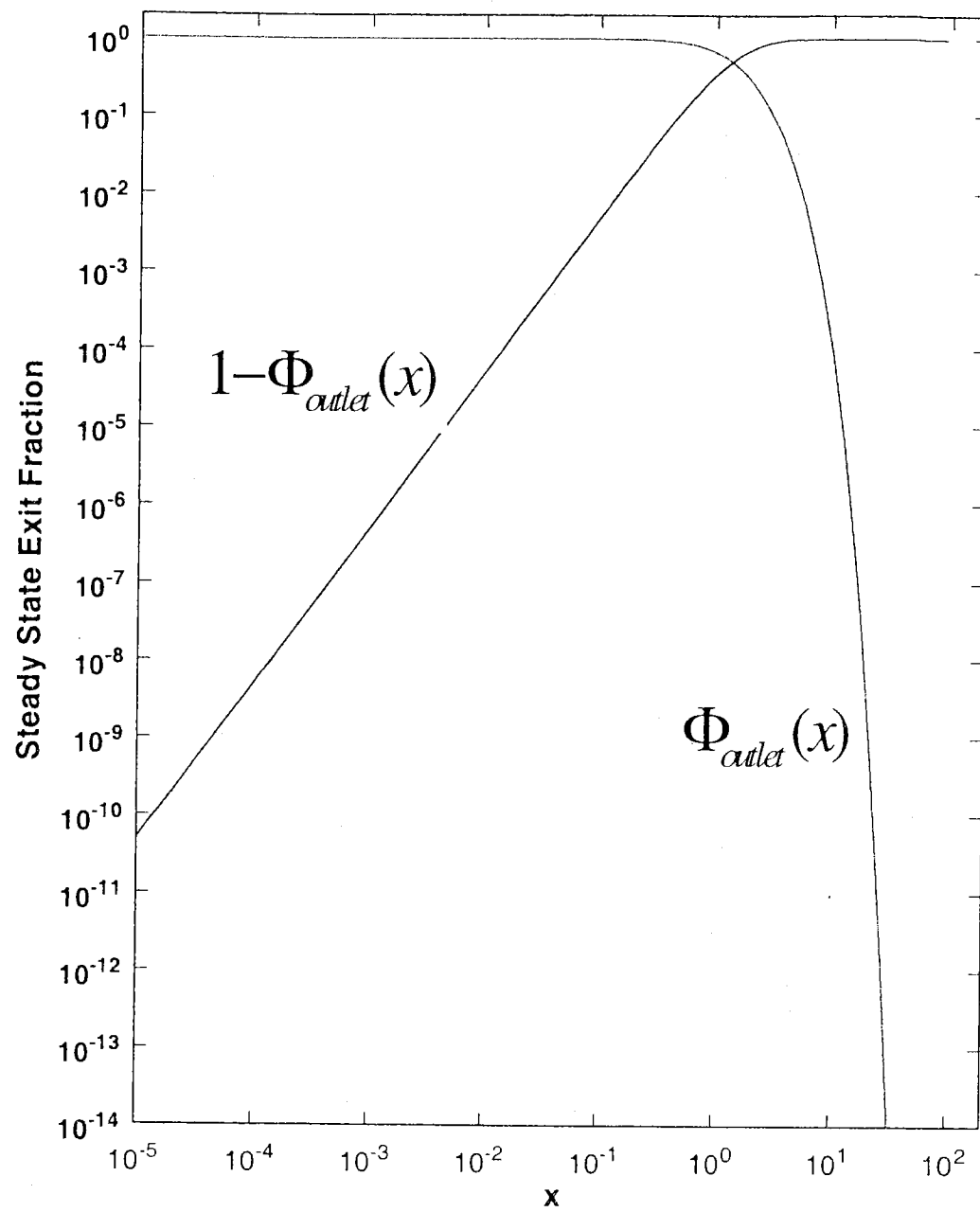


Figure 4.6 The steady state exit fraction versus  $x = \lambda L = \frac{L}{d} \sqrt{3S_0}$  for a long narrow tube with constant sticking coefficient  $S_0$ .

The presentation of the delay and rise/fall times is more complicated. The transient part of  $\Phi(z,t)$  now depends on the ratio  $L/d$  in the coefficients of the summation and further depends on the quantity  $\rho$  a function of  $S_0, d, T$ , and  $M$  defined in equation (4.19). These times must be calculated for specific parameters using a root-finding algorithm to solve the equation  $\Phi_{transient}(t) - f = 0$ , where  $\Phi_{transient}(t)$  is the transient part of equation(4.24) with  $n_L = 0, \Phi_0 = 0, \Phi_1 = 1$ , and where  $f$  is the desired fraction, e.g.  $f = 0.99$  for  $t_{delay}$  and  $f = 0.01$  for  $t_{rise/fall}$ .

As an example, we show the results of the transient analysis for the case of a tube diameter  $d = 1$  cm and length  $L = 100$  cm with argon gas at 300K. Figure 4.7 shows the calculated exit fraction versus time for several values of sticking probability in comparison with the non-sticking exit fraction. Both the steady state exit fraction and the transient times decrease as the sticking probability increases. The shape of the transient is more clearly revealed in Figure 4.8 where the same curves are displayed normalized to their steady state value. Unless, the absolute fluxes of the gas entering and leaving the tube can be measured, in practice only the shape of the curve can be used to distinguish the effects of sticking. Thus, comparison of the transient response of a non-sticking gas, e.g. argon, to that of a sticky gas, within this approximation of constant sticking coefficient, will reveal a faster apparent rise time if sticking occurs.

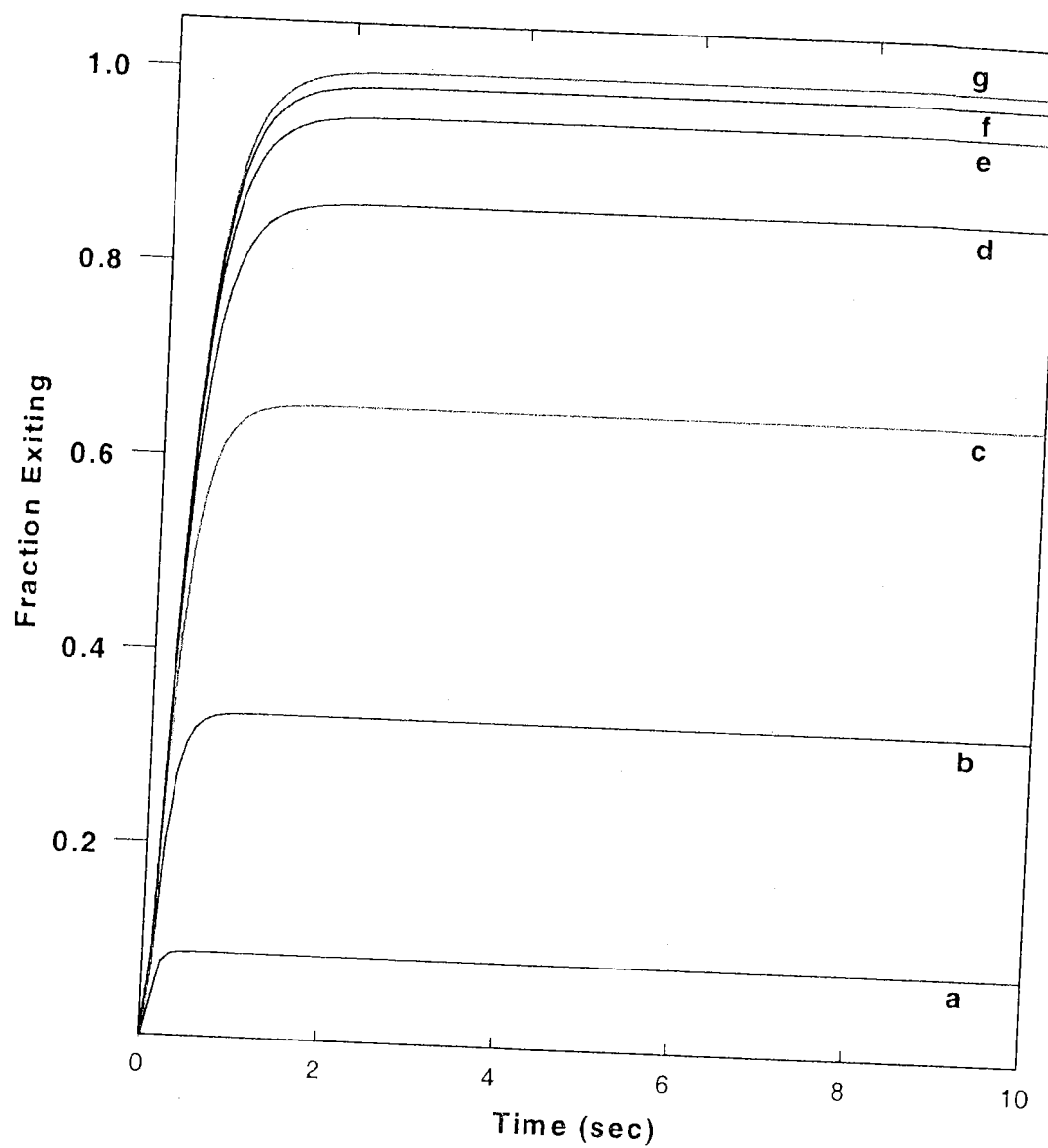


Figure 4.7 The fraction of gas exiting a 1 m long tube of 1 cm diameter for several sticking probabilities (a) $3\times10^{-4}$  ,(b) $1\times10^{-4}$  ,(c) $3\times10^{-5}$  ,(d) $1\times10^{-5}$  , (e) $3\times10^{-6}$  ,and (f) $1\times10^{-6}$  compared to the non-sticking model (g) .

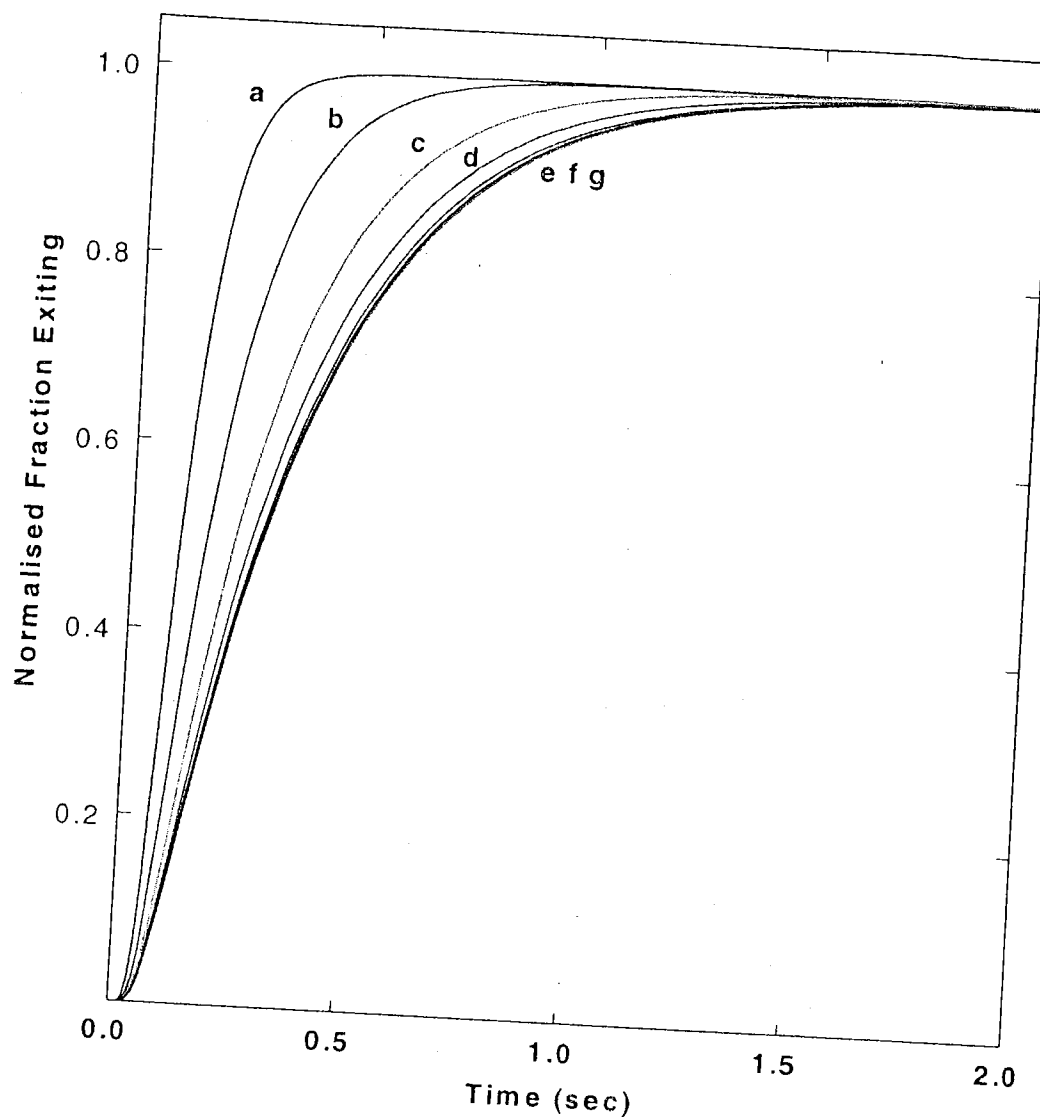


Figure 4.8 The fraction exiting normalized to the steady state value for a 1m long 1cm diameter tube with constant sticking probabilities (a)  $3 \times 10^{-4}$ , (b)  $1 \times 10^{-4}$ , (c)  $3 \times 10^{-5}$ , (d)  $1 \times 10^{-5}$ , (e)  $3 \times 10^{-6}$ , and (f)  $1 \times 10^{-6}$  compared to the non-sticking model (g).

The delay time and the rise/fall time versus sticking probability are shown in Figure 4.9. At sticking probabilities below  $10^{-6}$  the rise/fall time is constant at 0.8s in agreement with the non-sticking value for this particular choice of  $L$  and  $d$ . For sticking probabilities

above  $10^{-4}$ , the rise/fall time is approximately  $t_{rise/fall} = (2.15 \text{ ms}) \cdot S^{-2/3}$ . Note that at  $S = 1$  the rise/fall time is roughly the value of 2.5 ms, which would be required for a molecule of average velocity to traverse the 1 m tube.

We explain the apparent decrease in transient time in Figure 4.8 with the following argument. Consider the number of wall hits,  $N_{hi}$ , that each exiting molecule has made. Due to its random path back and forth down the tube, the transit time for a molecule will certainly increase with the number of hits. Since the probability of a particular molecule sticking in the tube before exiting increases with the number of hits, it follows that as the sticking probability increases, fewer molecules with long transit times will exit the tube and those that do exit will be more likely to have made fewer hits. Thus, the distribution of transit times for the fraction of molecules exiting the tube is shifted lower as the sticking probability increases. Therefore, while at higher sticking probabilities fewer molecules exit the tube, the molecules that do exit have transited the tube in less time.

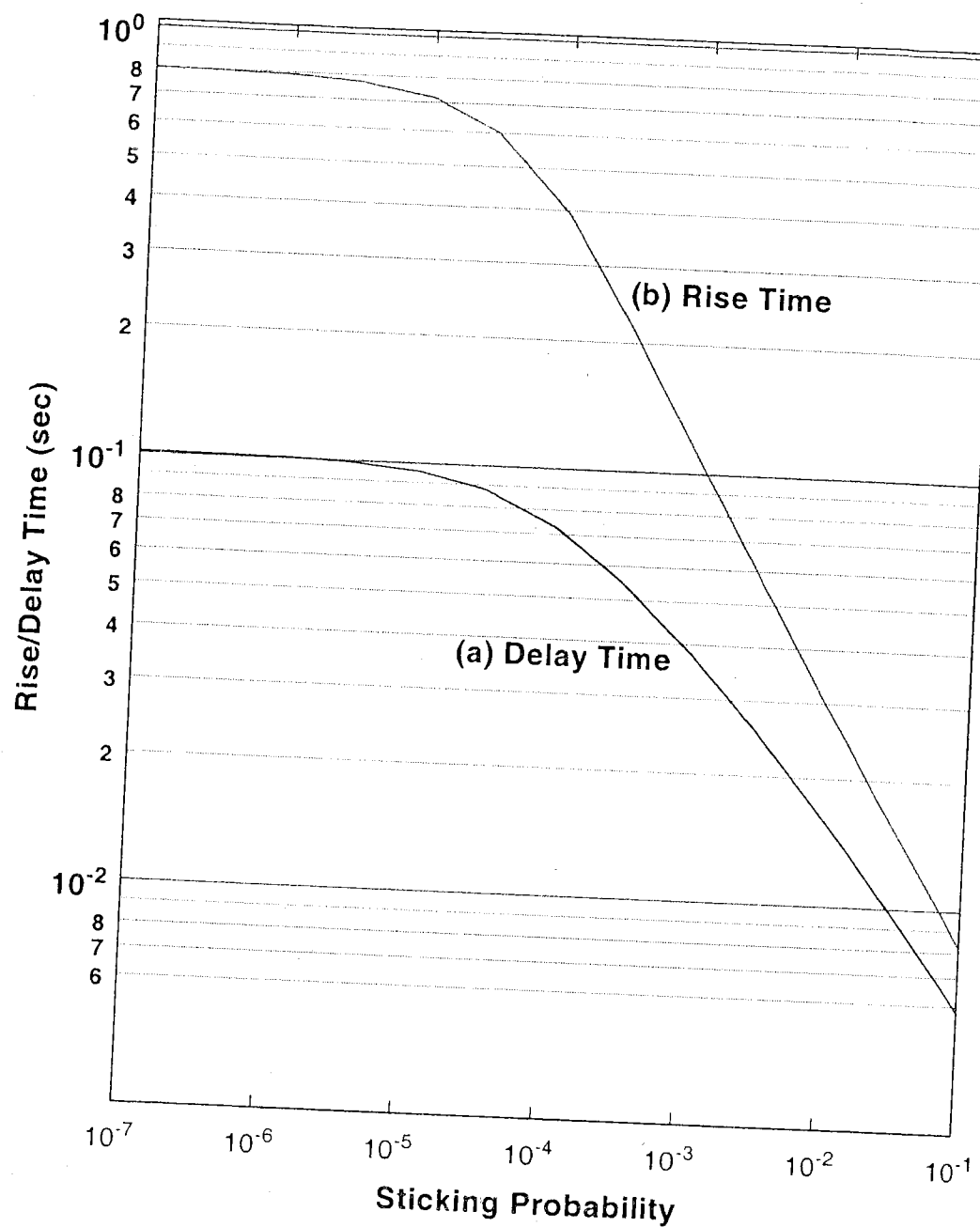


Figure 4.9 a) The time to reach 10% of the steady state value. (b) The time to reach 90% of the steady state value for a step change at the inlet of a 1 m long 1 cm diameter tube versus a constant sticking probability.

We estimate the average number of hits  $\bar{N}$  for a given transit time  $t_{trans}$  by considering the uniform equal step path shown in Figure 4.10. The distance  $d_B = \frac{2}{\pi}d$  is the average lateral distance from a point on a circular tube to any other point on the tube. The average total distance is  $s_{trans} = \bar{v} \cdot t_{trans}$ . By proportion of similar triangles

$$\bar{N}_{hit} = \frac{\Delta L}{L} = \frac{\sqrt{s_{trans}^2 - L^2}}{d_B}. \quad (4.27)$$

For our example above the average molecular velocity is 400 m/s and the transient time is about 1 s. The number of hits is then  $6.3 \times 10^4$ . The sticking probability at which significant loss starts to occur should be on the same order as the reciprocal of average number of hits, i.e.  $S_{significant} = 1.6 \times 10^{-5}$ , which agrees with the results of Figure 4.9.

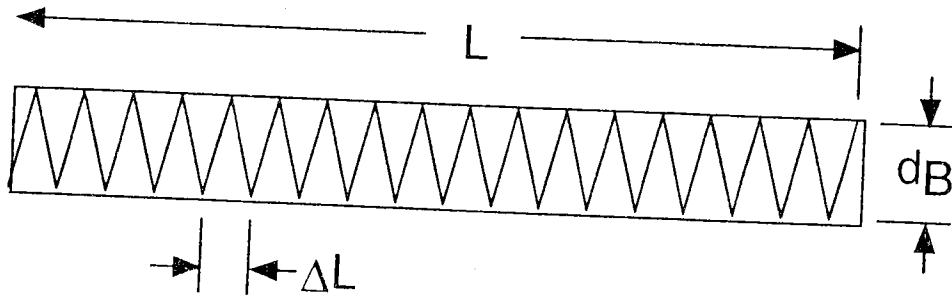


Figure 4.10 A uniform equal step path along the tube.

#### 4.5 Transient flow with a restricted exit

One deficiency of the simple long tube models of sections 4.2 and 4.4, when used to model our glass capillary array doser, is that the doser is a long tube terminated in a glass capillary array. Since the array has a conductance  $C_0$  that is small compared to the aperture

conductance of an open-ended tube, the outlet boundary condition of equation (4.3) is not valid. In this restricted outlet model we must specify the mixed boundary condition

$$\frac{\partial n}{\partial z}(z = L, t) + \frac{C_0}{AD} n(z = L, t) = \frac{C_0}{AD} n_L \quad (4.28)$$

Solving equation (4.2) with this outlet boundary condition and the inlet boundary condition of (4.3), we find the steady state solution

$$V(z) = n(z, t \rightarrow \infty) = n_L + \left( \frac{1}{C_0} + \frac{1}{C_{tube}} \right) \Phi_1 - \frac{1}{C_{tube}} \Phi_1 \frac{z}{L} \quad (4.29)$$

where  $C_{tube} = \frac{AD}{L}$ . Note that this solution is not consistent with the usual solution from standard vacuum flow calculations [19], where we would adjust the simple conductance combination  $\left( \frac{1}{C_0} + \frac{1}{C_{tube}} \right)$  for the reduction in conductance at the outlet. This difference can be accounted for by the differences in the inlet boundary conditions. The standard vacuum calculation assumes isotropic impingement from a large vessel at constant pressure, while our model forces a constant flow into the tube with no gas exiting the inlet.

The mixed boundary condition changes the problem from a simple initial-value boundary-value problem to the Sturm-Louiville problem with unevenly spaced eigenvalues,  $k_n$ , satisfying the equation

$$\varepsilon \cdot \cot(k_n L) = k_n L, \text{ where } \varepsilon \equiv \frac{C_0}{C_{tube}}. \quad (4.30)$$

Each eigenvalue,  $k_n$ , is in the interval  $(n-1)\pi < k_n L < (2n-1)\frac{\pi}{2}$  for  $n = 1, 2, 3, \dots$  and converges on the lower bound of each interval as  $n$  becomes large.

As before, we impose the initial condition that  $\Phi_0$  is established at  $t \rightarrow -\infty$ . Thus the initial condition is

$$n(z, t=0) = n_L + \left( \frac{1}{C_0} + \frac{1}{C_{tube}} \right) \Phi_0 - \frac{1}{C_{tube}} \Phi_0 \frac{z}{L}. \quad (4.31)$$

The general solution is then

$$n(z, t) = V(z) + \frac{\Phi_0 - \Phi_1}{C_{tube}} \cdot 2 \sum_{n=1,2,3,\dots} \frac{a_n}{(k_n L)^2} \cos(k_n L) \exp(-D \cdot k_n^2 t) \quad (4.32)$$

where

$$a_n = 1 - \frac{\varepsilon}{\varepsilon^2 + \varepsilon + (k_n L)^2} \quad (4.33)$$

The resulting flow is then

$$\Phi(z, t) = \Phi_1 + (\Phi_0 - \Phi_1) \cdot 2 \sum_{n=1,2,3,\dots} \frac{a_n}{(k_n L)} \sin(k_n L) \exp(-D \cdot k_n^2 t). \quad (4.34)$$

Figure 4.11 shows the exit fraction versus time calculated for several values of  $\frac{C_0}{C_{tube}}$ , using the tube dimensions from the example of section 4.4. This plot shows that the transient times increase, as the tube outlet becomes more restricted. At first, this result seemed counter intuitive, since with a restriction, we thought that the tube would fill to steady state more quickly. The tube does in fact fill more quickly, however it must fill to a

much higher density before achieving the steady state outlet flow. Thus the transient is approximately limited by the finite time to fill the tube at the rate  $\Phi_1$ . Finally, Figure 4.12 shows the rise and delay times for the 10% flow change as a function of outlet to tube conductance ratio. Each curve show a decrease in time as the outlet conductance is increased.

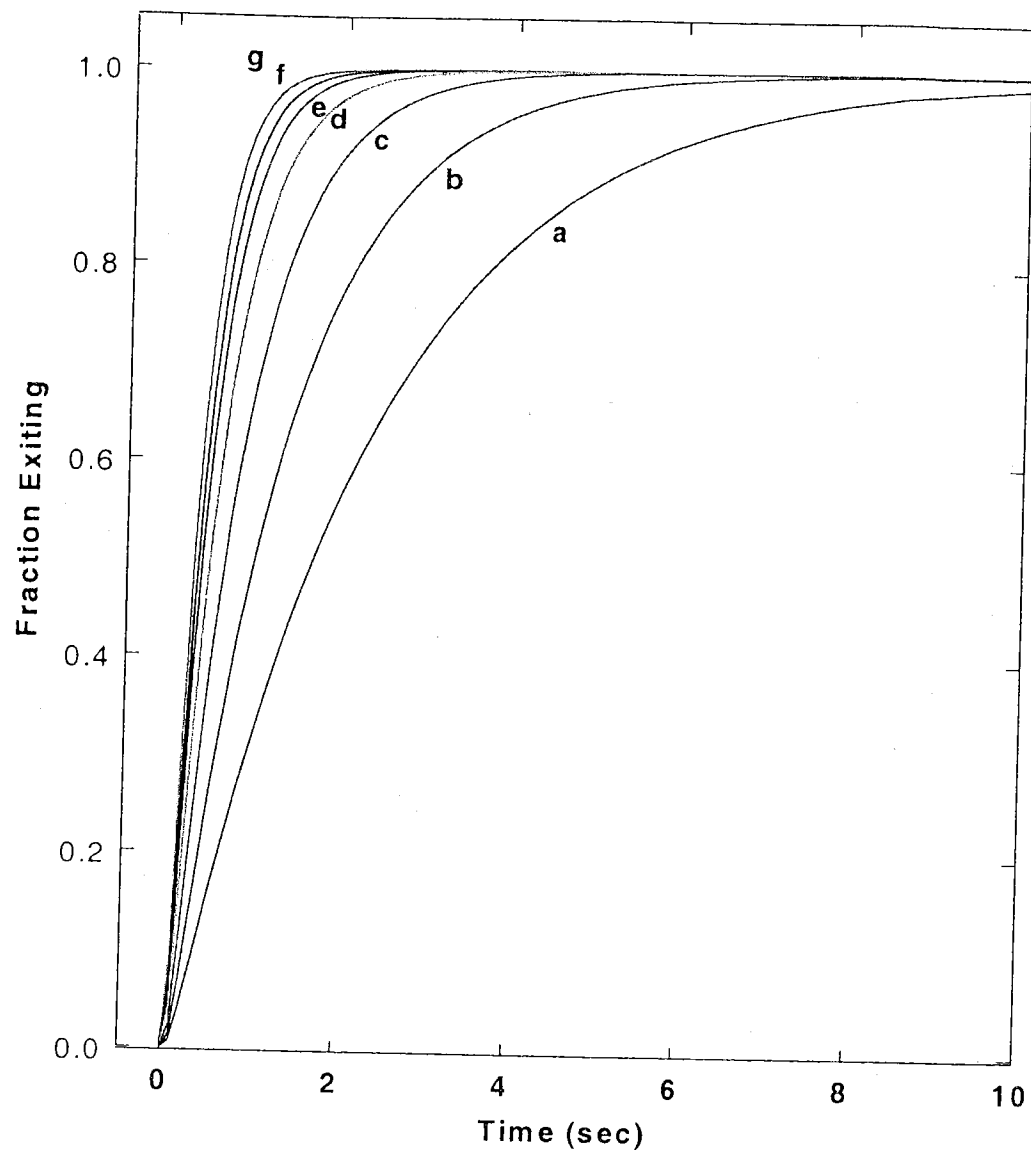


Figure 4.11 The fraction of gas exiting the 1m long 1cm diameter tube with a restricted exit for several values of the ratio of restriction conductance  $C_0$  to tube conductance  $C_{tube}$ : (a) 2.56, (b) 1.28, (c) 0.64, (d) 0.32, (e) 0.16, (f) 0.08, compared to the unrestricted tube with ratio (g) 0.013.

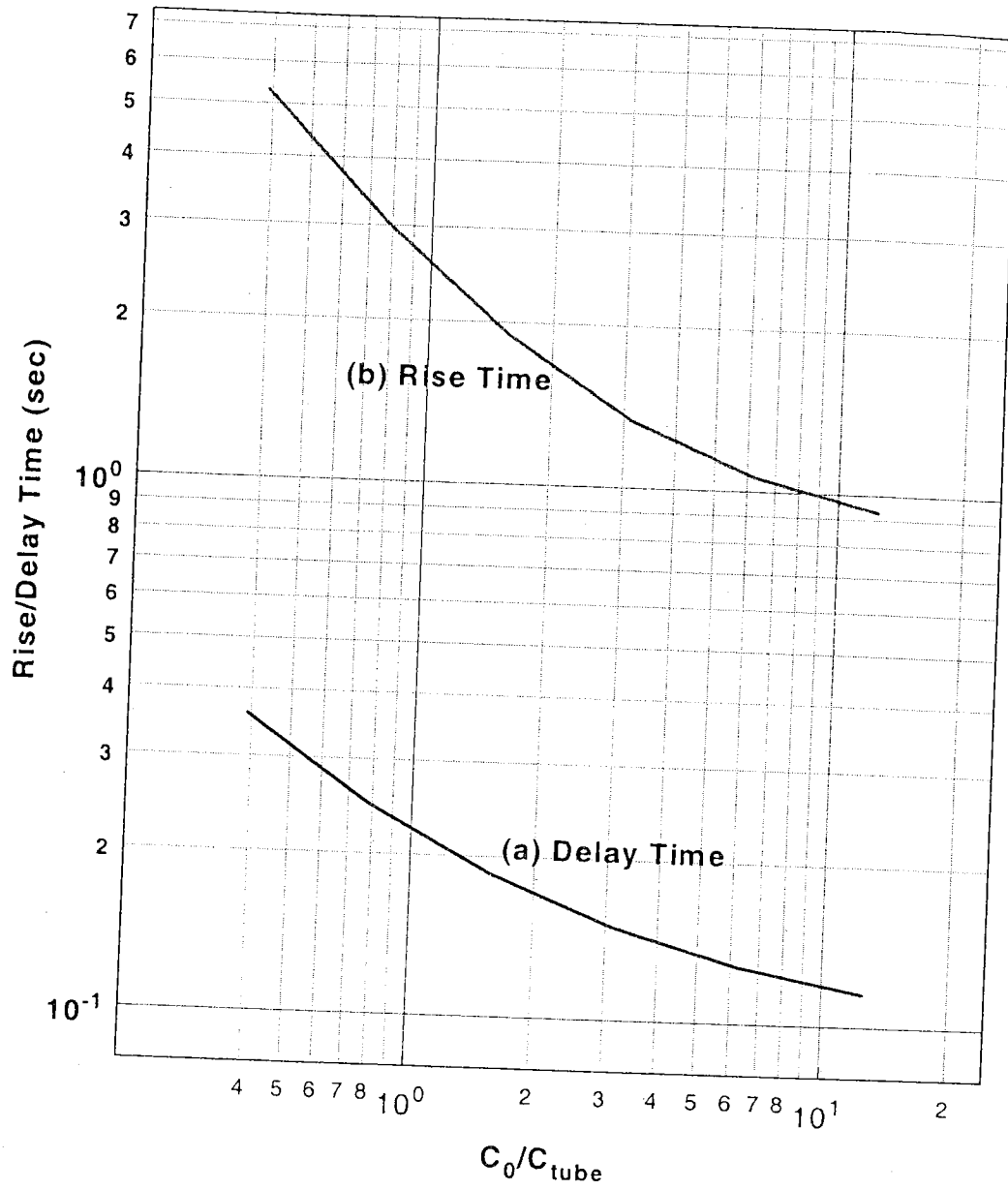


Figure 4.12 (a) The time to reach 10% of the steady state value. (b) The time to reach 90% of the steady state value for a step change at the inlet of a 1 m long 1 cm diameter tube versus the ratio of restriction conductance  $C_0$  to tube conductance  $C_{tube}$ .

#### 4.6 Conclusions, limitations, and further work

In an attempt to understand the transient molecular flow in a glass capillary doser we have examined three cases of long narrow tubes modeled with 1-D diffusion. Each case was chosen to elucidate a particular aspect of the molecular transient flow. The simple non-sticking case shows the relationship of the transient time to the ratio  $L^2/d$  and the average molecular velocity. The constant sticking probability case shows the strong dependence of the steady state flow on the sticking probability. This case further shows that the transient times are shorter for higher sticking probability, which was explained by the removal of molecules with larger numbers of wall hits as the sticking probability increases. We further demonstrated a simple estimate of the average number of wall hits for a given transit time down the tube and showed this to be consistent with the line-of-sight flow through the tube at unity sticking probability. Finally, the restricted flow case shows the effects of the restriction of the doser flow by the glass capillary array at the end of a long narrow tube. This case shows an increase in the transient times, as the outlet becomes more restricted.

In each case the model is limited to long narrow tubes where a 1-D diffusion model is applicable. We anticipate that short tubes could be modeled as well-mixed volumes and that intermediate length tubes would require direct dynamic simulations. The constant sticking probability model has many limitations. First, the sticking probability is unlikely to be a constant. However, if the sticking saturates very slowly with respect to the transient flow time, then the slowly varying sticking function could be included as a parameter in the constant sticking solution. Second, desorption of gas subsequent to adsorption has not been

included. Finally, finite residence time effects have not been considered along with the possible effect on the diffusion constant and the diffuse scattering assumptions.

Further work should include calculations for the basic adsorption models; e.g. Langmuir, dissociative, and BET models. These integro-differential equations can be solved by a successive approximation to a self-consistent solution. Since no closed form solution would be available, a systematic numerical study of the useful range of geometry and gas properties would be required. A systematic study of the specific geometry of each model remains to be done including the effects of temperature, tube material, and gas.

In chapter 5, we will apply the models of this chapter to the calibration of a glass capillary array doser, where the sticking of oxygen in the doser will be estimated. This calibrated doser will in turn be used to calibrate the differentially pumped mass spectrometer current against a known flow. We will demonstrate that accurate absolutely calibrated thermal desorption spectrometry can be achieved for the c(2x4) oxygen over-layer on Pd(110).

## 5 Calibrated Adsorption and Desorption

The absolute adsorption rate on a surface and the desorption rate from a surface measured as a function of the surface coverage and temperature provide detailed information about the kinetics of gas surface interactions and reactions [16]. In Chapter 2, we demonstrated the design and use of a differentially pumped mass spectrometer system with an absolutely calibrated molecular flow source routed to the bottom of the mass spectrometer shroud. This design provided a measurement of the molecular flux to the mass spectrometer aperture, which is linear over 4 decades of flux, with a characteristic pumping time of 6 ms. In Chapters 3 and 4 we have set forth a theoretical foundation to analyze the spatial distributions and transient effects in glass capillary array dosers so that we could understand their use as a calibrated molecular flux source for a calibrated thermal desorption spectrometer (CTDS) system. In this chapter we draw all of this work together using the O/Pd(110) system as a test case.

Testing the CTDS requires the measurement of an adsorbate/substrate system for which we have a reliable and repeatable method of producing a well-known coverage. The Pd(110) c(2x4)-O surface coverage has been determined by nuclear reaction analysis (NRA) [9] as well as by adsorption uptake measurements [7,36]. Scanning tunneling microscopy has provided further structural verification of the oxygen induced Pd reconstructions of Pd(110) [37-40]. Former members of our group have studied the subsurface oxygen on Pd(110)[41] and have provided a cleaned, oriented crystal in fair condition. In view of these further developments in the literature and the analysis of the

doser in chapters 3 and 4, we return to the O/Pd(110) system and reassess the capabilities and limitations of performing a CTDS measurement on a real surface.

The first section of this chapter reviews the current literature concerning oxygen coverage on Pd(110) surfaces. In the second section, we explain the changes to the experimental setup since the masters thesis, review the overall experimental setup, and describe the sample mounting and preparation procedures. The third section describes the basic sequence of calibration steps and shows some typical calibration results for both the gas source calibration and the mass spectrometer flow calibration. The fourth section shows the results of a study of the O/Pd(110) system. First using CTDS, we measured the oxygen c(2x4) coverage to be 0.44ML, in good agreement with other work. Then, using a modified King-Wells method to compare with the CTDS measurement, we find some disagreement in the coverages, concluding that the sample surface was not adsorbing uniformly. This section then continues with an analysis of the basic instrumental errors, followed by a detailed analysis of a series of oxygen calibration pulses. The analysis reveals a slow exponential process times an underlying non-sticking transient process. We will show that this slow exponential process is inconsistent with sticking in the doser, since the underlying transient exactly matches the shape predicted by the argon transient when the diffusion constant is adjusted for the molecular weight of oxygen. Finally, the last section summarizes the results and discusses possible modifications of the calibration procedures and the measurements.

## 5.1 A literature review of O/Pd(110)

He *et al*[26] discuss the oxygen induced phases determined by LEED and provide a schematic drawing showing three regions on a temperature versus exposure plot. First, at temperatures below 200K a “pseudo (2x1)” phase is created. From 200K to 400K a c(2x4) phase is created with coverages as high as 1 ML. Above 400K starting at low exposures, a “(2x3)-1D” phase exists, gradually converting reversibly to a c(2x4) phase as the exposure increases. Reaction of surface oxygen with background hydrogen or hydrogen from the bulk is thought to convert the structure from the c(2x4) to (2x3)-1D as the oxygen coverage is lowered, and is reversibly converted back to c(2x4) as the coverage is increased. It is generally agreed that the c(2x4) phase is accompanied by a Pd(1x2) added row reconstruction[37]. LEED shows a c(2x4) structure that reverts to p(1x2) after removal of the oxygen either by a clean-off reaction with hydrogen at room temperature and above[37] or by thermal desorption at 700K[26-28]. The Pd-p(1x2) reconstruction can be lifted to give the p(1x1) structure of the Pd(110) surface by annealing above 750K. The literature has not addressed the effects on the desorption spectra of the lifting of the Pd p(1x2) reconstruction during the linear temperature program typical in thermal desorption and considerable disagreement remains [37,38,40] over the exact position of the c(2x4) oxygen atoms and the dynamics of their desorption.

Thermal desorption shows two high temperature desorption features labeled  $\beta_1$  (~720K) and  $\beta_2$  (~815K), where  $\beta_1$  is generally believed to be due to subsurface oxygen and  $\beta_2$  is an associative first order desorption from surface sites[26-28,36]. Following adsorption at 100K, the  $\beta_2$  desorption feature appears first, becoming saturated at ~0.8L

exposure. The  $\beta_1$  feature then grows, filling in as the exposure increases to 5L[27]. At 475K,  $\beta_2$  is again populated for low coverages but the  $\beta_1$  now requires much larger exposures. The  $\beta_1$  feature first appears at about 10 L, but the  $\beta_1$  peak only becomes similar in intensity to the  $\beta_2$  peak at exposure over 7000 L[28]. Goschnick *et al*[7] use a two mass spectrometer technique, similar to the King-Wells method, to measure the adsorption uptake. At 427K the sticking probability drops precipitously to near zero at a coverage  $\theta = 0.5 \text{ ML}$ , where  $1 \text{ ML} = 9.4 \times 10^{14} \text{ atoms cm}^{-2}$ . Recently, Yagi *et al* have shown similar results at 473K and further show a distinct turnover in the coverage versus exposure plot at 0.8L and  $\theta = 0.5 \text{ ML}$  coverage. This distinct drop in the sticking probability provides a means of producing a 0.5ML coverage of oxygen that is not strongly dependent on either temperature or exposure, which should be advantageous for achieving reproducible c(2x4) oxygen covered surfaces.

## 5.2 The Experimental setup

In my masters thesis [10] the c(2x4) oxygen coverage on Pd(110) was measured for the  $\beta_2$  peak to be  $\theta = 1.0$  as compared with  $\theta = 0.50$  measured by nuclear reaction analysis[9]. After an exhaustive search for a factor of 2 error we determined this error to be due to several aspects of the design. Originally, we assumed a steady state molecular flow model for the region surrounding the mass spectrometer ionizer; however, the ionizer is primarily in the line of sight of the sample through the aperture. Thus, the molecules entering the mass spectrometer through the aperture have a substantial number ionized before becoming part of the accommodated gas within the mass spectrometer shroud. This

effect could explain an overestimate, since the gas from the sample traveled line-of-sight to the ionizer, while the calibrating gas did not. Subsequently, we have added a conical obstruction in front of the ionizer. We have also investigated the use of a glass capillary array doser, in conjunction with our calibrated molecular flow source, to produce a known molecular flux for absolutely calibrating the differentially pumped mass spectrometer for calibrated thermal desorption spectrometry (CTDS). The use of the doser as a known molecular flux source more nearly simulates the flux desorbing from a sample provided that the distance from the sample to the aperture is less than 1mm. As shown in section 2.3.3, the sample flux to the aperture is then essentially equal to the aperture area for  $\cos^1$  through  $\cos^5$  law desorption distributions.

### 5.2.1 Changes to the system since the MS Thesis

The measurement system is substantially the same as described in chapter 2 with the following exceptions. First, as suggested, the line-of-sight from the mass spectrometer shroud aperture to its axial ionizer is now obstructed with a small solid metal cone mounted on tungsten cross wires at the end of the conical section of the shroud as shown in Figure 5.1.

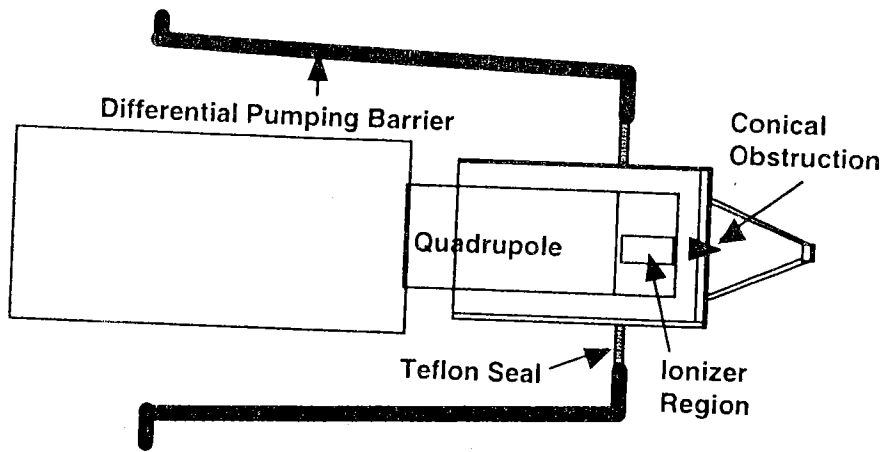


Figure 5.1 The mass spectrometer shroud with the small solid metal cone obstructing the line-of-sight path from the aperture to the axial ionizer.

Second, the doser has been modified to mount in a 10 inch travel bellows xyz manipulator positioned on the UHV chamber opposite to and coaxial with the mass spectrometer. This modification required the doser tube to be extended to 62cm. Third, the glass capillary array is now mounted with ceramic adhesive instead of Teflon seals as shown in Figure 3.3. This eliminated several small leaks that became apparent from the initial flux distribution measurements leading to the work described in chapter 3. Fourth, the 0.25 inch formed bellows tube was replaced between the gas source volume and the positive shutoff capillary valve due to damage. The gas source volume subsequently changed to  $430 \pm 3 \text{ cm}^3$ . Finally, the mass spectrometer shroud aperture was damaged and was resized from 3.48 mm to a 3.63 mm diameter.

### 5.2.2 Preparation of the Pd(110) sample

The Pd(110) sample is a ~0.5mm thick truncated ellipse having a polished surface area of  $0.8877\text{cm}^2$ . It was oriented by Laue x-ray diffraction to within  $1^\circ$  of the (110) surface and polished mechanically to  $0.05\mu\text{m}$  with alumina. The sample is "well used" and the path of the spot welded wires is visually obvious from the front of the crystal. The edges have rounded and due to the thinness of the sample they could not be safely removed by further polishing. The sample was mounted vertically from the tantalum bars of a cold-finger by two 0.15mm tungsten wires spot-welded to the back of the sample. The cold-finger is capable of liquid nitrogen cooling and the tantalum bars are electrically isolated by a sapphire spacer to provide both cooling and resistive heating.

The sample was cleaned by repeated 1000eV argon ion sputtering and annealing to 1150K. Surface carbon was removed by annealing at 367K in  $5 \times 10^{-7}\text{torr}$  of oxygen followed by TDS to 1100K. The surface carbon was titrated away by monitoring the CO production from the sample as it was repeatedly background dosed with oxygen at 367K, followed by annealing to 1100K until no CO was observed. Auger electron spectroscopy revealed no discernable contaminants. In spite of the rough condition of the sample, it produced a sharp (110) p(1x1) LEED pattern over the entire sample. LEED also showed a discernable c(2x4) pattern when dosed to saturation at 475K.

### 5.3 The Basic Calibration Procedure

In this section, we list the methods of calibration of both the gas source and the mass spectrometer. The sequence of calibration determinations is as follows:

- 1) The volume of the gas effusion source is determined by the expansion of argon gas, as described in section 2.3.1.
- 2) The effusion constant for argon gas is determined and effusion constants for other gases are calculated from the argon value by correcting for their molecular weight as described in section 5.3.1 below.
- 3) The fraction of doser gas entering the aperture is determined as described in chapter 3.
- 4) The mass spectrometer signal versus aperture flow is determined by the integral method and the peak method as shown in section 5.3.2 below.

### 5.3.1 Gas source calibration

The characteristic constant for effusion from the calibrated molecular flow source was determined for Argon gas at 295K with an initial number density  $n_0 = 1.201 \times 10^{20} \cdot m^{-3}$ . Figure 5.2 shows the number density versus time as the gas leaked through the positive shutoff capillary leak valve (PSO) into the vacuum chamber. A least squares fit to this data with  $n(t) = n_0 \exp(-\alpha_{Ar} t)$  yielded  $\alpha_{Ar} = 4.3597 \times 10^{-4} \cdot s^{-1}$ .

Adjusting the effusion constant for the mass of O<sub>2</sub> by  $\alpha_{O_2} = \sqrt{M_{Ar} / M_{O_2}} \cdot \alpha_{Ar}$ , we have the oxygen effusion constant  $\alpha_{O_2} = 4.871 \times 10^{-4} \cdot s^{-1}$ . For a dose with the PSO opened from  $t_0$  to  $t_1$  with the initial and final number densities  $n_0$  and  $n_1$ , respectively, the flow from the source at the valve is  $\Phi(t) = \alpha_{gas} V n(t)$  for  $n(t) = n_0 \exp(-\alpha_{dose}(t_1 - t_0))$ , where

$$\alpha_{dose} = \frac{\ln(n_0) - \ln(n_1)}{t_1 - t_0}$$

The  $\pm 3\%$  systematic uncertainty in the spinning rotor tangential momentum accommodation coefficient  $\sigma$  most significantly determines the accuracy of  $n(t)$  and therefore  $\Phi(t)$ . However, the rate of gas exiting the doser could be significantly affected by adsorption in the doser.

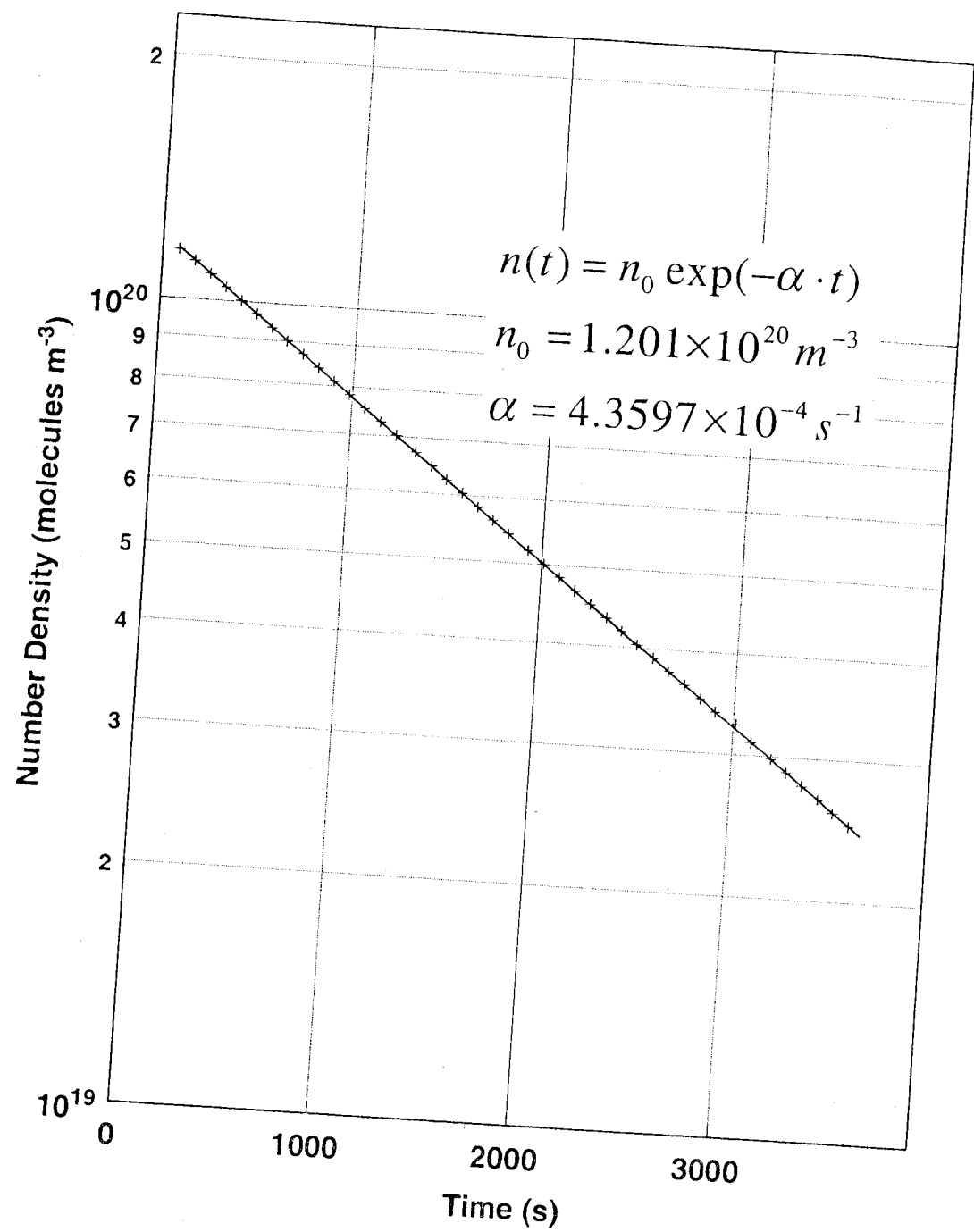


Figure 5.2 The argon number density in the gas source as the gas effuses through the positive shutoff capillary valve. The plus signs mark every forth data point.

### 5.3.2 Mass spectrometer calibration

We have previously demonstrated that the mass spectrometer current versus flow is linear over at least four orders of magnitude, section 2.3.3. Using the flow from the source through the glass capillary array doser as a known molecular flux, we calibrate the differentially pumped mass spectrometer in two ways. First, we start the flow and wait for the steady state current value  $i_{ss}$  to be achieved. The steady state calibration value is then

$$\lambda_{ss} = \frac{i_{ss}}{\Phi_{ms}(t_1)} \text{ where flow entering the mass spectrometer is } \Phi_{ms} = \Phi_s(t_1)r_d, \text{ and where}$$

$\Phi_s(t_1)$  is the flow leaving the doser and  $r_d = 0.07828$  is the previously determined fraction of the source gas reaching the mass spectrometer aperture at a distance  $d = 0.0635mm$ . Second, the time integral of the mass spectrometer current  $i(t)$  is compared to the total gas released from the source given by

$$N_{total} = V \cdot \frac{\alpha_{gas}}{\alpha_{dose}} r_d \cdot n_0 (1 - \exp(-\alpha_{dose}(t_1 - t_0))). \quad (5.1)$$

The integral method calibration factor  $\lambda_{int}$  is then given by

$$\lambda_{int} = \frac{N_{total}}{\int_{t_0}^{t_1^+} (i(t) - i_{base}) dt} \quad (5.2)$$

where  $t_1^+$  indicates that we integrate beyond the PSO shutoff time until  $i(t)$  returns to baseline.

Figure 5.3 shows the mass spectrometer current versus time of a typical 100s pulse of oxygen gas for a doser to aperture distance  $d = 0.0635mm$ .

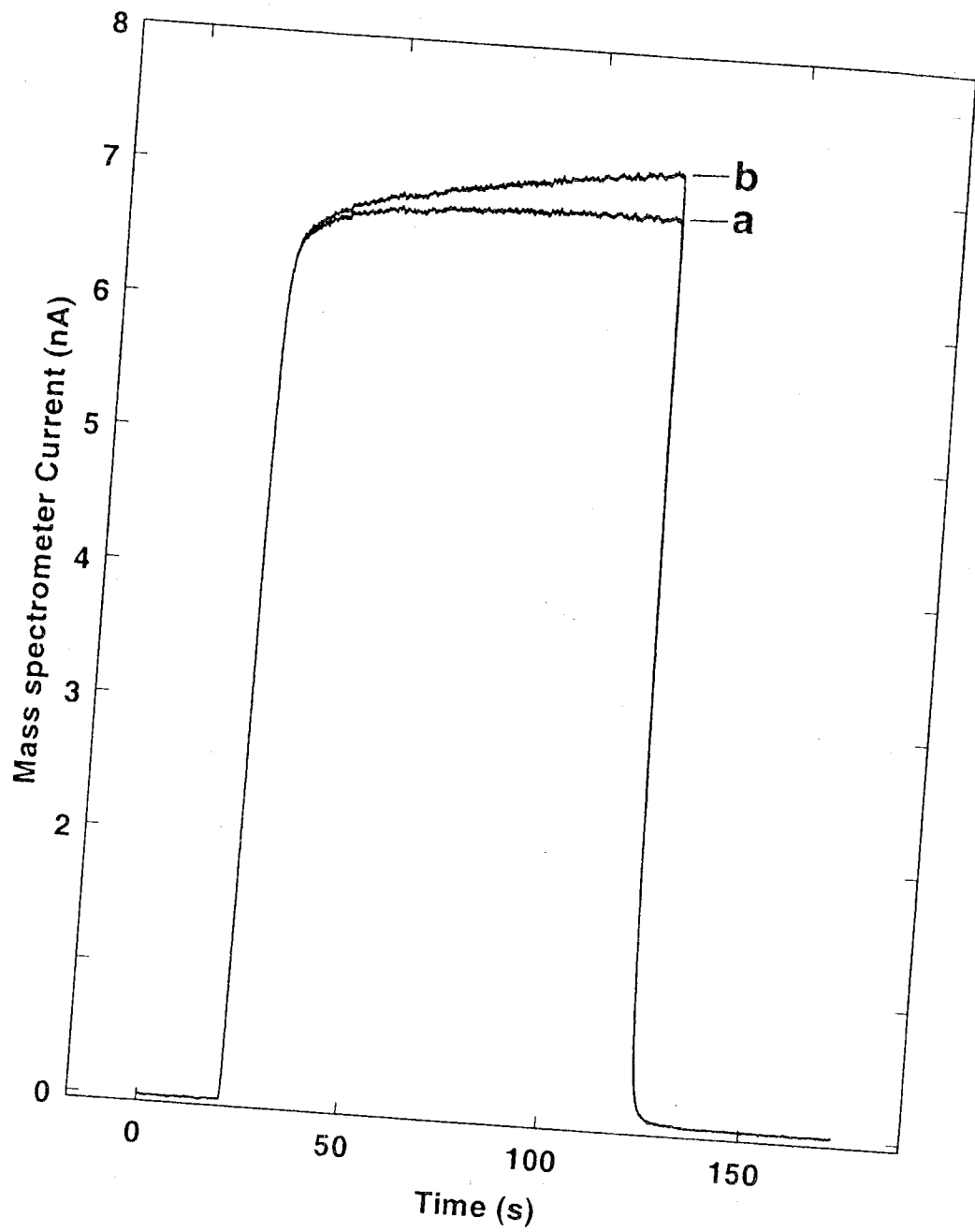


Figure 5.3 Typical pulse for calibrating the differentially pump mass spectrometer for flow. (a) Measured current; (b) current corrected for the exponential drop in gas source flow with  $\alpha_{dose} = 4.594 \times 10^{-4} \cdot s^{-1}$

Curve (a) is the recorded mass spectrometer current, which appears to become steady state after  $\sim 60$ s. When we corrected this measured current for the slow exponential drop in the gas source flow during the dose, we have curve (b), thus revealing the non-steady state nature at  $t_1$ . We subsequently refer to the steady state method as the peak method. Unless we are willing to wait for true steady state, such a method of calibration arbitrarily depends on the point at which we choose to stop the dose. The integral method takes a more pragmatic approach, relating the total gas released to the integral of the current.

The characteristic dose constant was  $\alpha_{dose} = 4.594 \times 10^{-4} \cdot s^{-1}$  and the integral of the mass spectrometer current was  $I_{int} = 3.54 \times 10^{-7} \cdot C$ . The integral method calibration factor is  $\lambda_{int} = 1.376 \times 10^{21} \cdot s^{-1} A^{-1}$ . The calibration factor using the peak value at the end of the pulse was  $\lambda_{peak} = 1.356 \times 10^{21} \cdot s^{-1} A^{-1}$ , which is within about 1% of the integral method value.

## 5.4 Results

Presently, we demonstrate the application and use of the instrument using these methods to provide CTDS of the c(2x4) oxygen over-layer on a Pd(110) surface. We further demonstrate a modified shutter-less King-Wells adsorption measurement [13] using the doser and the step-flow nature of the calibrated flow source. This adsorption experiment is similar to that of Goschnick *et al* [7] but uses a single mass spectrometer. We show that the CTDS successfully determines the coverage consistent with those reported in the literature[7,9,40] but the modified King-Wells measurement disappointingly shows a 27% lower coverage than is measured by CTDS. Next, we analyze the

instrumental measurement uncertainties showing how they affect the CTDS and uptake measurements. We then show a detailed analysis of a series of oxygen calibration pulses, revealing their underlying transient behavior and showing that this behavior is not consistent with significant sticking in the doser tube.

#### 5.4.1 Calibrated thermal desorption spectrometry (CTDS) on O on Pd(110)

The Pd(110) crystal was cleaned as described in section 5.2.2 and dosed with 99.99996% pure oxygen gas. Figure 5.4 shows the sequence of calibrated thermal desorption spectra dosed at 310K at a distance of 0.635mm from the doser with the temperature ramped at  $5Ks^{-1}$ . The calibration factor for this experiment was  $\lambda = 1.716 \times 10^{22} s^{-1} A^{-1}$ . As the total gas released from the dose increases, the measured coverage increases. The spectra evolve from a single  $\beta_2$  peak at low doses to a distinct  $\beta_1, \beta_2$  complex at high dose. The coverage measured for the CTDS (e) where the  $\beta_1$  is just appearing is 0.438, which we take as our measurement of the c(2x4) O coverage.



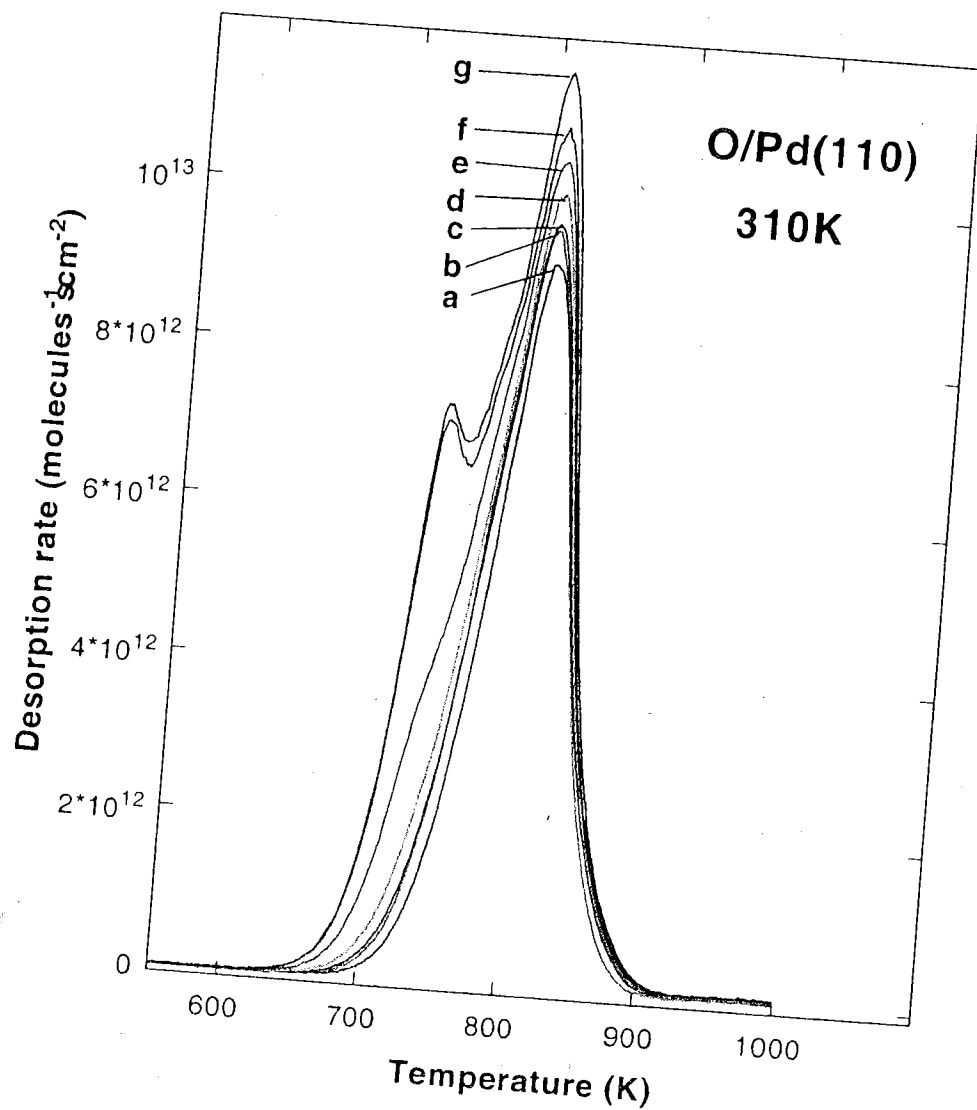


Figure 5.4 CTDS of oxygen on Pd(110) at 310K, with coverages (a) 0.313, (b) 0.335, (c) 0.349, (d) 0.379, (e) 0.438, (f) 0.519, and (g) 0.545. The calibration factor was  $\lambda = 1.716 \times 10^{22} \text{s}^{-1} \text{A}^{-1}$

We dosed the sample at very close distances  $d = 0.0635\text{mm}$ , where the molecules scattered from the surface have a high probability of scattering from the doser and immediately re-impinging on the sample. The possibility of multiple scattering between the doser and the sample complicates the determination of the total impingement. However, as a measure of the size of the dose, we used the total amount of gas released from the source and compare this value to the coverage measured by CTDS. Figure 5.5 shows the coverage measured by CTDS versus the total gas released in each dose. There is a an obvious knee and corresponding reduction in the uptake of the sample after doses where the  $\beta_1$  peak appears, corresponding to the quasi-saturation of the c(2x4) over-layer and the subsequent slower uptake creating subsurface oxygen attributed to the  $\beta_1$  feature. Similar results are found in Goschnick *et al.*[7] and Yagi *et al*[36], where the coverage is plotted against the exposure for a background dose.

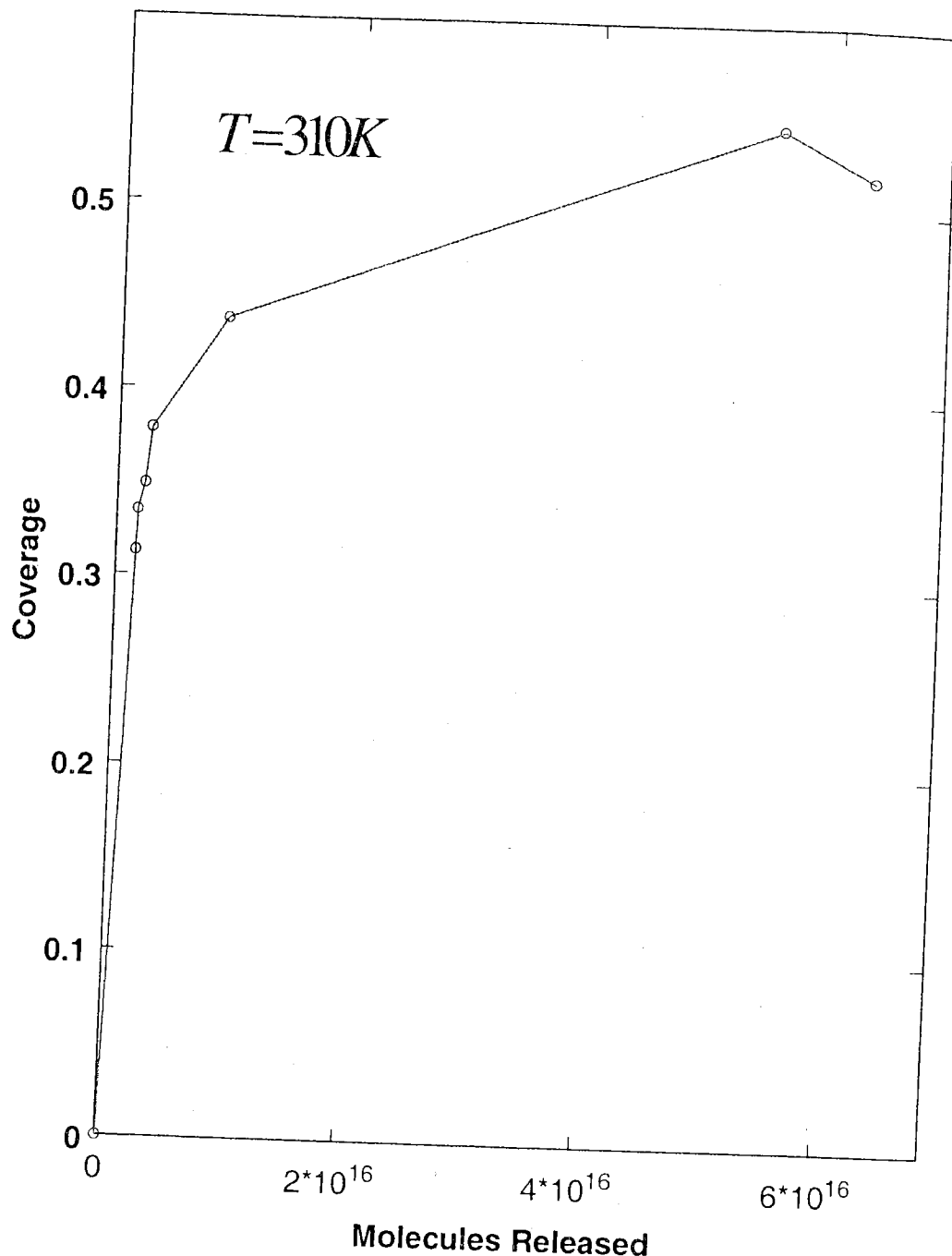


Figure 5.5 Coverage of atomic oxygen on Pd(110) measured by CTDS versus the total gas released in each dose at 310K.

### 5.4.2 Comparison of uptake measurements with the TDS

The ability of the positive shutoff capillary leak valve to provide a step change in the flow to the inlet of the doser suggests a variation on the method of King and Wells [13]. In our version, having only one mass spectrometer, we measured the background pressure in the chamber while the dose proceeds to saturation. As usual, the background pressure is modified by the uptake of gas onto the sample. Thus, we start with the sample in front of the doser with the PSO off. The differential pumping of the mass spectrometer is bypassed by opening a valve so that the signal is proportional to background pressure in the main chamber. The PSO is then opened and the mass spectrometer signal climbs to a first plateau while the sample is adsorbing gas, as illustrated schematically in Figure 5.6. Then as the sample saturates, the background pressure climbs to its final plateau and the PSO is shut. In order to estimate what the background pressure versus time would have been without adsorption by the sample, we reset the pressure in the gas source and re-dose the now-saturated sample. The height of the final plateau is proportional to the known flow into the chamber and thus provides the calibration of the mass spectrometer signal in terms of molecules per second. The difference between the two dose measurements is thus an estimate of the average uptake rate over the entire sample.

Referring to Figure 5.6, we let  $I_1(t)$  and  $I_2(t)$  be the mass spectrometer signals for the chamber background gas and  $n_1(t)$  and  $n_2(t)$  are the number densities in the gas source, where the subscripts refer to the first and second dose, respectively. The positive shutoff capillary valve is open at  $t_0$  and closed at  $t_1$ .

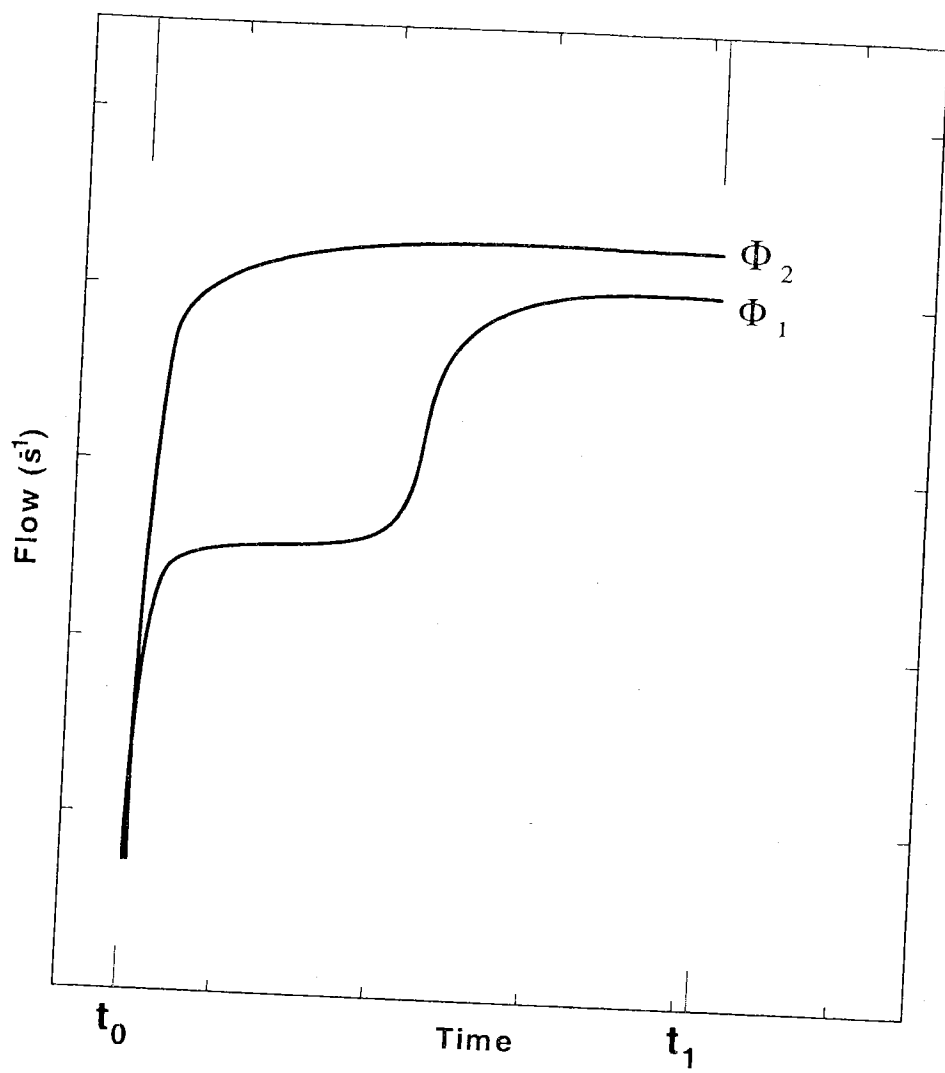


Figure 5.6 Schematic representation of the double dose mass spectrometer signals in our modified King-Wells experiment.

The gas leaving the doser is estimated to be  $\alpha_{gas} \cdot V \cdot n_i(t)$ , ignoring adsorption inside of the doser. Since the adsorption processes on the sample were most likely to have been closest to saturation at the end of the second dose, we use

$$\lambda = \frac{\alpha_{gas} \cdot V \cdot n_2(t_1)}{I_2(t_1) - I_{2_{base}}} \quad (5.3)$$

as the estimate of the flow calibration for the experiment, where  $I_{2_{base}}$  is the baseline current after the mass spectrometer settles. The flow into the chamber less the adsorption on the sample can now be estimated as

$$\Phi_i(t) = \lambda \cdot (I_i(t) - I_{base}). \quad (5.4)$$

The average rate of uptake by the sample is then given by the difference

$$r_{uptake}(t) = \Phi_2(t) - \Phi_1(t) \quad (5.5)$$

and the total uptake by the sample is

$$N_{uptake}(t) = \int_{t_0}^t r_{uptake}(t') dt'. \quad (5.6)$$

If  $n_1(t)$  and  $n_2(t)$  are different, then since  $\Phi_2$  should be the curve that results if the sample does not adsorb, we must multiply  $\Phi_2$  in equation (5.5) by  $n_1(t_0)/n_2(t_0)$  to correct the calibration. If we assume that the sample is uniformly dosed and that the sample surface is uniform, and subsequently adsorbs the dose uniformly, then the coverage is given by

$$\theta(t) = \frac{N_{\text{uptake}}(t)}{n_s A} \quad (5.7)$$

where  $n_s$  is the site density on the surface.

We have measured the uptake rates of the sample dosed at 310K, 400K, and 475K with oxygen at a distance of 5.08mm. Each dose started with a gas source number density of  $8.28 \times 10^{19} \text{ m}^{-3}$  and lasted for 100s, achieving a total release of  $1.69 \times 10^{15}$  molecules. The sample was double dosed to measure the uptake as shown in Figure 5.7, Figure 5.8, and Figure 5.9. After each double dose a CTDS was taken as shown later in Figure 5.10.

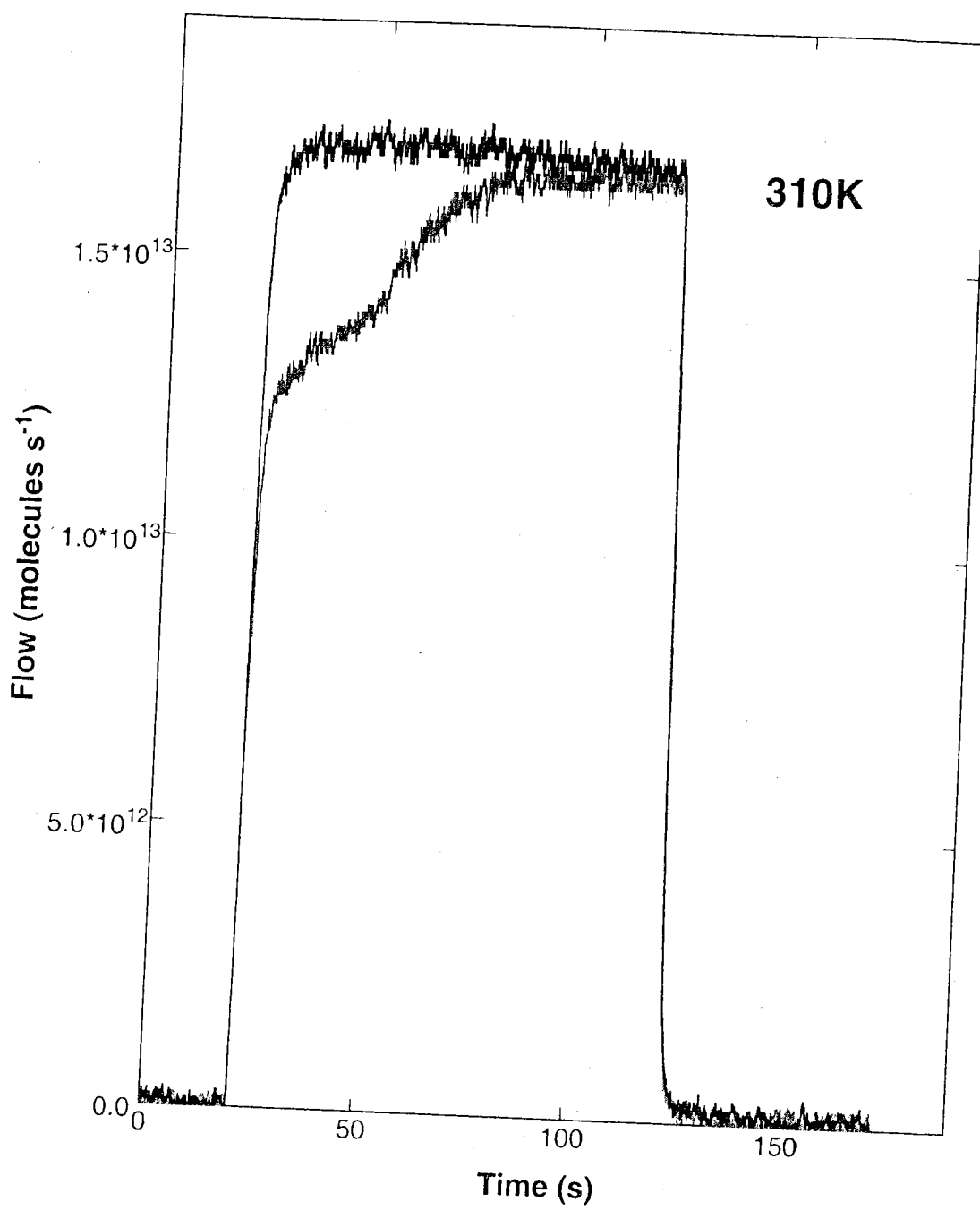


Figure 5.7 Flow of oxygen gas into the chamber during a double dose of the Pd(110) crystal at 310K with a calibration factor,  $\lambda = 2.59 \times 10^{22} s^{-1} A^{-1}$ .

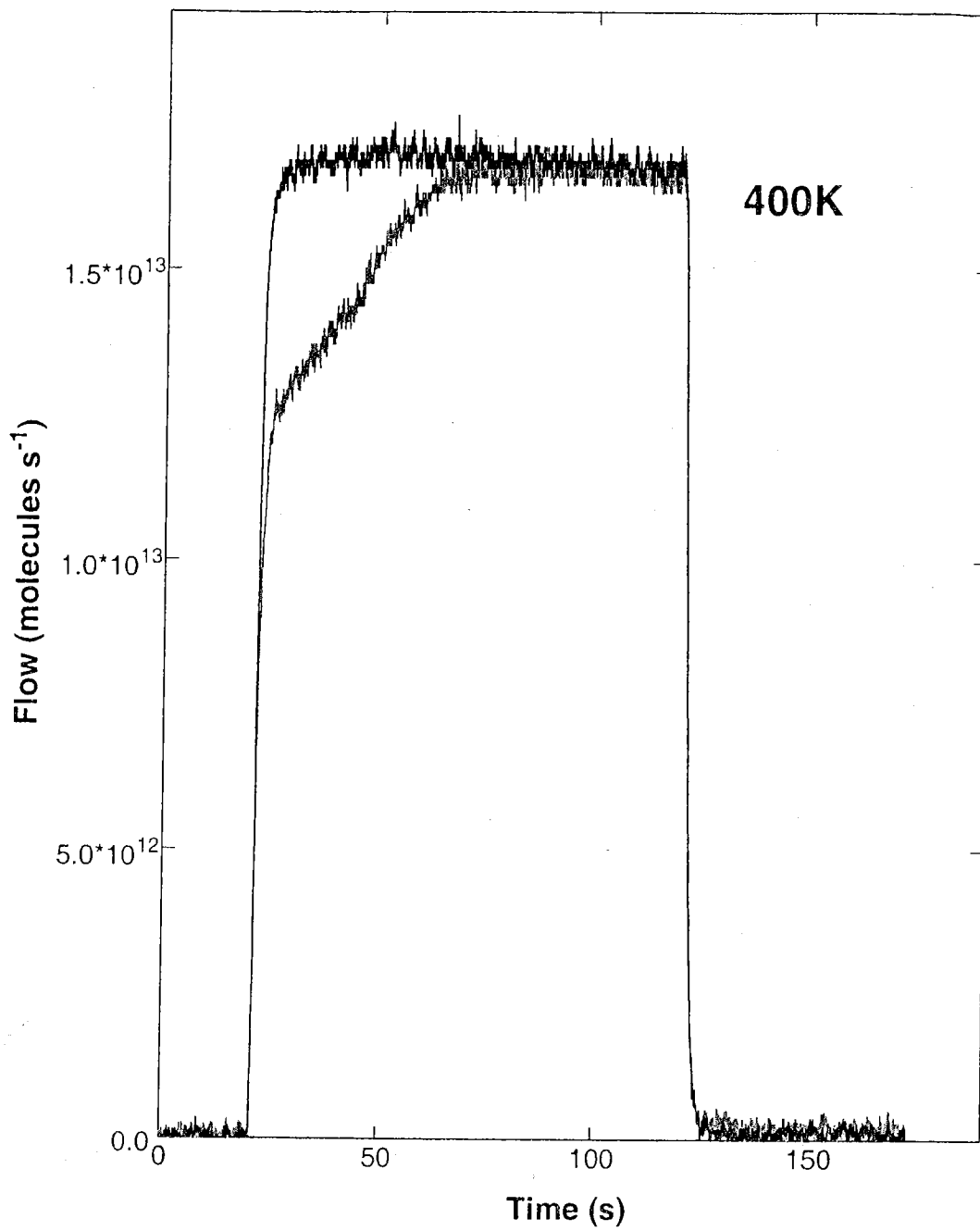


Figure 5.8 Flow of oxygen gas into the chamber during a double dose of the Pd(110) crystal at 400K with a calibration factor,  $\lambda = 2.70 \times 10^{22} \text{ s}^{-1} \text{ A}^{-1}$ .

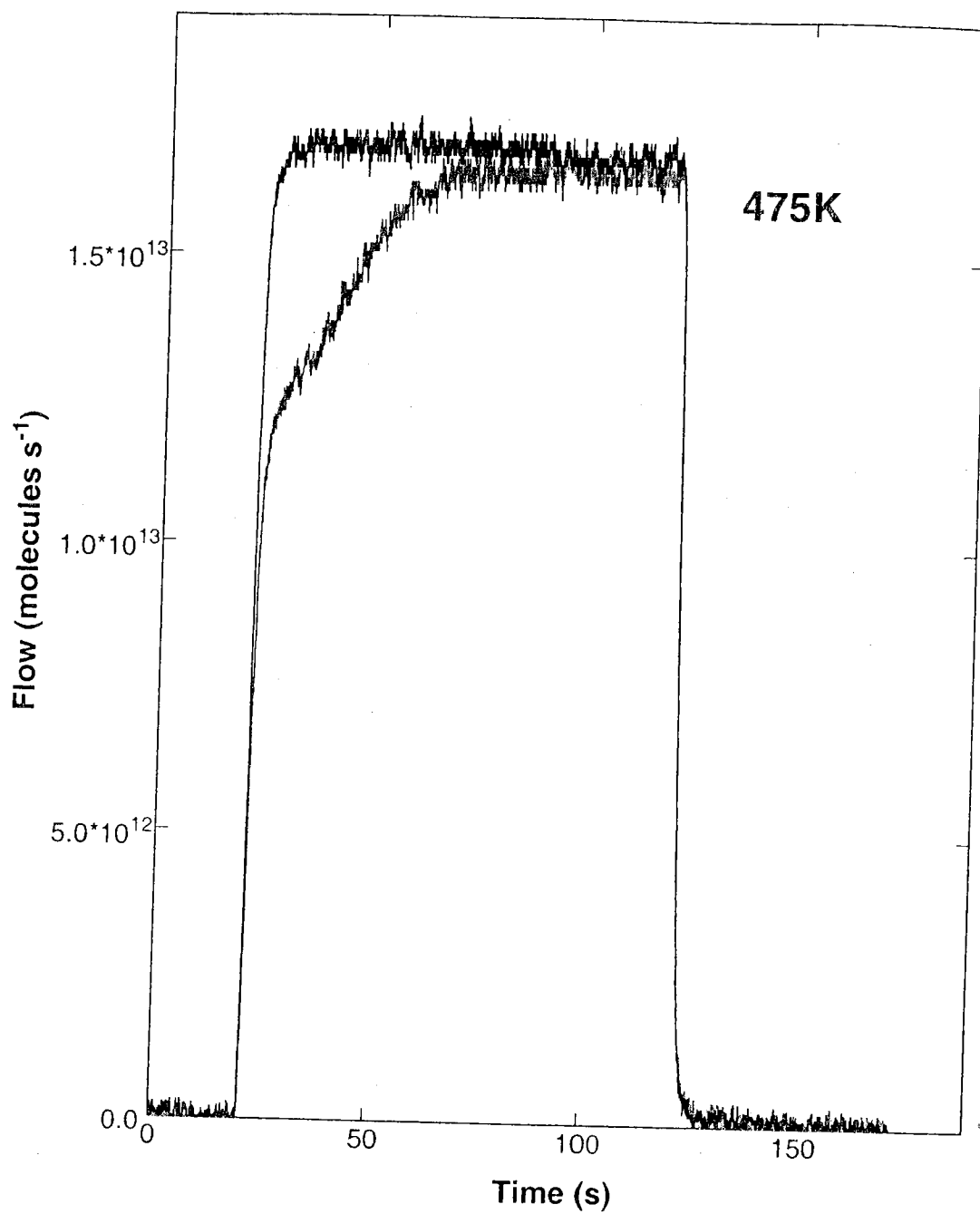


Figure 5.9 Flow of oxygen gas into the chamber during a double dose of the Pd(110) crystal at 475K with a calibration factor  $\lambda = 2.76 \times 10^{22} s^{-1} A^{-1}$ .

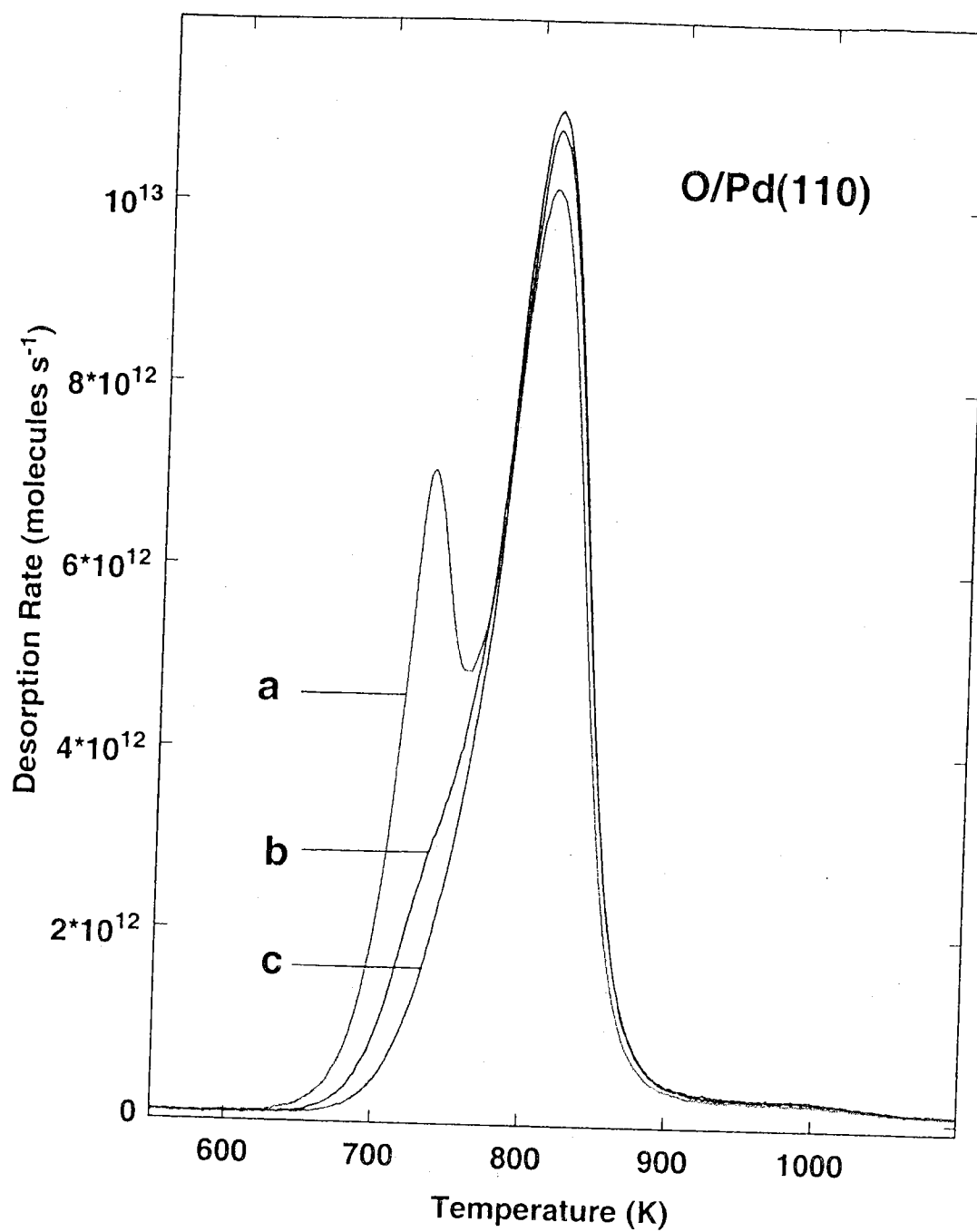


Figure 5.10 CTDS of oxygen on Pd(110) for each of the dose pairs at temperature and coverage: (a) 310K, 0.500, (b) 475K, 0.442, and (c) 400K, 0.409.

As described above, the mass spectrometer current is calibrated in terms of the rate of molecules flowing into the chamber using equation (5.4). The +6% shift of the calibration factor from the first measurement to the last is unexplained and may be due to sticking or multiplier gain effects to be discussed in the next section. Taking the difference between the flow for the second and first dose in each dose pair, we obtain the uptake rates versus time. These uptake rates are integrated to get the total uptake versus time. If the crystal surface, of area  $0.8877\text{cm}^2$ , adsorbs uniformly and no other surfaces adsorb significantly, we estimate the coverage of the sample versus time from the total uptake versus time. The corresponding uptake rate versus coverage is plotted in Figure 5.11, Figure 5.12, and Figure 5.13.

The uptake rates appear similar to the sticking coefficient curves of Goschnick *et al.* [7] and Yagi *et al.*[36], initially constant and then falling precipitously to near zero as the sample saturates. The final coverages are 30% lower than the coverages measured by the corresponding CTDS measurements shown in Figure 5.10. The initial uptake rates are around  $4\times10^{12}\text{s}^{-1}$  with the 475K initial uptake being 5% higher. Table 5.1 shows the final oxygen coverages measured by both CTDS and our modified King-Wells method.

For comparison with the literature, we also show the coverage measured with the King-Wells method as a function of the cumulative number of molecules released from the doser for each Temperature in Figure 5.14. The qualitative shape is in good agreement with Yagi *et al.*, but the absolute coverage is low by 30%.

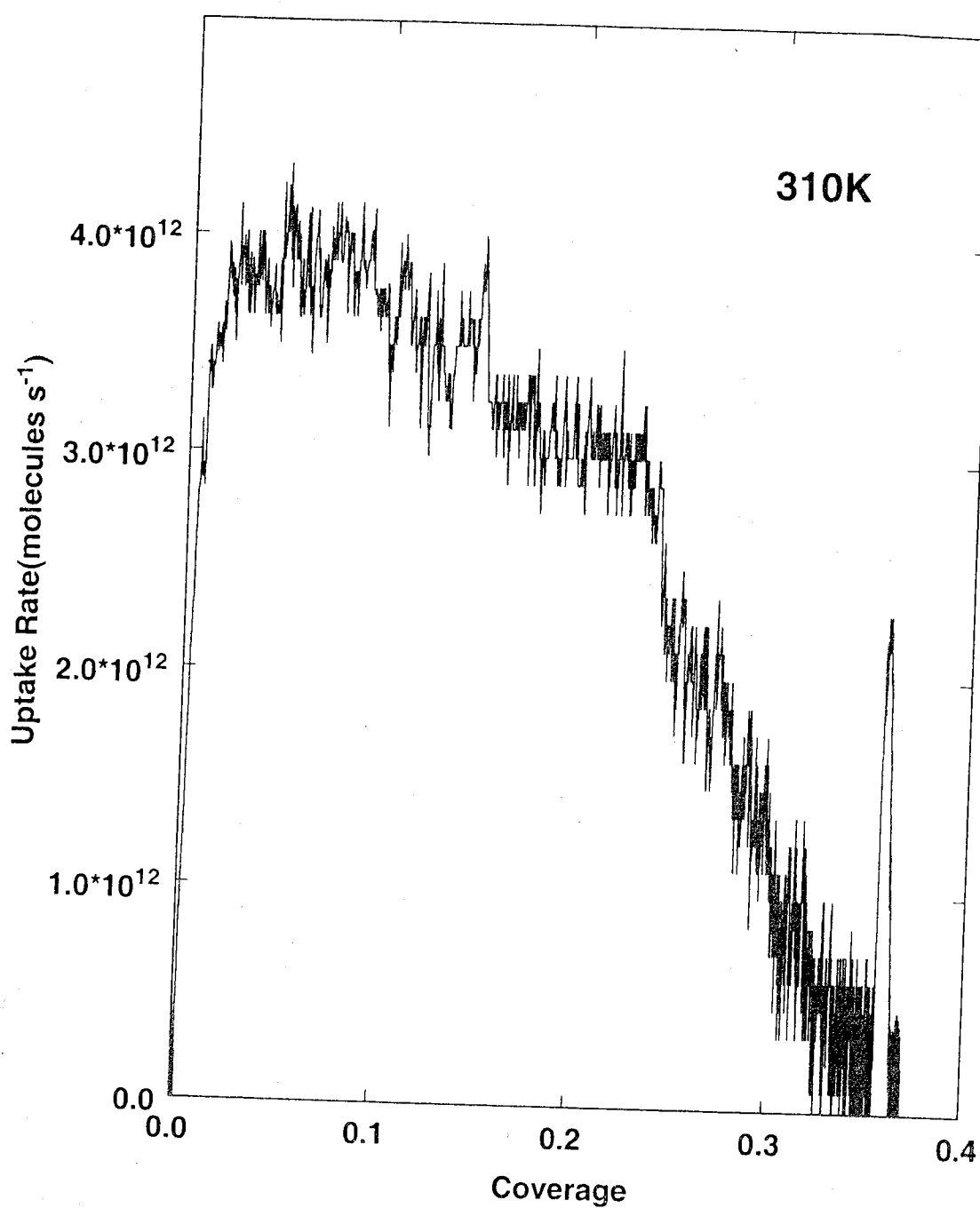


Figure 5.11 Oxygen uptake rate on a  $0.8877\text{cm}^2$  surface area of the Pd(110) crystal at a doser flow of  $1.7 \times 10^{13}\text{ molecule s}^{-1}$  at 310K.

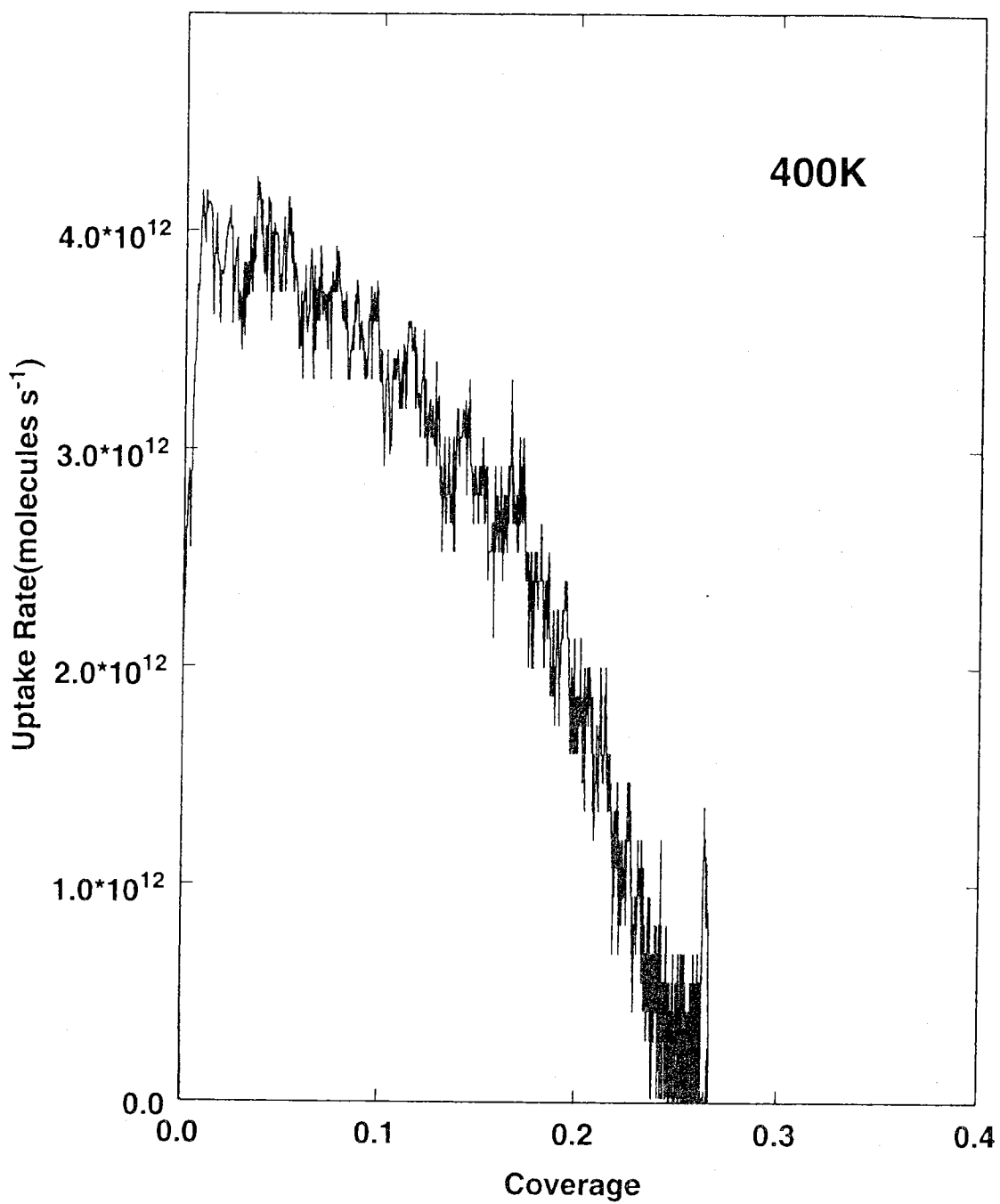


Figure 5.12 Oxygen uptake rate on a  $0.8877\text{cm}^2$  surface area of the Pd(110) crystal at a doser flow of  $1.7 \times 10^{13}\text{ molecule s}^{-1}$  at 400K.

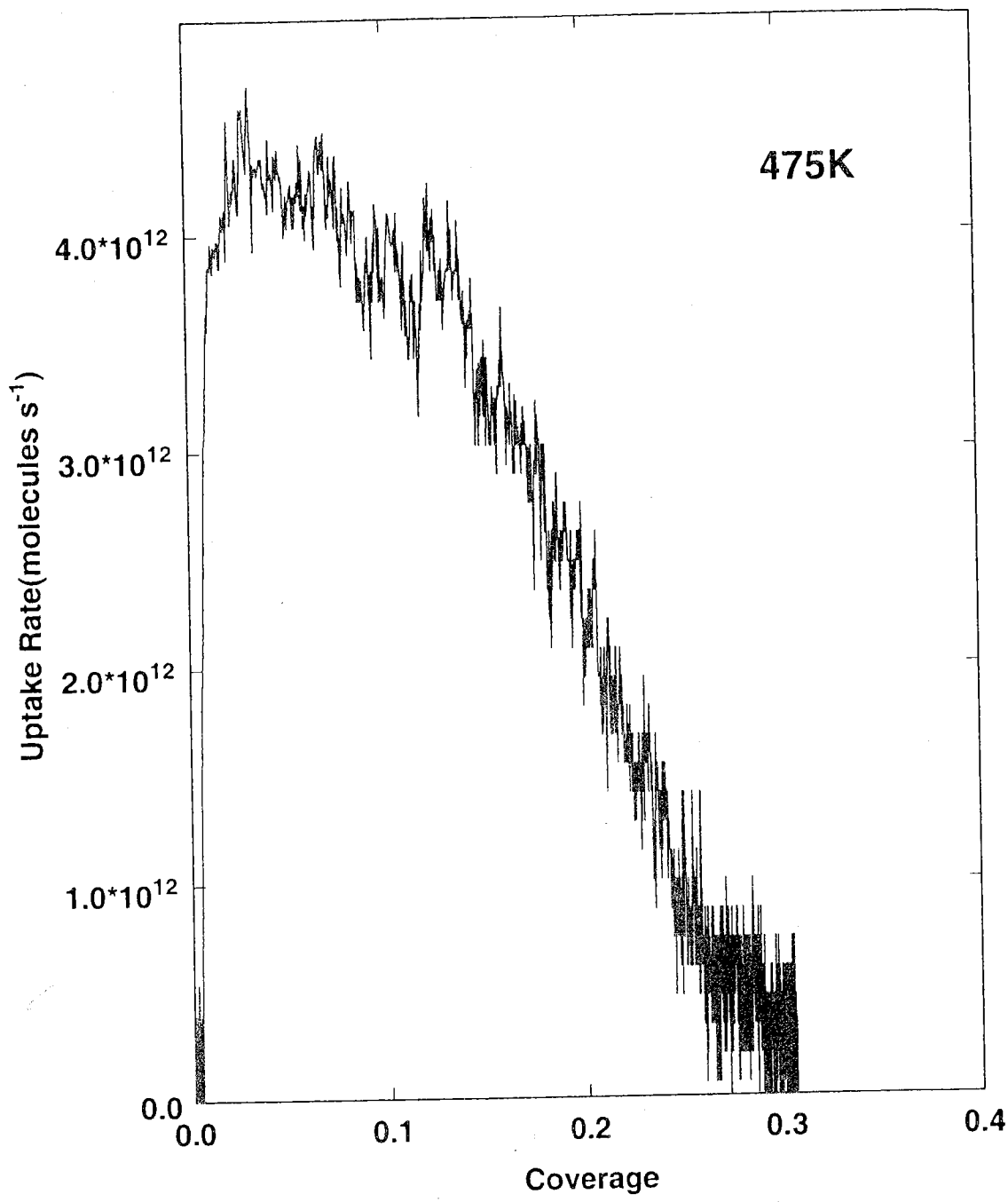


Figure 5.13 Oxygen uptake rate on a  $0.8877\text{cm}^2$  surface area of the Pd(110) crystal at a doser flow of  $1.7 \times 10^{13}$  molecule  $\text{s}^{-1}$  at 475K.

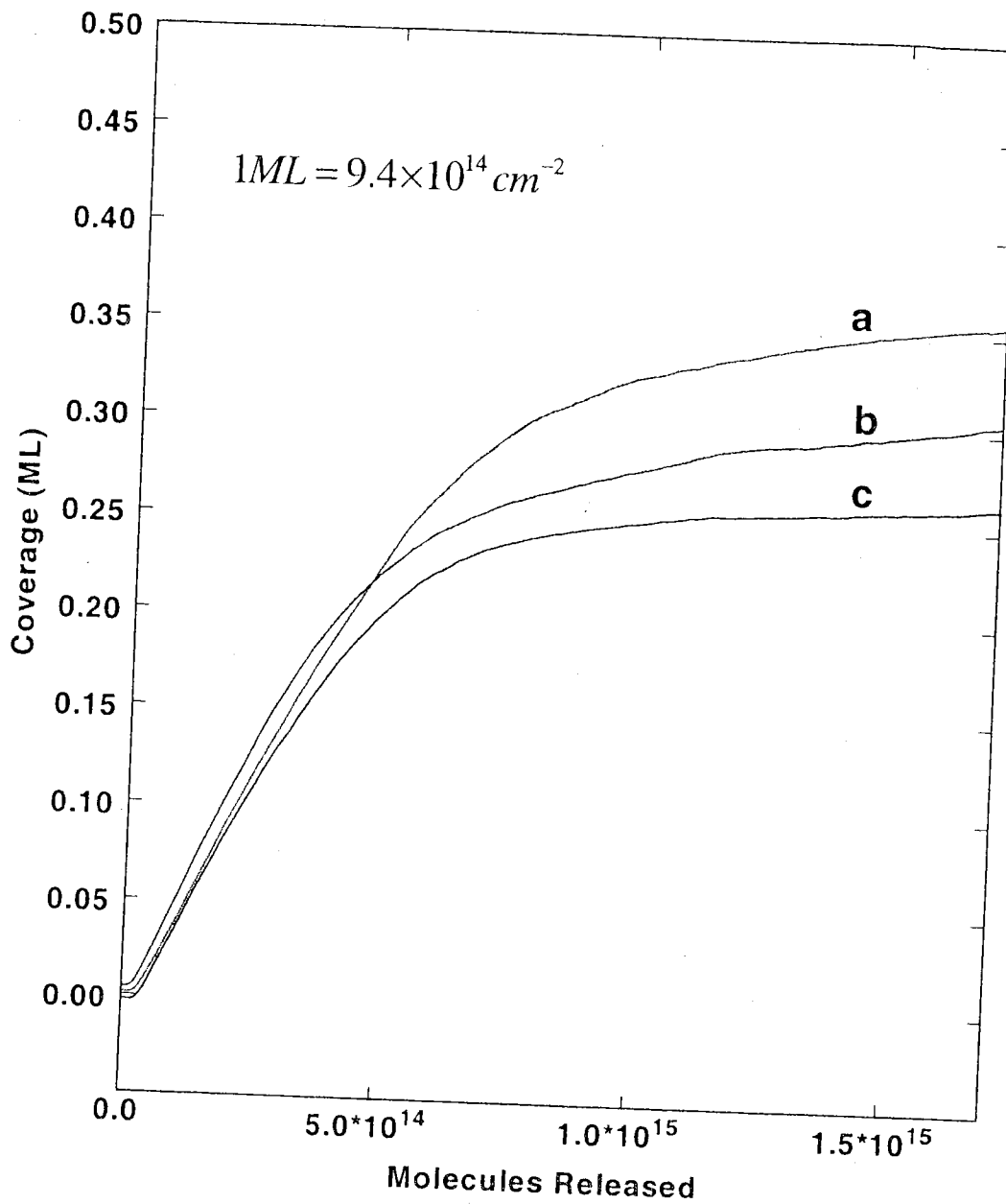


Figure 5.14 The coverage versus dose for each double dose pair at temperature (a) 310K, (b) 475K, and (c) 400K.

Table 5.1 A comparison of CTDS and modified King-Wells coverage measurements of O/Pd(110) for several temperatures.

Figure 5.10 reference	$\theta_{CTDS}$	$\theta_{KW}$	$\frac{\Delta\theta}{\theta_{CTDS}}$	T (K)
a	0.50	0.36	-0.28	310
b	0.44	0.31	-0.30	475
c	0.41	0.27	-0.34	400

The relative difference between the CTDS and the King-Wells coverages remains roughly constant at -30% with respect to the CTDS coverage. In general, we would have expected the King-Wells measurement to be higher than the CTDS, because the uptake is certain to include some adsorption on other surfaces, e.g. the support wires, the edges of the sample, and a small background adsorption on the back of the sample. The lower value of the King-Wells method is not explained by sticking of gas in the doser or on the system walls, the effect which would be higher King-Wells values. The pressures in the chamber was measured for several values of flow showing a perfectly linear relationship, thus removing concerns about pumping speed effects. If there were clean-off reactions after the dose, then the CTDS would be lower. Clean-off reactions during the dose would make the King-Wells value higher.

Since none of the possible sources of error explains a low value of coverage for the King-Wells measurement, we are left to consider the possibility that the sample did not adsorb uniformly. The microscopic structure of the surface could explain either a high value in the case where the adsorbing surface area is greater than the macroscopic area, or conversely for a lower adsorbing area. We speculate that the outside edges of the sample

adsorb less than the center of the sample, where the CTDS was measured, and that the effective area adsorbing oxygen is 30% less than the macroscopic area of the sample. Simmons *et al.*[42] show that the oxygen coverage at 300K on the Pd(100) surface is due to a p(2x2) over-layer with a 0.25 ML coverage. This suggests the possibility that other surface planes like the (111) plane or the (100) plane exposed by scratches or other surface irregularities can adsorb significantly less oxygen. We have also noticed that a freshly sputtered surface adsorbs much lower amounts of oxygen as revealed by TDS. Only after the sample is annealed does the sticking of oxygen improve and the normal oxygen TDS features appear. It is unfortunate that this discrepancy can not be resolved. If a second mass spectrometer were added to the system, then a measurement like that of Goschnick *et al.* could be performed. That version of the King-Wells method samples the same part of the surface during the adsorption measurement as is sampled during the TDS.

#### 5.4.3 Error analysis

The analysis of the errors involved in calibrating the CTDS can be logically broken down by considering the errors due to processes occurring in each part of the apparatus. In this section we consider error processes in the calibrated gas source, the doser, the doser exit distribution, the mass spectrometer shroud, the ionizer, and the mass spectrometer multiplier.

The effusion from the calibrated gas source has a basic systematic uncertainty of 3% in the tangential momentum accommodation coefficient  $\sigma = 1.00$  but is precise to at worst 5 parts in ten thousand. Since the expansion calibration of the gas source volume  $V$ ,

involves ratios of spinning rotor gauge measurements, the values of  $\sigma$  cancel for the volume calibration and the uncertainty is determined from the 0.7% scatter of the measured values. We thus assign a 3.7% uncertainty in accuracy to the gas flow leaving the gas source but report values to a precision of 0.7% due to the scatter in the volume measurement.

The fraction of the doser flux distribution that impinges on the mass spectrometer aperture has two primary sources of error. First, the flow was maintained constant within 0.3% over the 5 hour time during which 900 positions and mass spectrometer readings were manually recorded. The multiplier was checked for drift by returning to the center position after every lateral scan of positions. The maximum variation in the center mass spectrometer readings (from lowest to highest value) was ~1%. Since these variations appeared to be random, we calculated the standard deviation to be 0.4% for 27 values. Because the determination of flux fraction involves the spatial integral of the data, the random errors should cancel, but we conservatively assign the  $1\sigma$  uncertainty of 0.4%; then the fraction at the center of the doser is  $0.07828 \pm 0.003$ . The uncertainties in the position of the doser during measurement were limited to  $\pm 0.001\text{in}$  by using good micrometer technique to avoid backlash.

*The inherent uncertainties in the flux of gas leaving the doser and entering the mass spectrometer aperture is then assigned as a  $\pm 3\%$  systematic uncertainty plus a  $\pm 1.1\%$  random uncertainty to give a total  $\pm 4.1\%$  uncertainty. If the spinning rotor were calibrated at NIST the uncertainty  $\sigma$  could be reduced to  $\pm 1.5\%$ , which can slowly vary within this range over a period of years.*

#### 5.4.4 Transient effects: doser losses or mass spectrometer gain change

Adsorption of gas on the inside of the long doser tube is of primary concern. Since our calibration has assumed that the doser outlet flow was equal to the flow leaving the gas source, any loss of gas due to adsorption or reactive conversion to other components make the flow gain calibration factor for the mass spectrometer higher than the actual value.

*Correction for the loss of gas in the doser would lower the flow gain  $\lambda$  in proportion to the fraction of gas lost.*

The largest uncertainties appear directly in the mass spectrometer flow calibration, during which we release a pulse of gas from the gas source through the doser into the mass spectrometer. In order to understand these uncertainties and the physical behavior of these pulses, we examined a series of pulses of oxygen gas as described in section 5.3.2. A sequence of ten 60s pulses were made with the parameters listed in Table 5.2 where a 600 second pulse was also included between pulses (e) and (f).

Figure 5.16 Ref.	Start Time (min)	$n_0$ ( $10^{20} \text{ m}^{-3}$ )	$n_1$ ( $10^{20} \text{ m}^{-3}$ )	$\int i \cdot dt$ ( $10^{-7} \text{ C}$ )	$I_{\max} - I_{\text{base}}$ (nA)	$\lambda_{\text{int}}$ ( $10^{21} \text{ s}^{-1} \text{ A}^{-1}$ )	$\lambda_{\text{peak}}$ ( $10^{21} \text{ s}^{-1} \text{ A}^{-1}$ )	
a	0	8.3941	8.1779	5.41	9.22	1.507	1.45	
b	4	8.1776	7.9653	5.43	9.15	1.463	1.42	
c	9	7.9651	7.7582	5.34	9.01	1.449	1.41	
d	13	7.758	7.5554	5.26	8.86	1.433	1.39	
e	17	7.5551	7.3585	5.17	8.69	1.420	1.38	
--	--	7.3585	5.6287	A 600s Pulse (not recorded)				
f	33	5.6287	5.4776	4.20	6.97	1.301	1.28	
g	37	5.4777	5.3302	3.99	6.60	1.333	1.31	
h	55	5.1863	5.0465	3.61	6.03	1.395	1.36	
i	59	5.0464	4.9092	3.54	5.86	1.384	1.36	
j	67	4.9092	4.7758	3.43	5.69	1.389	1.37	

Table 5.2 The measured and calculated parameters for ten 60s oxygen pulses.

Figure 5.15 shows the recorded mass spectrometer current divided by the instantaneous flow from the gas source versus time during the dose. Thus, these plots are expressly the reciprocal of the instantaneous flow gain  $1/\lambda(t)$ . A similar way would be to plot this data as the mass spectrometer current corrected for the slow exponential drop in the flow from the effusion source as in Figure 5.3; however, the  $1/\lambda$  plot is more convenient in the analysis to follow. Figure 5.16 shows the top of the pulses expanded and labeled with the reference letters of Table 5.2. From the first pulse (a) through pulse (e),  $1/\lambda$  increased, then a 600 s pulse was made (not recorded due to a software limitation),

followed by pulse (f), which was the largest. Pulse (g) was smaller than (f) and pulses (h,i, and j ) were smaller still, but were substantially the same size.

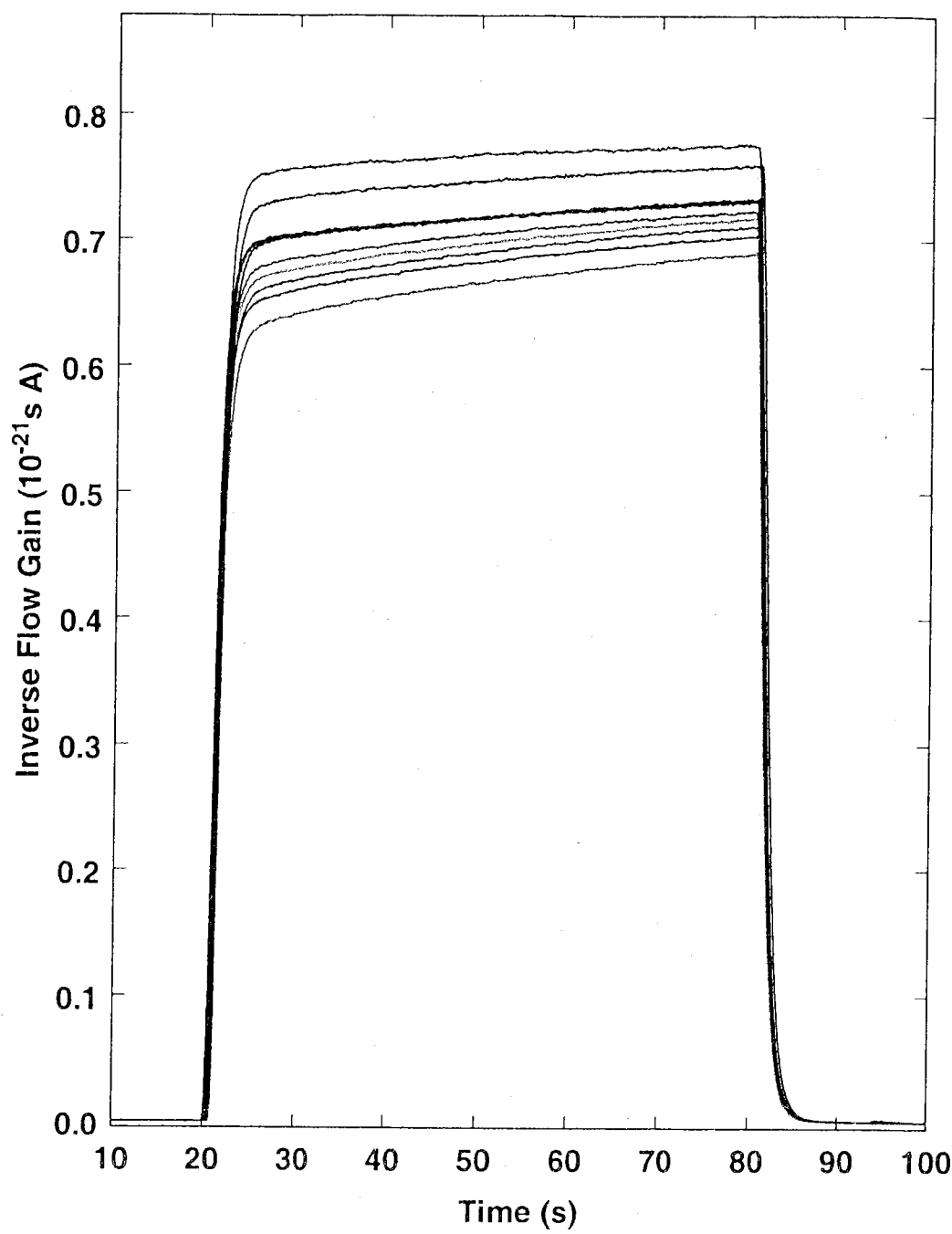


Figure 5.15 60s oxygen pulses for the doser into the mass spectrometer in term of the instantaneous reciprocal of the flow gain.

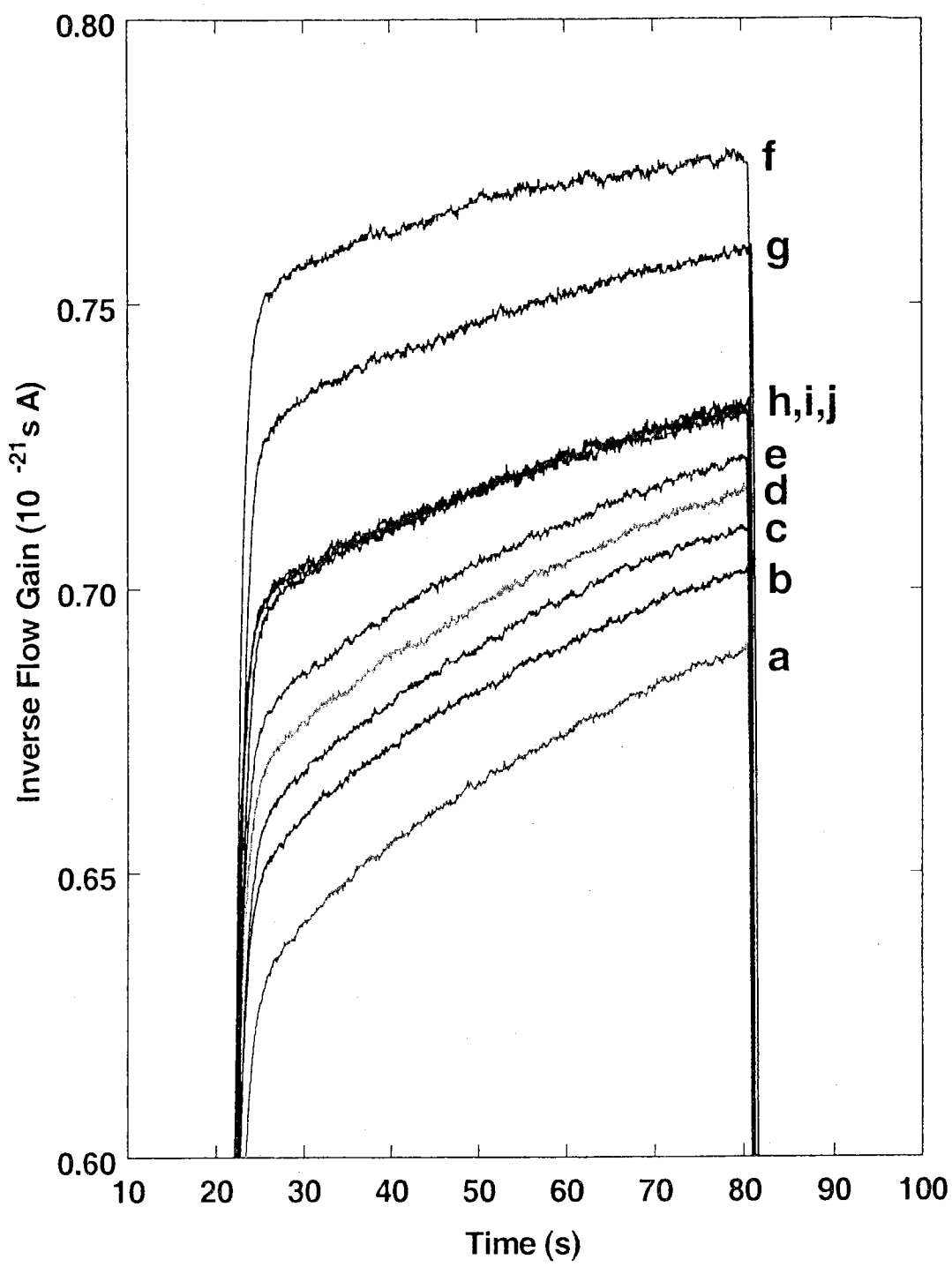


Figure 5.16 The top portion of Figure 5.15

Figure 5.17 shows a linear relationship of the peak and integral calibration factors for a sequence of pulses. Note that these factors settle down to a steady value. We believe this settling to be due to the adsorption of the oxygen on to surfaces in the system, most notably the walls of the doser or the walls of the mass spectrometer shroud. These effects will be analyzed in section 5.4.3 where we consider the possible errors in the calibration.

The linear relationship between the peak and integral calibration values suggest that the shape of the pulses is not changing significantly.

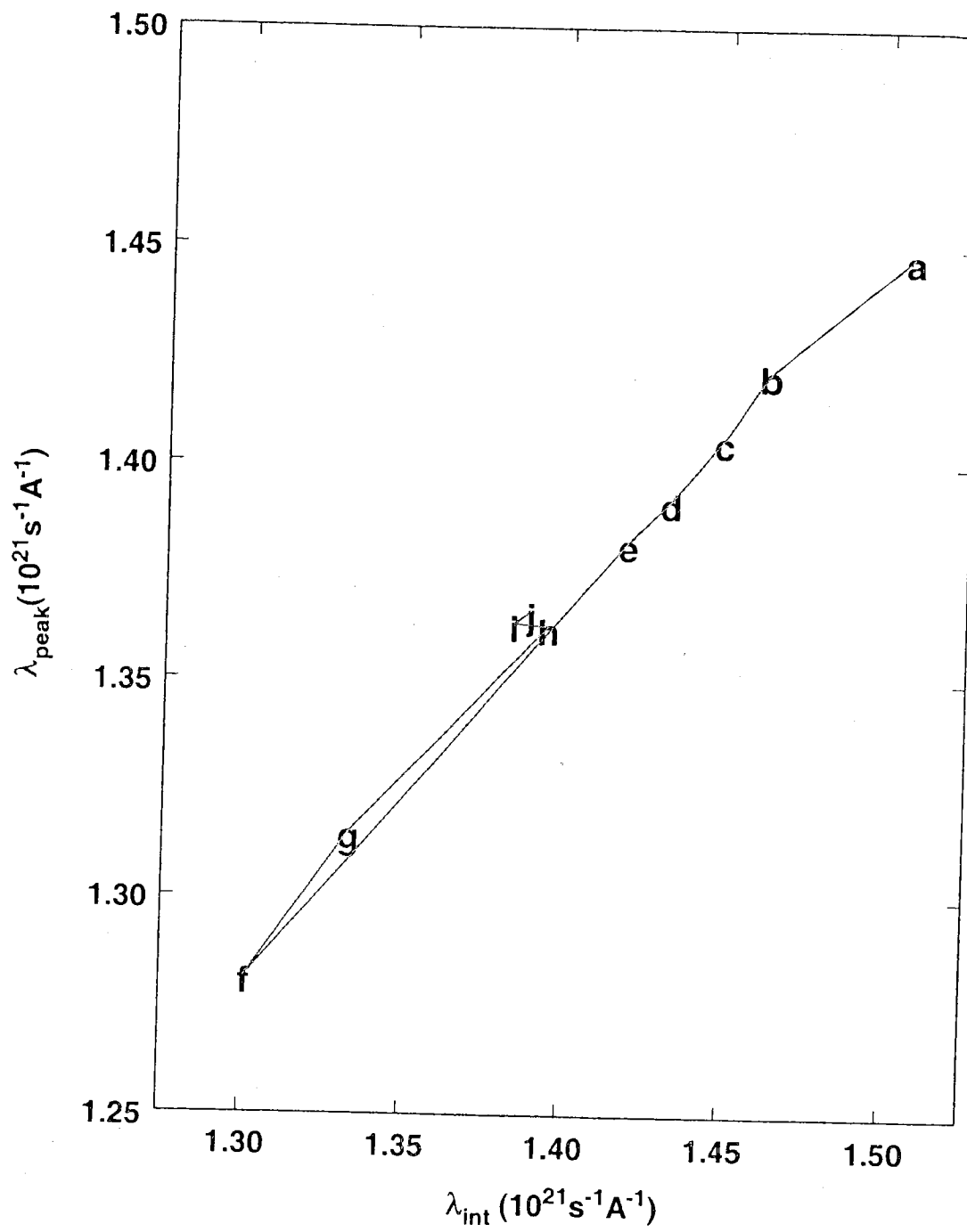


Figure 5.17 The linear relationship between the peak method and integral method calibration factors.

Unlike any of the three transient models of chapter 4, there appears to be an added asymptotic process occurring on a much larger time scale than the 2 to 3 s transient for the doser. Consider the constant sticking model of chapter 4. If adsorbing gas was slowly saturating the surface of the doser, then the fraction exiting would slowly drift up after the initial transient rise until the surface saturated. Since the average number density in the doser is roughly constant after the initial transient, consider the following model of a container of volume,  $V$ , containing gas at a constant number density,  $n$ , and temperature,  $T$ . For simple Langmuir adsorption, the coverage on the surface of the container would obey the differential equation

$$\frac{d\theta}{dt} = \alpha(1 - \theta) - \beta\theta \quad (5.8)$$

where  $\alpha = s_0 n \sqrt{\frac{kT}{2\pi m}}$  and  $\beta = v_0 \exp\left(\frac{-E_d}{kT}\right)$  for initial sticking coefficient  $s_0$ . The solution of this equation is

$$\theta(t) = \frac{\alpha n}{\beta + \alpha n} \left(1 - \exp(-(\beta + \alpha n)t)\right) \quad (5.9)$$

Assuming this process, or some similar process, we fit the exponential equation  $A \exp(B(t - t_0)) + C$  to the tails of plots (a) through (i) from 12 s after the intended valve open time  $t_0 = 20s$  up to the turnoff of the PSO valve. Table 5.3 shows the results of the fits along with the fraction of change  $\frac{\Delta\lambda}{\lambda} = \frac{A}{A+C}$  from the initial value to the asymptote, initial flow gain  $\lambda_0 = \frac{1}{A+C}$ , corresponding to  $t_0 = 20s$ , and the asymptotic flow gain

$\lambda_1 = \frac{1}{C}$ . The parameter B in the exponential is nearly constant with median value

$B_{med} = -0.017 \cdot s^{-1}$ , i.e. an exponential time constant  $\tau_B = 59 \cdot s$ . Thus, within this model,

after  $5 \cdot \tau_B = 295 \cdot s$ , the flow gain  $\lambda(t)$  will reach 99% of its asymptotic value. The initial flow gain,  $\lambda_0$ , varies similarly to  $\lambda_{int}$  and  $\lambda_{peak}$  in Table 5.2.  $\lambda_0$  decreases for each dose

becoming minimum for (f) and finally rises, settling to  $1.44 \times 10^{21} s^{-1} A^{-1}$ , which is 3.6% higher than that for  $\lambda_{int}$ . The asymptotic flow gain  $\lambda_1$  is more nearly constant with a mean

value  $\bar{\lambda}_1 = (1.33 \pm 0.03) \times 10^{21} s^{-1} A^{-1}$ . The fraction change  $\frac{\Delta\lambda}{\lambda}$ , i.e.  $\frac{A}{A+C}$  is about 10% for the settled values of (h, i, and j). The various flow gain values order as  $\lambda_1 < \lambda_{peak} < \lambda_{int} < \lambda_0$ , indicating that the peak and integral methods both give estimates between the initial and asymptotic values.

Figure ( Ref.	A ( $10^{21} s A$ )	B ( $s^{-1}$ )	C ( $10^{-21} s A$ )	$\frac{A}{A+C}$	$\lambda_0$	$\lambda_1$
					$\frac{1}{A+C}$	$\frac{1}{C}$
a	-0.0980	-0.0167	0.725	-0.156	1.59	1.38
b	-0.0859	-0.0175	0.733	-0.133	1.55	1.36
c	-0.0850	-0.0184	0.739	-0.130	1.53	1.35
d	-0.0862	-0.0157	0.751	-0.130	1.50	1.33
e	-0.0748	-0.0185	0.747	-0.111	1.49	1.34
f	-0.0329	-0.0305	0.781	-0.044	1.34	1.28
g	-0.0521	-0.0168	0.778	-0.072	1.38	1.29
h	-0.0641	-0.0158	0.757	-0.093	1.44	1.32
i	-0.0690	-0.0114	0.767	-0.099	1.43	1.30
j	-0.0546	-0.0174	0.750	-0.079	1.44	1.33

Table 5.3 The parameters of an exponential fit through the top part of the pulses.

We removed the effect of this slow exponential process and normalized to the asymptotic value by dividing the plots of Figure 5.15 by the fit exponential function as shown in Figure 5.18. The curves (a) through (g) now appear as a set of similarly shaped transient step responses with a 0.7 s scattering of the open time.

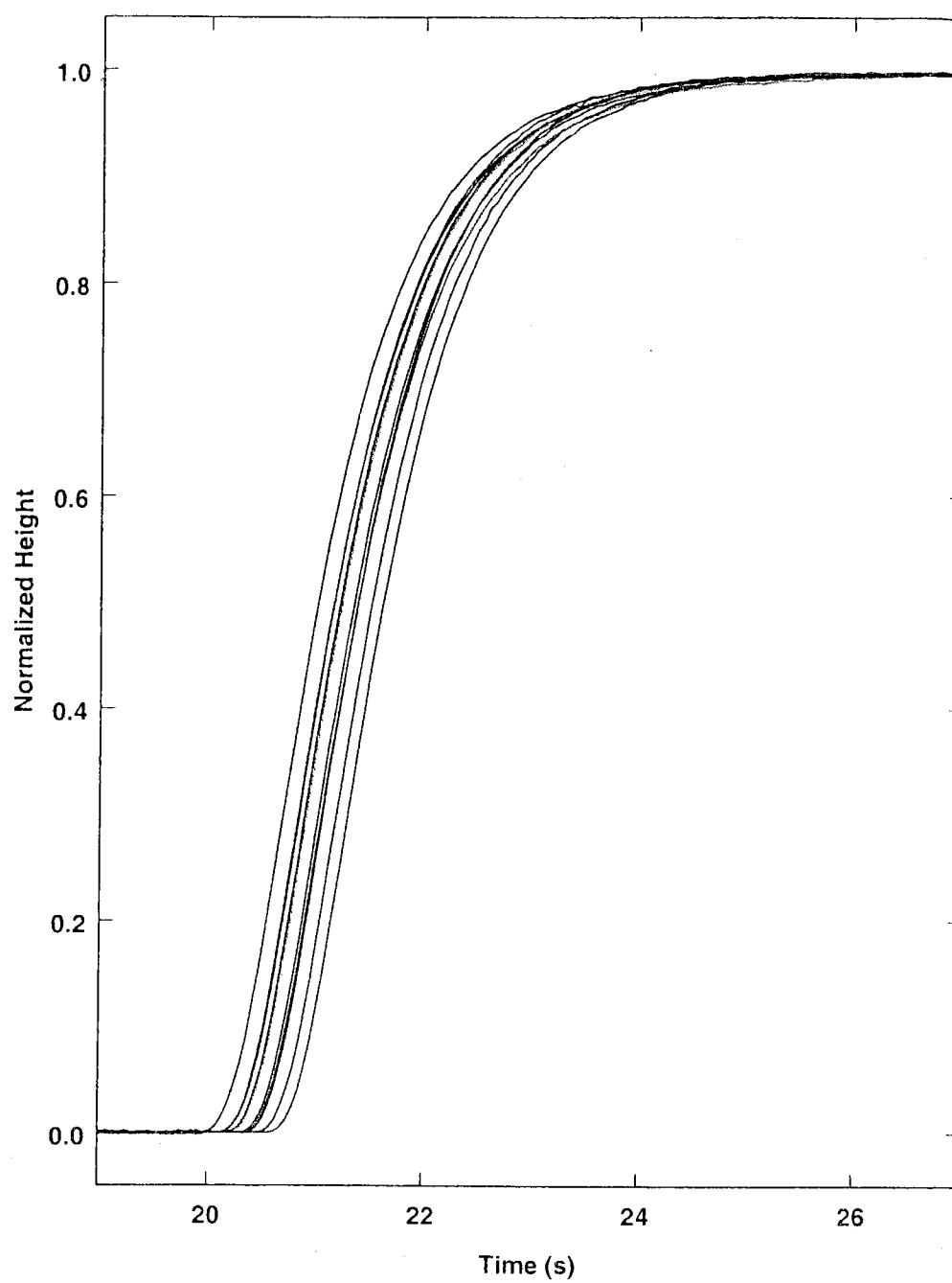


Figure 5.18 The inverse flow gain of Figure 5.15 divided by the slow exponential function fit to the tails.

In order to bring these step responses into coincidence, we use delay/rise values for the non-sticking open tube transient model of section 4.2. We created a cubic spline for each curve and then, using a root-finding algorithm, found the times  $t_d$  and  $t_r$  for the 10% and 90% points respectively. Using the ratio  $\chi = \frac{t_r - t_0}{t_d - t_0} = 7.92189$  from Table 4.1, we solved for the valve open times  $t_0$ . Furthermore, we estimate the value of  $D/L^2$  for the transient using the factor for the delay time in Table 4.1 by  $\frac{D}{L^2} = \frac{0.13016}{t_d - t_0}$ . As shown in Table 5.4, the delay times are constant at 0.28 s and the values of  $D/L^2$  vary  $\pm 2\%$  and are equal to the value  $0.457 s^{-1}$  predicted simply by adjusting the argon value  $0.410 s^{-1}$  for the mass of oxygen. Figure 5.19 shows the curves plotted from their valve open times. The curves are nearly indistinguishable with the maximum variation occurring at the knee of the curves, varying  $\pm 0.7\%$  in height with a time spread of  $\pm 70$  ms.

Figure 5.16 Ref.	$t_d$ (s)	$t_r$ (s)	$t_0$ (s)	$\frac{D}{L^2}$ ( $s^{-1}$ )
a	0.293	2.320	20.441	0.444
b	0.288	2.281	20.229	0.452
c	0.286	2.269	20.418	0.454
d	0.285	2.257	20.311	0.457
e	0.284	2.253	20.294	0.458
f	0.278	2.201	20.472	0.469
g	0.284	2.248	20.694	0.459
h	0.282	2.233	20.591	0.462
I	0.285	2.256	20.087	0.457
j	0.282	2.233	20.245	0.462

Table 5.4 The delay, rise, and start times of the pulse estimated from the non-sticking transient model

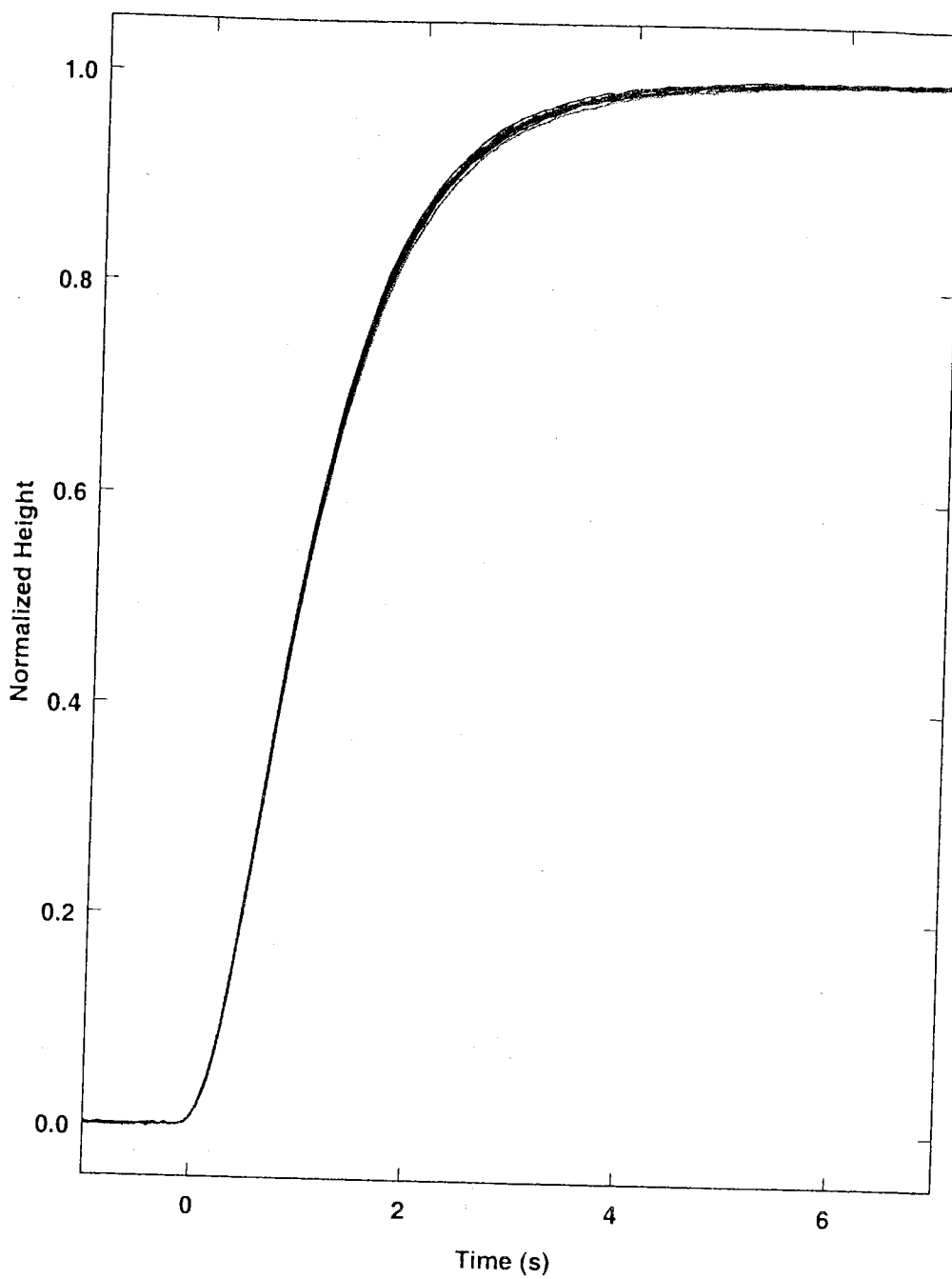


Figure 5.19 The underlying transient of the pulses (a) through (i) shifted to their start times.

Figure 5.20 shows a plot of curve (i) from Figure 5.19 along with the transient calculated from the non-sticking transient flow model using the  $D/L^2$  value of Table 5.4. Since, the  $D/L^2$  is consistent with the argon value corrected for mass, the goodness of the fit at the knee suggests that the underlying transient step response of the doser shows little or no sticking loss in the doser. To show this, assume that at the asymptote the sticking is zero; therefore, at the initial value the fraction lost to sticking is about 10% from Table 5.3. Using the *I-fraction* curve of Figure 4.6 to find  $\lambda L = 0.5$  at 10% loss, then plotting the step response with  $D/L^2$  and  $\lambda L$ , curve b yields a noticeably sharper knee for the step response as indicated in Figure 5.20. The initial sticking coefficient is given by

$$s_0 = \frac{\lambda L}{3} \left( \frac{d}{L} \right)^2. \text{ Estimating, } d/L \approx 0.003 \text{ the initial sticking probability would have to}$$

have been  $s \approx 1.5 \times 10^{-6}$ , which is not supported by Figure 5.20.

Since if the variation of  $\lambda_0$  to  $\lambda_1$  were due to sticking in the doser there would be a change in shape of the underlying transient and since this is not observed, we conclude that the slow exponential process is more likely to be external to the doser. This slow exponential could be consistent with an adsorption loss in the mass spectrometer shroud or it might be possible that the multiplier gain shifts due to adsorption of oxygen. We attempted to resolve the multiplier gain shift question by pulse counting, however, the pulse height distribution for the multiplier merged continuously into the noise level such that we could not discriminate between a change in count rate or a change in multiplier gain.

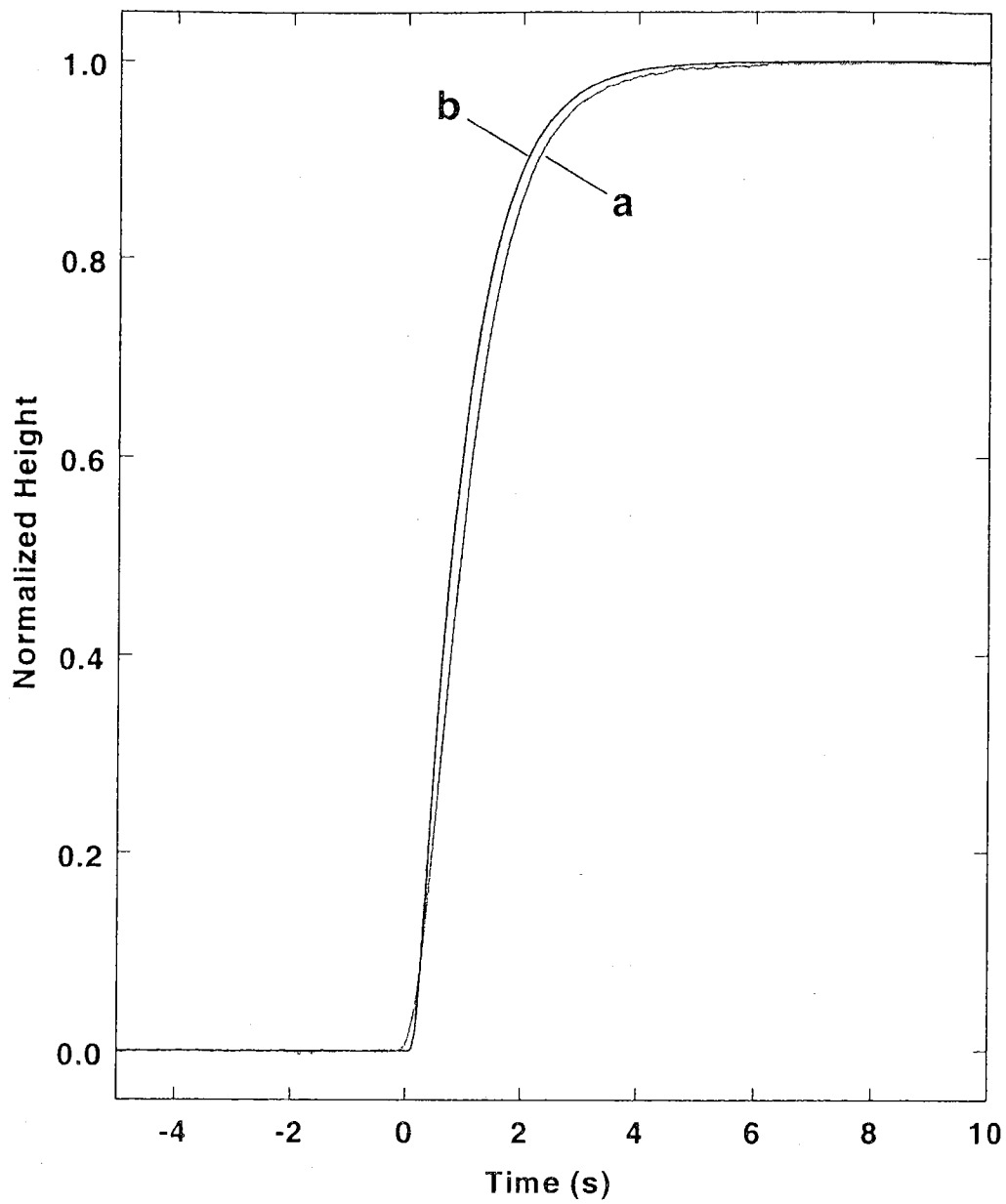


Figure 5.20 A comparison of (a) the transient response of the oxygen pulse (i) of Figure 5.16 divided by the slow exponential and shifted to its start time, (b) the calculated transient response based on the  $D / L^2$  value from Table 5.4 and the sticking equivalent to the 10% change in (i) from start to the asymptote.

## 6 Conclusions and Further Work

We conclude this work by reviewing the methods and results obtained, by suggesting new ideas for a calibrated thermal desorption/ adsorption measurement system derived from the results, and by proposing further extensions and tests of both the flux distribution work and the transient work.

### 6.1 Summary of this work

The general formalism of Winkler and Yates [12] for the calculation of the spatial molecular flux distributions exiting glass capillary arrays was reparameterized reducing the order of integration by one. The parameter  $p$  used by Olander *et al* [32] and subsequently by Winkler and Yates[12] is now interpreted geometrically as a doubly re-scaled radius from a point on the source, such that the capillary flux distribution  $J(\theta)$  is constant on circles of this radius for an adjacent point on the target. This radius is re-scaled in units of distance from source to target and by the ratio of the length to the diameter of the capillaries of the array. The theory was extended to arbitrarily shaped planar targets at any position in front of the array using Fourier Transform convolution techniques.

The molecular flux from the glass capillary array doser to the mass spectrometer was measured versus lateral position for two distances. At a distance of 0.0635cm, the theoretical model fit well with the data consistently determining the diameter of the array. Using the fit parameters the flux distribution at 1cm was correctly predicted.

The transient flow models reveal some basic features, providing a conceptual framework for the understanding of transients in long narrow uniform tubes. These models were shown to fit the measured transient responses for argon gas, but due to the more complicated geometry of the doser only a rough interpretation of the fit parameters was possible. The longer thinner tube directly connected to the mass spectrometer shroud had much longer transient times than the doser tube as is predicted by the theory.

The non-sticking open tube model has solutions for the number density and flow along the length of the tube versus time that are transcendental functions that can be re-scaled for any length  $L$  and diameter  $d$  tube provided  $L/d \gg 1$ . These solutions are easily used to fit the transients flows measured at the exit of the tube using a non-linear least squares algorithm. The fitting parameters can also be estimated by a simple two point delay time/ rise time analysis.

The solution of the open tube model with a constant sticking coefficient has the same eigen-values and eigen-functions but has coefficients that are functions of the sticking probability and the transient part has an overall negative time exponential factor depending on the sticking probability. The steady state solution for the exit flow is a strong function of the sticking probability showing that for the example of a 1m long tube of 1cm diameter, half of the gas is lost to sticking for a sticking probability of  $4 \times 10^{-5}$ . The transient times decrease as a function sticking probability, which is explained in terms of the distribution of molecular transit times and the number of wall hits. A simple average equal step path down the tube is used to estimate the number of wall hits showing that at a 1s transient time

and a 400m/s molecular velocity the average number of hits is estimated at  $6.4 \times 10^4$ , thus accounting for the effects of small sticking probabilities.

The solutions for the non-sticking model for a long tube with a restriction at the exit become more complicated, requiring mixed boundary conditions at the exit and subsequently having eigen-values that are solutions of a transcendental equation that is a function of the ratio of the open tube conductance to the restriction conductance. The eigen-functions are the same relative to their eigen-value but the coefficients are also functions of the eigen-values and conductance ratio. Thus far we have developed a fitting procedure in MathCad that adjusts the parameters, calculates the eigen values, and checks the fit, but due to long computation times (several hours each attempt) we have not been able to fit the data. This can probably be resolved by writing a dedicated algorithm in C.

The transient times are longer as the exit become more restricted, which is explain by the additional time required for the number density in the tube to increase to a level to support the exit flow. It was shown that this model reverts to the unrestricted model as the restriction is diminished.

A test of the calibrated system was made by measuring the c(2x4) O/Pd(110) coverage with CTDS, for which we obtained a coverage of 0.44 ML in agreement with the quoted value of 0.5 ML. Disappointingly, the coverage measured by our modified King-Wells method was inconsistent being 30% lower than the CTDS determined coverage. Consideration was given to the possible causes of this discrepancy including, sticking effects, which would lead to even lower coverages; the method of analysis and

experimental error, which seems to be correct; and finally, the possibility that the Pd(110) crystal being “well used” and rough at the edges did not adsorb uniformly after the extensive clean-off studies and other experiments that were done between the two uptake data sets.

The transient analysis of the calibrating pulses of oxygen show slow exponential ( $\tau = 59\text{s}$ ) approach to an asymptote after the initial transient. This exponential was shown to be consistent with Langmuir adsorption, leading to saturation in a volume held at constant gas density; however, this is only one possible exponential process. Dividing by a fit of this exponential function through the data reveals that the underlying transient behavior is in good agreement with the parameters from the argon data adjusted for the molecular weight of the gas.

Assuming that the initial flow gain found by extrapolating the exponential fit to the valve open time has a small sticking coefficient and that the sticking is zero at the asymptote, there is approximately a 10% change in the measured flow from start to the asymptote. Assuming further that since this process is very slow compared to the underlying transient time through the tube, the constant sticking analysis applies and we estimate the initial sticking probability to be  $1.5 \times 10^{-6}$ , which is not distinguishable in the shape of the underlying transient.

## 6.2 Recommendations for further work

Based on the results of this work and the masters thesis work, we can make recommendations about future versions of a calibrated thermal desorption spectrometer

system with calibrated uptake ability. One major point of philosophy concerning these measurements should be to consider the system and its components as a reaction chamber that we will monitor with mass spectrometers. Considering this point, it is necessary to control and simplify as many of the reaction variables as possible. Using this point of view, we propose an attempt at the ultimate calibrated adsorption and desorption measurement system.

The problem of adsorption in the doser can be reduced by having a custom positive shutoff capillary leak valve constructed, such that the internal volume and surface area is small and such that the glass capillary array is mounted immediately adjacent to the PSO valve. The geometry of such a valve would be designed such that the gas from the valve impinges uniformly across the array. This valve could be constructed to reside entirely inside the vacuum, thus removing the need for a high surface area bellows in the valve construction.

Considering the use of the transient models for the long tube it is probably good to also have a long tube doser with or without an array so that sticking effects can be checked. The long tube doser should have a geometry very close to the model geometry, i.e. straight, with a uniform circular cross-section and the crimped capillary of the PSO as close to the closed end of the doser as possible to minimize the back volume.

Both types of doser should have temperature control for control of the sticking or other surface reactions as well as providing the ability to further study the transient effects

of sticking in the doser. Temperature control could also provide more flexibility for pretreatment of the doser walls, e.g. *in situ* passivation of the walls or other treatments.

The chamber for adsorption and desorption experiments should be as simple in geometry with the least number of flanges, gaskets, etc. It should also be temperature controlled with the ability of fast bake cycles and argon ion discharge or UV cleaning. The ability to throttle the pumping could help provide better optimization of the pumping characteristics for different levels of background dosing. The chamber should be pumped by a combination of a turbomolecular pump for high gas throughput and some kind of getter pump, perhaps a non-evaporable getter (NEG) with an isolation valve. The turbo molecular pump could have an optional diffusion pump at its outlet for better hydrogen pumping.

The differentially pumped mass spectrometer design should incorporate a movable obstruction of the line-of-sight path from the inlet aperture to the ionizer. The pumping speed to the ionizer region should be variable from near the ultimate pumping speed of the pump for line-of-sight measurements to the 10 liter/s speed and small ionizer volume of the present design for the non-line-of sight measurements. These features broaden the range of molecular fluxes that can be measured from non-reactive gases studied in the accommodated mode with the obstruction in place to the highly reactive gases and other sticky fluxes, e.g. evaporating metals.

The first obvious step in the mass spectrometer design is to remove the filament to a position as remote as possible to the measured gas and the mass spectrometer ionizer, thus

eliminating thermal gradients and eliminating the various high temperature reactions that can occur. This design would constitute a type of "cross beam ionizer" design, but would require an innovation to reduce the dependence of ionization probability on molecular velocity. Since we are measuring a beam of gas from the aperture, it may also be possible to design the ionizer ion extraction optics to select ions created only in the region of the intersection of the molecular beam and the ionizer electron beam. Preliminary estimates show that for a gas that typically has a background in the chamber, the ultimate signal to background could be improved by a factor of four for a typical desorption flux through a  $0.1\text{cm}^2$  aperture by using such an ionizer design.

Finally, proper pulse counting mass spectrometry should be used with the multiplier operating such that the pulse height distribution is well separated from the noise, so that the count rate is immune to gain variations due to gas reactions at the multiplier. Since the multiplier will operate at its plateau, we will have to reconsider the maximum gas flow through the aperture. Note that the possibility of reducing the aperture size helps several other aspects of the measurements. First a smaller portion of the sample can be measured. Second, the flux distribution measurements, which are convolved with the aperture, would more nearly represent the actual distribution. Third, if we use the method of Goschnick *et al* [7] to measure the uptake the change of the background impingement by the presence of the aperture may be improved.

Finally, we discuss some further theoretical and experimental work to be continued. The further development of better transient models and their experimental verification for simple geometries with more realistic inclusion of variable or saturable sticking would

provide a better basis from which to correct for sticking losses in the calibrated flow. Furthermore, it might be possible to utilize the large number of hits and the subsequent sensitivity of the transient flow to very small sticking probabilities to measure gas adsorption on very low sticking probability surfaces. The inclusion of saturable sticking to the transient diffusion model would require some sort of self-consistent numerical analysis to solve the integro-partial differential equation. It might be possible to cast the problem as Freholm type problem and use the calculation tools available for this well-known problem.

Further work could be done to develop simple design tools for molecular transient flow. For example, we started to find a method of adding simple diameter tubes together such that we could estimate the transient times using a simple addition of transient time approach. This approach should be verified by solving the diffusion equation with matching conditions between the sections. Since our solutions are for the step flow response of the transient flow system, we can also apply Laplace convolution techniques to find the response to other inlet flows. We might be able to provide a set of, albeit more complicated, design tools similar to the standard steady state vacuum calculations.

To conclude this work it is noteworthy to say that this work embodies a beginning for the development of a truly analytical technique. The goal is to make quantitative measurements of adsorption and desorption, expecting closure in the measurements; i.e. the difference of the adsorbed amount and the desorbed amount is interpretable as the amount left on the surface. This ability alone could help us move away from model surfaces where we require other knowledge to absolutely determine the surface concentrations and reaction rates of atomic and molecular species at surfaces.

## References

1. Charles B. Duke, *Surface Science. The First Thirty Years* (North Holland, Amsterdam, 1994).
2. W.H. Weinberg, M.A. van Hove, and C.-M. Chan, *Low Energy Electron Diffraction: Experiment, Theory, and Surface Structural Determination* (Springer-Verlag, Heidelberg, 1986).
3. M. P. Seah, "XPS Reference Procedure for the Accurate Intensity Calibration of Electron Spectrometers -- Results of a BCR Intercomparison Co-sponsored by the VAMAS SCA TWA ,," *Surf. Interface Anal.* **20**, 243-266 (1993).
4. J.B. Hudson, *Surface Science: an Introduction* (Butterworth-Heinemann, Boston, 1992).
5. K. Christmann, *Introduction to Surface Physical Chemistry* (Springer, New York, 1991).
6. M. Henzler and W. Göpel, *Oberflächenphysik des Festkörpers* (B.G. Teubner, Stuttgart, 1991).
7. J. Goschnick, M. Wolf, M. Grunze, W.N. Unertl, J.H. Block, and J. Loboda-Cacovic, "Adsorption of O<sub>2</sub> on Pd(110)," *Surf. Sci.* **178**, 831-841 (1986).

8. V.S. Smentkowski and J.T. Yates, "A multipurpose quadrupole mass spectrometer detector for surface kinetic and absolute coverage measurements," *J. Vac. Sci. Technol. A* **7** (6) (1989).
9. J.-W. He, U. Memmert, K. Griffiths, W.N. Lennard, and P.R. Norton, "Absolute coverages for the various surface phases of CO and O adsorbed on Pd(110)," *Surf. Sci.* **202**, L555-L558 (1988).
10. Robert H. Jackson, "The Design of a Calibrated Thermal Desorption Spectrometer," Masters Thesis, University of Maine, 1996.
11. G. Binnig and H. Rohrer, "Scanning Tunneling Microscopy," *Helv. Phys. Acta* **55**, 726-735 (1982).
12. A. Winkler and J.T. Yates Jr., "Capillary array dosing and angular desorption measurements: A general formalism," *J. Vac. Sci Technol. A* **6** (5), 2929-2932 (1988).
13. D.A. King and M.G. Wells, "Molecular Beam Investigation of Adsorption on Bulk Metal Targets: Nitrogen on Tungsten," *Surf. Sci.* **29**, 454-482 (1972).
14. C.M. Chan and W.H. Wienberg, "An Analysis of Thermal Desorption Spectra. II.," *Appl. Surf. Sci.* **1**, 377 (1978).
15. P.A. Redhead, "Thermal Desorption of Gases," *Vacuum* **12**, 203 (1962).
16. D. A. King, "Thermal Desorption from metal surfaces: A review," *Surf. Sci.* **47**, 384-402 (1975).

17. Micheal A. DeAngelis and A. Brad Anton, "Temperature Programming for Isothermal Desorption Rate Measurements," *J. Vac. Sci. Technol. A* **10** (6), 3507-3516 (1992).
18. Deborah Holmes Parker, Mark E. Jones, and Bruce Koel, "Determination of the Reaction Order and Activation Energy for Desorption Kinetics Using TPD: Application to D<sub>2</sub> Desorption from Ag(111)," *Surf. Sci.* **233**, 65-74 (1990).
19. J.F. O'Hanlon, *A users Guide to Vacuum Technology*, 2nd ed. (John Wiley & Sons, New York, 1989).
20. G. Reich, "Spinning rotor viscosity gauge: A transfer standard for the laboratory or an accurate gauge for vacuum process control," *J. Vac. Technol.* **20** (4), 1148-1152 (1982).
21. S. Dittmann, B.E. Lindenau, and C.R. Tilford, "The molecular drag gauge as a calibration standard," *J. Vac. Sci. Technol. A* **7** (6), 3356-3360 (1989).
22. T. J. Cassidy, M. D. Allen, Y. Li, and M. Bowker, "From surface science to catalysis - surface explosions observed on Rh crystals and supported catalysts," *Cat. Lett.* **21** (3-4), 321-331 (1993).
23. S. Haq, R. C. Bainbridge, B. G. Frederick, and N. V. Richardson, "Anhydride ring chemistry at a metal surface," *J. Phys. Chem. B* **102**, 8807-8815 (1998).
24. J. McCarty, J. L. Falconer, and R. J. Madix, "Surface explosion: HCOOH on Ni<110>," *Surf. Sci.* **42**, 329-330 (1974).

25. V. A. Bondzie and D.J. Dwyer, *Surf. Sci.* **347**, 319-328 (1996).
26. Jian-Wei He, Ulrich Memmert, Kieth Griffiths, and Peter R. Norton, "Interaction of oxygen with a Pd(110) surface.I. Structure and coverages.," *J. Chem. Phys.* **90** (9), 5082-5087 (1989).
27. Jian-Wei He, Ulrich Memmert, and Peter R. Norton, "Interaction of oxygen with a Pd(110) surface. II. Kinetics and energetics," *J. Chem. Phys.* **90** (9), 5088-5093 (1989).
28. J.-W. He and P.R. Norton, "Thermal desorption of oxygen from a Pd(110) surface," *Surf. Sci.* **204**, 26-34 (1988).
29. C.T. Campbell and S.M. Valone, "Design considerations for simple gas dosers in surface science applications," *J. Vac. Sci. Technol. A* **3** (2), 408-411 (1985).
30. H.P. Steinruck and K.D. Rendulic, "A test of capillary array beam sources for very large Knudsen numbers," *Vacuum* **36** (4), 213-215 (1986).
31. H.C.W. Beijerinck and N.F. Vester, "Velocity distribution and angular distribution of molecular beams from multichannel arrays," *J. Appl. Phys.* **46** (5), 2083-2091 (1975).
32. Donald R. Olander and Valerie Kruger, "Molecular Beam Sources Fabricated from Multichannel Arrays. III. The Exit Density Problem," *J. Appl. Phys.* **41** (7), 2769-2776 (1970).
33. Von P. Clausing, "Über die Strahlförzung bei der Molekularströmung," *Zeitschrift für Physik* **66**, 471-477 (1930).

34. Athanasios Papoulis, *Circuit and Systems: A Modern Approach* (Holt, Rinehart, and Winston, Inc., New York, 1980).
35. A. Bermann, *Total Pressure Measurements in Vacuum Technology* (Academic Press, Inc., Orlando, 1985).
36. Kazutoshi Yagi, Daiichiro Sekiba, and Hirohito Fukutani, "Adsorption and desorption kinetics of oxygen on the Pd(110) surface," *Surf. Sci.* **442**, 307-317 (1999).
37. Horst Niehus and Carlos Achete, "Oxygen-induced mesoscopic island formation at Pd(110)," *Surf. Sci.* **369**, 9-22 (1996).
38. R.A. Bennett, S. Poulston, I.Z. Jones, and M. Bowker, "High-temperature scanning tunneling microscopy studies of oxygen-induced reconstructions of Pd(110)," *Surf. Sci.* **401**, 72-81 (1998).
39. Hiroyuki Tanaka, Jin Yoshinobu, and Maki Kawai, "Oxygen-induced reconstruction of the Pd(110) surface: an STM study," *Surf. Sci.* **327**, L505-L509 (1994).
40. Kazutoshi Yagi and Hirohito Fukutani, "Oxygen adsorption site of Pd(110)c(2x4)-O: analysis of ARUPS compared with STM," *Surf. Sci.* **412/413**, 489-494 (1998).
41. V.A. Bondzie, P. Kleban, and D.J. Dwyer, "XPS identification of the chemical state of subsurface oxygen in the O/Pd(110) system," *Surf. Sci.* **347**, 319-328 (1996).

42. Gary W. Simmons, Yarw-Nan Wang, Juan Marcos, and Kamil Kleir, "Oxygen Adsorption on Pd(110) Surface: Phase Transformations and Surface Reconstructions," *J. Phys. Chem.* **95**, 4522-4528 (1991).

## **Biography of the Author**

Robert H. Jackson was born in Englewood, New Jersey on 12 June 1958. His family and he moved to Eddington, Maine in 1961. He graduated from Brewer High School in 1977, after which he attended the "electronics technology program" at Eastern Maine Vocational Technical Institute. Deciding to seek a higher education, Robert left the technical institute in 1978. He took a job as a laboratory assistant in the clinical laboratory at Eastern Maine Medical Center where he worked to pay for school. In the spring of 1979 he started course work at the University of Maine pursuing a degree in Engineering Physics. In the summer of 1985 Robert left the University to take an electrical engineering job at Nautel Maine Inc., a local subsidiary of the electronics manufacturer Nautical Electronics Laboratories Limited of Nova Scotia. In the winter of 1991 Robert received a research stipend from the University of Heidelberg which allowed him to return to the University of Maine. Robert completed a Bachelor of Science degree in Engineering Physics in August 1991 then enrolled in graduate school with a research assistantship at the Laboratory for Surface Science and Technology. Robert received a Master of Science degree in Physics from the University of Maine in 1996. Robert's Masters Thesis was entitled "The Design of a Calibrated Thermal Desorption Spectrometer." Robert has continued this work as graduate research assistant at the Laboratory for Surface Science and Technology, University of Maine. Robert is a candidate for the Doctor of Philosophy degree in Physics from the University of Maine in August 2000.